Theoretical studies on the viscosity and the dynamics of dilute dispersions of chains in shear flow using direct numerical simulation

Hideki Kobayashi

2011

Contents

Chapter 1

General Introduction

1.1 Introductory remark

A dispersion is a system in which particles are dispersed in a continuous phase of a different composition. The particles dispersed in a continuous phase are called dispersoids, and the continuous phase is called the disperse medium. The dispersoids and the disperse medium can be gases, liquids, or solids.

Understanding the macroscopic properties of dispersions is an important problem in many fields of science and engineering, such as statistical physics, soft matter physics, chemical engineering, and mechanical engineering. Thus, this system is currently being actively investigated. In our daily lives, there are many products that rely on dispersions, for example, paints, cosmetics, inks, pastes, milk, and jelly. It is important to understand the macroscopic properties of dispersions to design products and for industrial manufacturing and processing. Concretely speaking, it is easy to design the chemical plant by predicting the physical properties of polymer solutions, and a cake with a wonderful texture can be made by understanding the viscoelasticity of foodstuffs. The macroscopic properties of dispersions greatly depend on the dynamics of the dispersoids in the disperse medium. Understanding these dynamics is valuable in the field of engineering. Although considerable efforts have been made to experimentally and theoretically investigate the dynamic of dispersed systems in the past decade, the relationships between the dynamics of dispersoids and the macroscopic properties in the non-equilibrium state are still subjects of ongoing research.

In this dissertation, the viscosity and the dynamics of chains (such as rigid rods and flexible polymer) are investigated in a Newtonian fluid under shear flow. This system is simple compared to other systems encountered in various industrial applications, such as charged particles in electrolyte solutions and polyelectrolytes. Nevertheless, the dynamics of particles in Newtonian fluids in the non-equilibrium state has not been fully understood because the dynamics of particles in Newtonian fluids is essentially a many-body problem caused by hydrodynamic interactions, which are a long range force. In particular, the dynamics of chains is more complex in comparison with those of spherical particles, and many problems still remain. Therefore, investigating this topic is valuable

in both scientific and engineering fields.

The subject of this chapter is to provide a background on dispersions and the objectives of this dissertation.

1.2 Chain dispersion

The chain dispersion investigated in this dissertation belongs to the category of colloidal dispersions based on the particle size. In a colloidal dispersion, the dynamics of particles are strongly affected by the thermal fluctuations of their host fluids. The dynamics of the chain is complex, and understanding the statics and dynamics of the chain is a central issue in colloidal science and polymer science.

Although this system is simple, the macroscopic properties are indeed interesting. For example, in a dilute system, which is the simplest one, the viscosity shows shear-thinning behavior,[1,2] which is non-Newtonian behavior. In a condensed system, the viscosity shows shear banding.[3] Although the components of the system are simple, the viscosity shows various behaviors by changing the shear rate or the volume fraction. The reason for the complex behavior is the competition of the hydrodynamic interaction, the shear rate, the thermal fluctuation, and the excluded volume effect. The variations in behavior are not only useful in engineering fields but are also interesting in science fields. Understanding the non-equilibrium state can be advanced by the knowledge obtained through this research.

However, the dynamics of a colloidal dispersion in a shear flow is essentially a many-body problem caused by hydrodynamic interactions. Even if there is only one particle in the system, the dynamics of the particle is affected by itself. Therefore analysing the dynamics of the dispersion leads to hard problems. It is too difficult to understand the mechanism determining the macroscopic properties from the dynamics of particles with a theoretical approach alone. It is also very difficult to directly observe the dynamics of colloidal particles using an experimental approach alone. To understand the relationship between the macroscopic properties and the dynamics of colloidal particles, a numerical approach is important.

1.3 Computer simulation

To understand the dynamics of chain dispersions, computer simulations are very powerful tools. Simulations can carry out virtual experiments on the phenomenological model based on physical

considerations using a computer and verify the validity of the physical considerations. Thus, numerical simulations are important tool to discover and to predict undiscovered phenomena. It was recently developed as the third approach to follow the experiment and the theory.

However, the dispersion system is typically a multi-scale problem, and calculating this system with computer simulations causes serious problems. The molecules comprising the dispersion medium are smaller and move faster than dispersoids. The performance of a fully microscopic molecular simulation on an atomistic time scale requires a huge computational time to obtain physically meaningful results about the dispersion. In simulations disregarding the freedom of the solvent, the synchronisation of the disperse medium with the dispersoid cannot be described. To overcome this problem, a numerical modelling method based on a coarse-graining approach over mesoscopic scales can be used. Mesoscales, between the atomistic and macroscopic scales, are very important in dispersions. In this approach, the dispersion medium is often treated as a continuum velocity field, and coarse-graining models can describe the synchronisation of the disperse medium with the dispersoid.[4–8]

Recently, Nakayama and Yamamoto[5,6] developed a numerical method, that is known as the smoothed profile method (SPM) for direct numerical simulation (DNS) which is based on a mesoscale model, and Iwashita introduced thermal fluctuations to the original SPM.[7,8] This method is used to calculate the translational velocity autocorrelation function (VACF) and the rotational velocity autocorrelation function (RVACF). The VACF and the RVACF show an asymptotic approach to the hydrodynamic long-time tail, which agrees well with analytical solutions.[7,8] In this dissertation, the dynamics and the viscosity of a chain dispersion are calculated by using the SPM introduced thermal fluctuations. I explain this method in following section.

1.3.A Smoothed Profile Method

In the SPM, the boundary between the solid particles and the solvent is replaced with a continuous interface by assuming a smoothed profile. This simple modification enables us to calculate hydrodynamic interactions both efficiently and accurately without neglecting many-body interactions. The equation governing the dynamics of particle dispersion is a modified Navier-Stokes equation:

$$\rho \left\{ \frac{\partial \mathbf{u}}{\partial t} + (\mathbf{u} \cdot \nabla)\mathbf{u} \right\} = \nabla \cdot \boldsymbol{\sigma} + \rho\phi\mathbf{f}_{\mathrm{p}} \tag{1.1}$$

with the condition of incompressibility $\nabla \cdot \mathbf{u} = 0$, where ρ is the solvent density,

$$\boldsymbol{\sigma} = -p\mathbf{I} + \eta_{\mathrm{f}} \left\{ \nabla \mathbf{u} + (\nabla \mathbf{u})^T \right\} \tag{1.2}$$

is the Newtonian stress tensor with a solvent viscosity of η_{f}, and $\mathbf{u}(\mathbf{r}, t)$ and $p(\mathbf{r}, t)$ are the velocity and pressure of the dispersion, respectively. A smoothed profile function $0 \leq \phi(\mathbf{r}, t) \leq 1$ distinguishes between the fluid and particle domains as well as yields $\phi = 1$ in the particle domain and $\phi = 0$ in the fluid domain. These domains are separated by thin interstitial regions with thicknesses characterized by ξ. The dispersion density ρ is represented as

$$\rho = (1 - \phi)\rho_{\mathrm{f}} + \phi\rho_{\mathrm{p}} \tag{1.3}$$

where ρ_{f} and ρ_{p} are the solvent and particle densities, respectively. Only neutral buoyancy dispersions with $\rho = \rho_{\mathrm{f}} = \rho_{\mathrm{p}}$ are simulated in the present study. The body force $\phi\mathbf{f}_{\mathrm{p}}$ is introduced so that the total velocity field $\mathbf{u}$ of the dispersion satisfies $\mathbf{u}(\mathbf{r}) = (1 - \phi)\mathbf{u}_f(\mathbf{r}) + \phi\mathbf{u}_p(\mathbf{r})$, where $\mathbf{u}_f$ is the fluid velocity and $\mathbf{u}_p$ represents the rigid motions of the particles. The incompressible condition $\nabla \cdot \mathbf{u} = 0$ thus ensures $\nabla\phi \cdot (\mathbf{u}_p - \mathbf{u}_f) = 0$ because both $\mathbf{u}_f$ and $\mathbf{u}_p$ satisfy incompressible conditions. The gradient of ϕ is proportional to the surface-normal vector and has a support on the interfacial domains. Therefore, the body force $\phi\mathbf{f}_{\mathrm{p}}$ introduced to satisfy the rigidity of the particles ensure the appropriate impermeability boundary conditions at the fluid-particle interface, while the non-slip boundary conditions are imposed automatically by the viscous stress term in the Navier-Stokes equation. More detailed explanations and the mathematical expressions for ϕ and $\phi\mathbf{f}_{\mathrm{p}}$ were also detailed in previous papers.[5,6]

The motion of the i-th particle in a dispersion is governed by Newton's and Euler's equations of motion:

$$M_i \frac{d}{dt}\mathbf{V}_i = \mathbf{F}_i^{\mathrm{H}} + \mathbf{F}_i^{\mathrm{P}} + \mathbf{G}_i^V, \quad \frac{d}{dt}\mathbf{R}_i = \mathbf{V}_i \tag{1.4}$$

$$\mathbf{I}_i \cdot \frac{d}{dt}\boldsymbol{\Omega}_i = \mathbf{N}_i^{\mathrm{H}} + \mathbf{G}_i^{\Omega} \tag{1.5}$$

where $\mathbf{R}_i$, $\mathbf{V}_i$, and $\boldsymbol{\Omega}_i$ are the position, translational velocity, and rotational velocity of the colloidal particles, respectively. M_i and $\mathbf{I}_i$ are the mass and the moment of inertia, and $\mathbf{F}_i^{\mathrm{H}}$ and $\mathbf{N}_i^{\mathrm{H}}$ are the hydrodynamic force and torque exerted by the solvent on the colloidal particles, respectively.[5,6] $\mathbf{G}_i^{\mathrm{v}}$ and $\mathbf{G}_i^{\Omega}$ are the random force and torque, respectively, due to thermal fluctuations. The

temperature of the system is defined such that the long-term diffusive motion of the colloidal particles reproduces the Stokes-Einstein rule.[7,8] $\mathbf{F}_i^{\mathrm{P}}$ represents the potential force due to direct inter-particle interactions such as through the Coulombic and Lennard-Jones potentials.

We calculate the dynamics of solid particle dispersions by following these steps:

i) The fluid velocity field in the oblique coordinate system at a new time $t = nh$ is calculated by integrating Eq. (1.1) over time with $\phi\mathbf{f}_{\mathrm{p}} = 0$ as

$$\mathbf{u}^* = \mathbf{u}^{n-1} + \int_{t_{n-1}}^{t_{n-1}+h} \left[\nabla \cdot \left(\frac{1}{\rho}\sigma - \mathbf{uu}\right)\right] ds \tag{1.6}$$

while satisfying the incompressibility condition $\nabla \cdot \mathbf{u}^* = 0$. Here, the superscript n denotes the time step, and h is the time increment.

ii) The position of each colloidal particle is calculated by

$$\mathbf{R}_i^n = \mathbf{R}_i^{n-1} + \int_{t_{n-1}}^{t_{n-1}+h} \mathbf{V}_i^{n-1} ds \tag{1.7}$$

iii) Using the momentum conservation between colloidal particles and the solvent, the hydrodynamic force and torque acting on each colloidal particle are computed with volume integrals within the particle domain as

$$\mathbf{F}_i^H = \frac{\rho}{h} \int \mathbf{dr}[\phi_i^n \left(\mathbf{u}^* - \mathbf{u}_p^{n-1}\right)] \tag{1.8}$$

and

$$\mathbf{N}_i^H = \frac{\rho}{h} \int \mathbf{dr}[(\mathbf{r} - \mathbf{R}_i^n) \times \phi_i^n \left(\mathbf{u}^* - \mathbf{u}_p^{n-1}\right)] \tag{1.9}$$

where $\phi\mathbf{u}_{\mathrm{p}}^{n-1}(\mathbf{r}) = \sum_i \phi_i^n(\mathbf{r}) \left(\mathbf{V}_i^{n-1} + \mathbf{\Omega}_i^{n-1} \times (\mathbf{r} - \mathbf{R}_i^n)\right)$ is the correct velocity field within the particle domain in which $\phi \simeq 1$. The translational velocity and rotational velocity of each colloidal particle are then calculated as

$$\mathbf{V}_i^n = \mathbf{V}_i^{n-1} + \frac{1}{M_i} \int_{t_{n-1}}^{t_{n-1}+h} \left(\mathbf{F}_i^H + \mathbf{F}_i^P + \mathbf{G}_i^V\right) ds \tag{1.10}$$

and

$$\mathbf{\Omega}_i^n = \mathbf{\Omega}_i^{n-1} + \mathbf{I}_i^{-1} \int_{t_{n-1}}^{t_{n-1}+h} \left(\mathbf{N}_i^H + \mathbf{G}_i^\Omega\right) ds \tag{1.11}$$

iv) To ensure the rigidity of the particles and the appropriate non-slip boundary conditions at the fluid/particle interface, the body force $\phi\mathbf{F}_{\mathrm{p}}$ is calculated as

$$\phi\mathbf{f}_{\mathrm{p}} = \frac{\phi\left(\mathbf{u}_{\mathrm{p}}^n - \mathbf{u}^*\right)}{h} - \frac{1}{\rho}\nabla p_{\mathrm{p}}. \tag{1.12}$$

The correcting pressure $p_{\rm p}$ is determined to make the resultant total velocity incompressible. This leads to the Poisson equation of $p_{\rm p}$:

$$\boldsymbol{\Delta} p_{\rm p} = \rho \frac{\nabla \cdot \phi \left(\mathbf{u}_{\rm p}^{n} - \mathbf{u}^{*} \right)}{h}. \tag{1.13}$$

v) Finally, we obtain the correct fluid velocity field as:

$$\mathbf{u}^{n} = \mathbf{u}^{*} + \phi \mathbf{f}_{\rm p} h. \tag{1.14}$$

Repetition of steps i) through v) provides a complete procedure to perform the DNS of colloidal dispersions.

1.4 Method of implementing shear flow

In a model which treats a dispersed medium as a continuum velocity field i.e., a fluid field, using periodic boundary conditions has two advantages. First, the bulk measurements of some systems can only be obtained with computer simulations when a periodic boundary condition is employed, because computational resources are finite. Second, in that model, highly accurate measurements of the dispersion are obtained by using a periodic boundary condition. To obtain measurements of the dispersion, the dominant fluid dynamics equation (such as Navier-Stokes equation) must be solved. The dominant fluid dynamics equation should be solved with the spectral method, in which the basis functions are trigonometric functions, namely, a Fourier series which is obtained using the fast Fourier transform (FFT), because there is no error based on the finite difference approximation.

However, when the system is in shear flow, a periodic boundary condition cannot be used because the shear flow violates the periodicity of the system. The spectral method in which the basis functions are a Fourier series also cannot be used. Several methods can be used to solve this problem.

1.4.A Fixed boundary conditions of velocity field and imposing Lees-Edwards boundary conditions

Fig. 1.1 (a) shows the schematic illustration of the method combining the Lees-Edwards boundary conditions[9] with the Chebyshev method, which is a spectral method in which the basis functions are Chebyshev functions.[10]

Although this method can solve non-periodic problems, we can not obtain highly accurate measurement of the dispersion. This method imposes a fixed boundary condition on the velocity

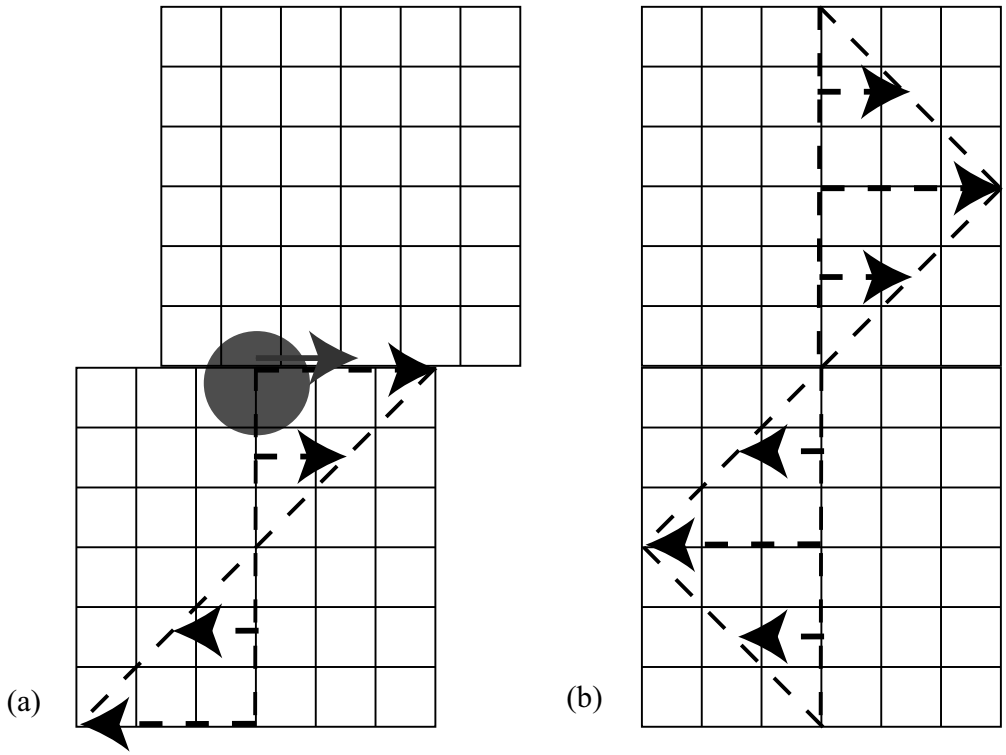

Figure 1.1: (a) The schematic illustration of the method combining the Lees-Edwards boundary conditions[9] with the Chebyshev method, particle velocity (gray arrow), fluid velocity (black arrow). (b)The schematic illustration of one simple technique to impose shear flow that maintains periodic boundary conditions, fluid velocity (black arrow).

field, and a difficult problem arises when a colloidal particle is on the boundary. In general, the particle velocity is different from the fluid velocity, which is always a fixed value, and a contradiction arises when the colloidal particle is on the boundary. To avoid this problem, a potential wall to repulse colloidal particles is necessary. In this case, the macroscopic properties of the bulk are not obtained, because the colloidal particles are confined in the limited space enclosed by the potential walls.

1.4.B Implementation of body force

Fig. 1.1 (b) shows the schematic illustration of one simple technique to impose shear flow that maintains periodic boundary conditions. This technique is to apply a spatially periodic external force to generate a periodic flow profile. The flow profile must be a zigzag profile to maintain the periodic boundary conditions. In this technique, bulk measurements cannot be accurately calculated because of unphysical kinks of the zigzag flow.

1.4.C Deformation lattice

This method is to solve the dominant equation of fluid dynamics in deformed (oblique) coordinates. Onuki proposed a general methodology of this to examine the phase transition dynamics and rheology in a shear flow.[11] Although this method is excellent, a hard problem appears when one treat the boundary between the particle and fluids. Thus, this method has never been successfully used in a dispersion system.

With these methods mentioned above, bulk measurements of a colloidal dispersion in a shear flow are not calculated. In this dissertation, a general methodology was developed to solve the dynamics of a colloidal dispersion in oblique coordinates. With this method, bulk measurements of chain dispersions can be calculated.

1.5 Thesis objectives

To elucidate the dynamical behavior of chain dispersions, a few problems were computationally investigated using the mesoscale models. These problems are as follows:

- The problem of the dynamics of chain in a Newtonian fluid under shear flow
- The problem of the viscosity of chain dispersions

These problems were modelled using the Navier-Stokes and Newtonian equations. This dissertation is composed of five chapters as follows:

In **Chapter 2**, A general methodology is presented to perform direct numerical simulations of particle dispersions in a shear flow with Lees-Edwards periodic boundary conditions. The Navier-Stokes equation is solved in oblique coordinates to resolve the incompatibility of the fluid motions with the sheared geometry, and the force coupling between colloidal particles and the host fluid is imposed by using the smoothed profile method. The validity of the method is carefully examined by comparing the present numerical results with experimental viscosity data for particle dispersions in a wide range of volume fractions and shear rates including nonlinear shear-thinning regimes.

In **Chapter 3**, I present the numerical results for the dynamics of a single chain in steady shear flow. The chain is represented by a bead-spring model, and the smoothed profile method is used to accurately account for the effects of thermal fluctuations and hydrodynamic interactions acting on beads due to host fluids. It was observed that the chain undergoes tumbling motions and that its dimensionless frequency $F = 6\pi\eta\sigma^3\nu/k_{\mathrm{B}}T$ depends only on the Peclet number Pe with a power

law $F \propto Pe^{\alpha}$, where k_{B} is the Boltzmann constant, T is the temperature, and σ is the diameter of the beads. The exponent α clearly changes from 2/3 to 1 around the critical Peclet number, Pe_{c}, indicating that the crossover reflects the competition of thermal fluctuation and shear flow. The presented numerical results agree well with my theoretical analysis based on Jeffrey's work.

In **Chapter 4**, The intrinsic viscosity of a dilute dispersion of rigid rods is studied using a SPM which is a recently developed direct numerical simulation (DNS) method for particle dispersions . A reentrant transition from shear-thinning to the 2nd Newtonian regime is successfully reproduced in the present DNS results around a Peclet number Pe = 150, which is in good agreement with our theoretical prediction of Pe = 143, at which the dynamical crossover from Brownian to non-Brownian behavior takes place explained in **Chapter 3**. The viscosity undershoot is observed in our simulations before reaching the 2nd Newtonian regime. The physical mechanisms behind these behaviors are analyzed in detail.

In **Chapter 5**, the thesis is summarized

References

1 H. Chen, Y. Ding, and A. Lapkin, Powder Tech. **194**, 132 (2009).

2 G. Chauveteau, J. Rheol. **26**, 111 (1982).

3 P. E. Boukany, Y. T. Hu and S. Wang, Macromolecules **41**, 2644 (2008).

4 H. Tanaka and T. Araki, Phys. Rev. Lett. **85**, 1338 (2000).

5 Y. Nakayama and R. Yamamoto, Phys. Rev. E **71**, 036707 (2005).

6 Y. Nakayama, K. Kim, and R. Yamamoto, Eur. Phys. J. E **26**, 361 (2008).

7 T. Iwashita, Y. Nakayama, and R. Yamamoto, J. Phys. Soc. Jpn. **77** 074007 (2008).

8 T. Iwashita and R. Yamamoto, Phys. Rev. E **79** 031401 (2009).

9 A. W. Lees and S. F. Edwards, J. Phys. C **5**, 1921 (1972).

10 R. Peyret, Applied Mathematical Sciences Volume 148 Spectral Methods for Incompressible Viscous Flow, 39, Springer (2002).

11 A. Onuki, J. Phys. Soc. Jpn. **66**, 1836 (1997).

Chapter 2

Implementation of Lees-Edwards periodic boundary conditions for direct numerical simulations of particle dispersions under shear flow

2.1 Introduction

Understanding the rheological properties of particle dispersions has been an important problem in many fields of science and engineering. When a dispersion is subjected to shear flow, the flow properties of the dispersion show a variety of non-Newtonian behaviors such as shear thinning and shear thickening. These non-Newtonian behaviors are associated with the changing microstructures of the dispersion, and several different physical mechanisms for these peculiar behaviors have been proposed.

In recent years, several numerical methods have been developed to accurately simulate particle dispersions, and they are all based on a similar approach, which involves resolving the fluid motion simultaneously with the particle motion. I refer to this approach as direct numerical simulation (DNS). Recently, Nakayama and Yamamoto have developed a numerical method, which we call the smoothed profile method (SPM), for the DNS of particulate flows.[1–4] In the SPM, the Navier-Stokes equation for the fluid motion is discretized on a fixed grid, and the Newton's and Euler's equations for the particle motion are solved simultaneously with the fluid motion. One simple technique to impose shear flow with the DNS approach that maintains conventional cubic periodic boundary conditions is to apply a spatially periodic external force to generate a periodic flow profile. Iwashita have successfully used a zigzag flow profile to impose both steady and oscillatory shear flows in the DNS of spherical particle dispersions.[3,4]

When a zero-wavevector shear flow is required, the usual cubic periodic boundary conditions must be modified to be compatible with a time-dependent shear deformation of the simulation cell. Such a modification was proposed by Lees and Edwards[5] and is commonly used in various simulation studies. The Lees-Edwards boundary conditions can be very easily implemented for particle-based simulations such as molecular dynamics simulations. However, care must be taken to implement these conditions in continuum grid-based simulations such as computational fluid

dynamics or time-dependent Ginzburg-Landau equations. The most useful implementation of the Lees-Edwards periodic boundary conditions for grid-based simulations is to solve the dynamic equations in deformed (oblique) coordinates.[6–8] Onuki proposed a general methodology to examine the phase transition dynamics and rheology in the presence of shear flow,[6] and it has been successfully used in several simulation studies and particularly for polymeric fluids in shear flow.[9–12]

The aim of this chapter is to propose a method to implement the Lees-Edwards periodic boundary conditions to simulate dispersions of solid particles in host fluids by the combinatory use of the SPM and the oblique coordinates.

2.2 Method

In the SPM, the equation governing the dynamics of particle dispersion is a modified Navier-Stokes equation:

$$\rho\left\{\frac{\partial \mathbf{u}}{\partial t}+(\mathbf{u}\cdot\nabla)\mathbf{u}\right\}=\nabla\cdot\boldsymbol{\sigma}+\rho\phi\mathbf{f}_{\mathrm{p}}-K\rho(u_x-\dot{\gamma}y)\mathbf{e}_x \tag{2.1}$$

with the condition of incompressibility $\nabla\cdot\mathbf{u}=0$, where ρ is the solvent density,

$$\boldsymbol{\sigma}=-p\mathbf{I}+\eta_{\mathrm{f}}\left\{\nabla\mathbf{u}+(\nabla\mathbf{u})^T\right\} \tag{2.2}$$

is the Newtonian stress tensor with a solvent viscosity of η_{f}, and $\mathbf{u}(\mathbf{r},t)$ and $p(\mathbf{r},t)$ are the velocity and pressure of the dispersion, respectively. A smoothed profile function $0\leq\phi(\mathbf{r},t)\leq 1$ distinguishes between the fluid and particle domains as well as yields $\phi=1$ in the particle domain and $\phi=0$ in the fluid domain. These domains are separated by thin interstitial regions with thicknesses characterized by ξ. The dispersion density ρ is represented as

$$\rho=(1-\phi)\rho_{\mathrm{f}}+\phi\rho_{\mathrm{p}} \tag{2.3}$$

where ρ_{f} and ρ_{p} are the solvent and particle densities, respectively. Only neutral buoyancy dispersions with $\rho=\rho_{\mathrm{f}}=\rho_{\mathrm{p}}$ are simulated in the present study. The body force $\phi\mathbf{f}_{\mathrm{p}}$ is introduced to ensure the rigidity of the particles and the appropriate non-slip boundary condition at the fluid/particle interface. The mathematical expressions for ϕ and $\phi\mathbf{f}_{\mathrm{p}}$ are detailed in previous papers.[1,2] The last term in Eq.(2.1) represents the external force needed to maintain linear shear flow:

$$u_x=\dot{\gamma}y \tag{2.4}$$

where $\dot{\gamma}$ is the shear rate, and K is a constant that determines the amplitude of the external force. Here I impose only the zero-wavevector shear flow so that the averaged fluid velocity becomes compatible with Eq.(2.4).

The motion of the i-th particle in a dispersion is governed by Newton's and Euler's equations of motion:

$$M_i \frac{d}{dt}\mathbf{V}_i = \mathbf{F}_i^{\mathrm{H}} + \mathbf{F}_i^{\mathrm{P}} + \mathbf{G}_i^{V}, \quad \frac{d}{dt}\mathbf{R}_i = \mathbf{V}_i \tag{2.5}$$

$$\mathbf{I}_i \cdot \frac{d}{dt}\mathbf{\Omega}_i = \mathbf{N}_i^{\mathrm{H}} + \mathbf{G}_i^{\Omega} \tag{2.6}$$

where $\mathbf{R}_i$, $\mathbf{V}_i$, and $\mathbf{\Omega}_i$ are the position, translational velocity, and rotational velocity of the colloidal particles, respectively. M_i and $\mathbf{I}_i$ are the mass and the moment of inertia, and $\mathbf{F}_i^{\mathrm{H}}$ and $\mathbf{N}_i^{\mathrm{H}}$ are the hydrodynamic force and torque exerted by the solvent on the colloidal particles, respectively.[1,2] $\mathbf{G}_i^{\mathrm{v}}$ and $\mathbf{G}_i^{\Omega}$ are the random force and torque, respectively, due to thermal fluctuations. The temperature of the system is defined such that the long-term diffusive motion of the colloidal particles reproduces the Stokes-Einstein rule.[3,4] $\mathbf{F}_i^{\mathrm{P}}$ represents the potential force due to direct inter-particle interactions such as through the Coulombic and Lennard-Jones potentials.

Eqs.(2.1), (2.5), and (2.6) are solved simultaneously in the SPM. However, this task is not easy with an ordinary periodic boundary condition because Eq.(2.1) depends explicitly on y, which leads to a violation of the translational invariance. This problem can be eliminated by using oblique coordinates. Fig. 2.1 represents a schematic illustration of the present coordinate transform. At a time $t = t_0$, a spherical solid particle is located in a solvent in Fig. 2.1 (a) where the solvent is discretized into square grids in an ordinary rectangular coordinate system. In Fig. 2.1 (b), the grids are deformed due to the shear flow that is applied for $t > t_0$ while the shape of the solid particle is unchanged. The same situation is depicted in a transformed (oblique) frame in Fig. 2.1 (c) where the grid has not moved (i.e., it remains rectangular), but the shape of the solid particle changes over time due to the shear flow.

To formulate the oblique coordinate transformation based on tensor analysis, I began by re-defining the covariant basis $\hat{\mathbf{E}}_i$ and contravariant basis $\hat{\mathbf{E}}^i$ in oblique coordinates rather than using the expressions shown in the literature.[6–8] Fig. 2.2 provides a definition of the basis vectors. Using a rectangular unit vector, $\hat{\mathbf{E}}_i$ and $\hat{\mathbf{E}}^i$ are expressed as

$$\begin{array}{ll} \hat{\mathbf{E}}_1 = \mathbf{e}_x & \hat{\mathbf{E}}^1 = \mathbf{e}_x - \dot{\gamma} t \mathbf{e}_y \\ \hat{\mathbf{E}}_2 = \dot{\gamma} t \mathbf{e}_x + \mathbf{e}_y & \hat{\mathbf{E}}^2 = \mathbf{e}_y \\ \hat{\mathbf{E}}_3 = \mathbf{e}_z & \hat{\mathbf{E}}^3 = \mathbf{e}_z \end{array} \tag{2.7}$$

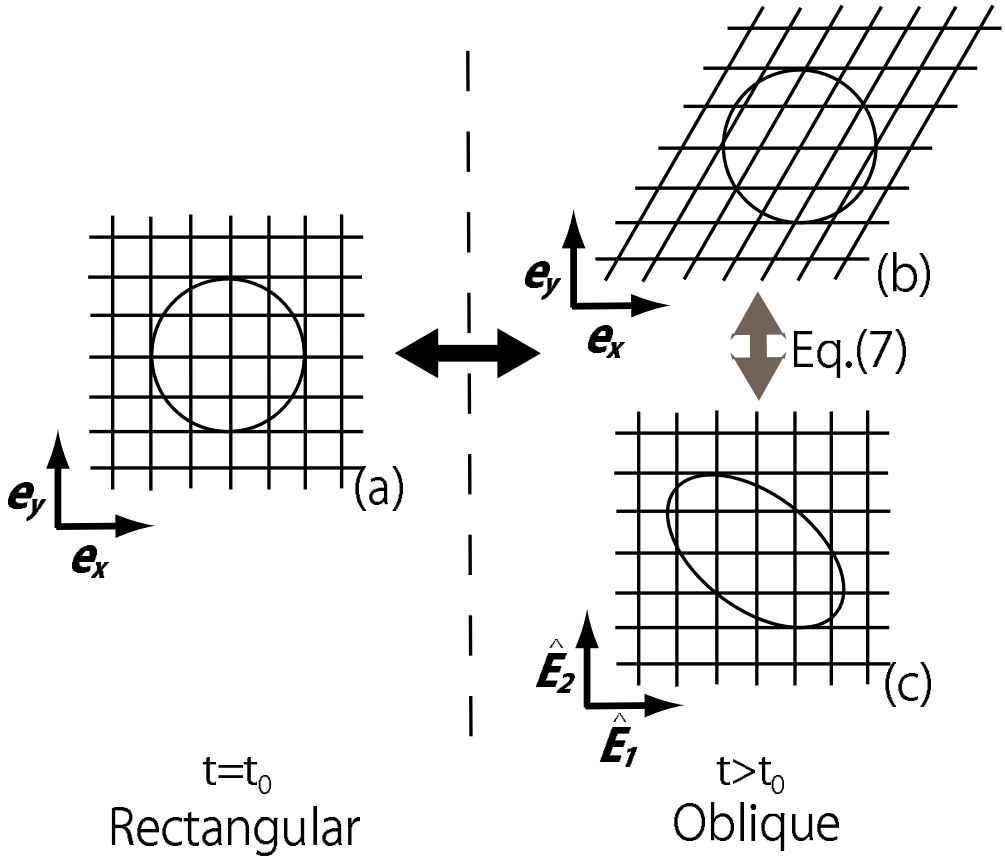

Figure 2.1: A schematic illustration of the present coordinate transformation. In (a), a spherical solid particle is in a solvent, which is discretized into grids in an ordinary rectangular coordinate system, at a time $t = t_0$. Since the shear flow is applied for $t > t_0$, the solvent (grids) is convected by the flow while the shape of the solid particle is unchanged. Such a situation is depicted in the original (experimental) frame in (b) and also in a transformed (oblique) frame in (c). The transformation between (b) and (c) is defined by Eq. (2.7).

where $\mathbf{e}_\alpha$ is the unit vector in the $\alpha(= x, y, z)$ direction in the original rectangular coordinate system. We can obtain contravariant (covariant) vector components A^i (A_i) using $\mathbf{A} \cdot \hat{\mathbf{E}}^i$ ($\mathbf{A} \cdot \hat{\mathbf{E}}_i$). The positional vector $\mathbf{r} \equiv x\mathbf{e}_x + y\mathbf{e}_y + z\mathbf{e}_z$ is transformed from the rectangular coordinate expression $\mathbf{r}$ to the oblique coordinate expression $\hat{\mathbf{r}}$ as follows:

$$\begin{aligned} \mathbf{r} &\equiv x\mathbf{e}_x + y\mathbf{e}_y + z\mathbf{e}_z \\ &= (\mathbf{r} \cdot \hat{\mathbf{E}}^1)\hat{\mathbf{E}}_1 + (\mathbf{r} \cdot \hat{\mathbf{E}}^2)\hat{\mathbf{E}}_2 + (\mathbf{r} \cdot \hat{\mathbf{E}}^3)\hat{\mathbf{E}}_3 \\ &= \hat{x}^1\hat{\mathbf{E}}_1 + \hat{x}^2\hat{\mathbf{E}}_2 + \hat{x}^3\hat{\mathbf{E}}_3 \equiv \hat{\mathbf{r}}, \end{aligned} \tag{2.8}$$

where the contravariant components $(\hat{x}^1, \hat{x}^2, \hat{x}^3)$ are expressed as

$$\begin{aligned} \hat{x}^1 &= x - \dot{\gamma} t y \\ \hat{x}^2 &= y \\ \hat{x}^3 &= z \end{aligned} \tag{2.9}$$

and the time in oblique coordinates is expressed as $\hat{t} = t$. Each contravariant component is trans-

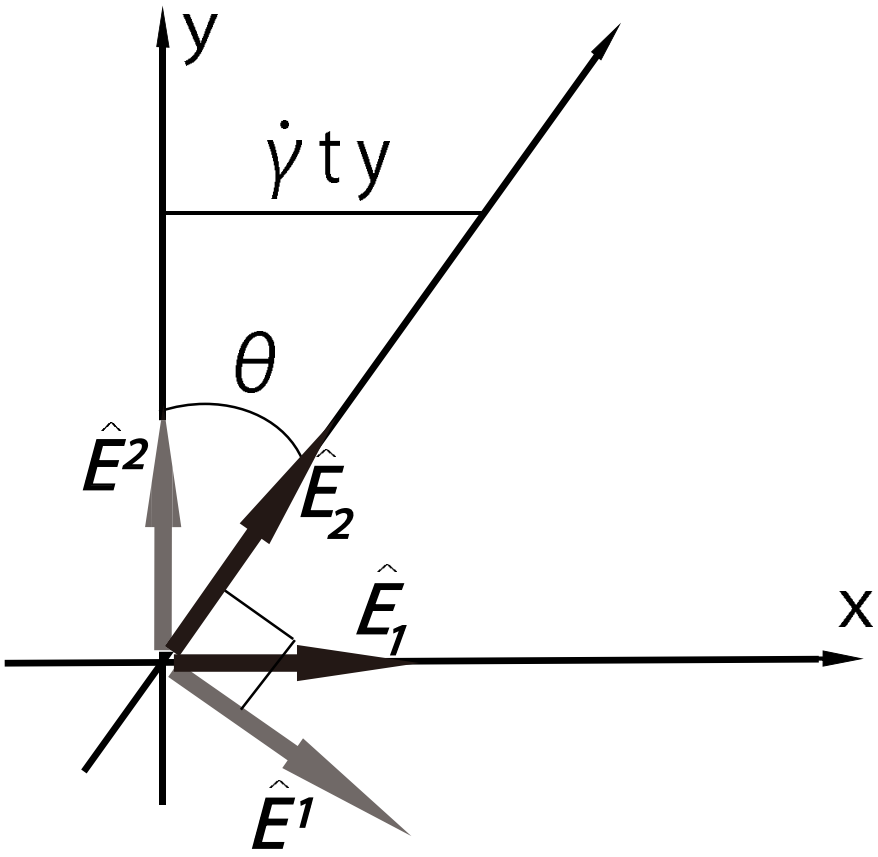

Figure 2.2: The definition of a basis vector.

formed to a covariant component by using the metric tensors $g_{ij} = \hat{\mathbf{E}}_i \cdot \hat{\mathbf{E}}_j$ and $g^{ij} = \hat{\mathbf{E}}^i \cdot \hat{\mathbf{E}}^j$. Then, the transformation can be expressed as

$$A^i = g^{ij} A_j \tag{2.10}$$

$$A_i = g_{ij} A^j \tag{2.11}$$

The physical quantities in Eq. (2.1) are transformed as indicated below:

$$\hat{p}(\hat{\mathbf{r}}, \hat{t}) = p(\mathbf{r}, t) \tag{2.12}$$

$$\hat{\phi}(\hat{\mathbf{r}}, \hat{t}) = \phi(\mathbf{r}, t) \tag{2.13}$$

$$\hat{\mathbf{u}}(\hat{\mathbf{r}}, \hat{t}) = \mathbf{u}(\mathbf{r}, t) - \dot{\gamma} y \mathbf{e}_x \tag{2.14}$$

$$\hat{\phi}\hat{\mathbf{f}}_{\mathrm{p}}(\hat{\mathbf{r}}, \hat{t}) = \phi \mathbf{f}_{\mathrm{p}}(\mathbf{r}, t) \tag{2.15}$$

In the oblique coordinate system, $\hat{\mathbf{u}}$ satisfies the standard periodic boundary conditions while $\mathbf{u}$ satisfies the Lees-Edwards periodic boundary conditions in the rectangular coordinate system. The

contravariant components $(\hat{u}^1, \hat{u}^2, \hat{u}^3)$ of $\hat{\mathbf{u}}$ are expressed as

$$\begin{aligned} \hat{u}^1 &= u_x - \dot{\gamma} t u_y - \dot{\gamma} y \\ \hat{u}^2 &= u_y \\ \hat{u}^3 &= u_z \end{aligned} \tag{2.16}$$

where (u_x, u_y, u_z) are the rectangular components of $\mathbf{u}$. The contravariant components of $\hat{\phi}\hat{\mathbf{f}}_{\mathrm{p}}$ are $(\hat{\phi}\hat{f}_{\mathrm{p}}^1, \hat{\phi}\hat{f}_{\mathrm{p}}^2, \hat{\phi}\hat{f}_{\mathrm{p}}^3)$ and can be expressed as

$$\begin{aligned} \hat{\phi}\hat{f}_{\mathrm{p}}{}^1 &= \phi f_{\mathrm{p}}^x - \dot{\gamma} t \phi f_{\mathrm{p}}^y \\ \hat{\phi}\hat{f}_{\mathrm{p}}{}^2 &= \phi f_{\mathrm{p}}^y \\ \hat{\phi}\hat{f}_{\mathrm{p}}{}^3 &= \phi f_{\mathrm{p}}^z \end{aligned} \tag{2.17}$$

where $(f_{\mathrm{p}}^x, f_{\mathrm{p}}^y, f_{\mathrm{p}}^z)$ are the rectangular components of $\mathbf{f}_{\mathrm{p}}$.

The differential operators in oblique coordinates are defined by

$$\hat{\nabla} = \hat{\mathbf{E}}^1 \frac{\partial}{\partial \hat{x}^1} + \hat{\mathbf{E}}^2 \frac{\partial}{\partial \hat{x}^2} + \hat{\mathbf{E}}^3 \frac{\partial}{\partial \hat{x}^3} \tag{2.18}$$

$$\frac{\partial}{\partial \hat{t}} = \frac{\partial}{\partial t} + \dot{\gamma} y \frac{\partial}{\partial x} \tag{2.19}$$

Therefore, the Laplacian operator in oblique coordinates is expressed as

$$\hat{\mathbf{\Delta}} = \left(\frac{\partial}{\partial \hat{x}^1} \right)^2 + \left(\frac{\partial}{\partial \hat{x}^2} - \dot{\gamma} t \frac{\partial}{\partial \hat{x}^1} \right)^2 + \left(\frac{\partial}{\partial \hat{x}^3} \right)^2 \tag{2.20}$$

Using these formula, Eqs. (2.1) and (2.2) are rewritten in oblique coordinates as

$$\begin{aligned} &\rho \left\{ \frac{\partial \hat{\mathbf{u}}}{\partial \hat{t}} + (\hat{\mathbf{u}} \cdot \hat{\nabla}) \hat{\mathbf{u}} \right\} \\ &\quad = \hat{\nabla} \cdot \hat{\boldsymbol{\sigma}} + \rho \hat{\phi} \hat{\mathbf{f}}_{\mathrm{p}} - \rho \dot{\gamma} \hat{u}^2 \hat{\mathbf{E}}_1 - K \rho (\hat{u}^1 + \gamma \hat{u}^2) \hat{\mathbf{E}}_{\mathbf{1}} \end{aligned} \tag{2.21}$$

and

$$\hat{\sigma}^{ij}(\hat{\mathbf{r}}, \hat{t}) = -g^{ij} \hat{p}(\hat{\mathbf{r}}, \hat{t}) + \eta_{\mathrm{f}} \left\{ g^{in} \frac{\partial \hat{u}^j}{\partial \hat{x}^n} + g^{jm} \frac{\partial \hat{u}^i}{\partial \hat{x}^m} \right\} \tag{2.22}$$

with the incompressibility condition $\hat{\nabla} \cdot \hat{\mathbf{u}} = 0$. Because Eq. (2.21) and $\hat{\mathbf{u}}$ satisfy the periodic boundary conditions in all directions, a fast Fourier transformation (FFT) can be safely used to solve the Poisson equation, which is needed to determine $\hat{p}$ with the incompressibility condition. In Appendix 1, detailed explanations are given on how to solve Eq. (2.21) with the incompressibility condition in the oblique coordinate system with using the spectral (Fourier) method.

When $\gamma \equiv \dot{\gamma} t = 1$, the positions $\hat{\mathbf{r}} = (\hat{x}^1, \hat{x}^2, \hat{x}^3)$ on an oblique grid with γ can be mapped onto the identical positions $\mathbf{r} = (x, y, z)$ on the original rectangular grid with $\gamma = 0$ using the operation $x = \hat{x}^1 + \hat{x}^2$, $y = \hat{x}^2$, $z = \hat{x}^3$. The shear strain γ is then reset to 0.[6] Repeating this process

allows us to perform stable numerical calculations over a long period with keeping $0 \leq \gamma \leq 1$. The above coordinate transformation based on the tensor analysis leads to the same expression for the Laplacian $\hat{\mathbf{\Delta}}$ as that of a previous study.[6] However, a difference arises between the differential operators $\hat{\nabla}$ for which my formal transformation derives a much simpler expression as shown in Eq. (2.18).

I calculate the dynamics of solid particle dispersions in shear flow by following these steps:

i) The fluid velocity field in the oblique coordinate system at a new time $t = nh$ is calculated by integrating Eq. (2.21) over time with $\hat{\phi}\hat{\mathbf{f}_{\mathrm{p}}} = 0$ as

$$\begin{aligned} &\hat{\mathbf{u}}^* = \hat{\mathbf{u}}^{n-1} + \\ &\int_{t_{n-1}}^{t_{n-1}+h} \left[\hat{\nabla} \cdot \left(\frac{1}{\rho} \hat{\boldsymbol{\sigma}} - \hat{\mathbf{u}}\hat{\mathbf{u}} \right) - \left\{ K(\hat{u}^1 + \gamma \hat{u}^2) + 2\dot{\gamma}\hat{u}^2 \right\} \hat{\mathbf{E}}_1 \right] ds \end{aligned} \tag{2.23}$$

while satisfying the incompressibility condition $\hat{\nabla} \cdot \hat{\mathbf{u}}^* = 0$. Here, the superscript n denotes the time step, and h is the time increment. In Appendix 1, detailed explanations are given also on how to solve Eq. (2.23) with using the spectral method.

ii) The velocity field $\hat{\mathbf{u}}^*$ is transformed into rectangular coordinates $\mathbf{u}^*$ using the inverse transformation expressed as

$$\begin{aligned} u_x &= \hat{u}^1 + \dot{\gamma} t \hat{u}^2 + \dot{\gamma}\hat{x}^2 \\ u_y &= \hat{u}^2 \\ u_z &= \hat{u}^3. \end{aligned} \tag{2.24}$$

iii) The motions of colloidal particles are only calculated in rectangular coordinates. The position of each colloidal particle is calculated by

$$\mathbf{R}_i^n = \mathbf{R}_i^{n-1} + \int_{t_{n-1}}^{t_{n-1}+h} \mathbf{V}_i^{n-1} ds \tag{2.25}$$

iv) Using the momentum conservation between colloidal particles and the solvent, the hydrodynamic force and torque acting on each colloidal particle are computed with volume integrals within the particle domain as

$$\mathbf{F}_i^H = \frac{\rho}{h} \int \mathbf{dr} [\phi_i^n \left(\mathbf{u}^* - \mathbf{u}_p^{n-1} \right)] \tag{2.26}$$

and

$$\mathbf{N}_i^H = \frac{\rho}{h} \int \mathbf{dr} [(\mathbf{r} - \mathbf{R}_i^n) \times \phi_i^n \left(\mathbf{u}^* - \mathbf{u}_p^{n-1} \right)] \tag{2.27}$$

where $\phi \mathbf{u}_{\mathrm{p}}^{n-1}(\mathbf{r}) = \sum_i \phi_i^n(\mathbf{r}) \left(\mathbf{V}_i^{n-1} + \mathbf{\Omega}_i^{n-1} \times (\mathbf{r} - \mathbf{R}_i^n) \right)$ is the correct velocity field within the particle domain in which $\phi \simeq 1$. The space integrals in Eqs.(2.26) and (2.27) are carried out by

summations over grid points in actual computations, however, there occur grid mismatch between $\mathbf{u}^*$ which is supported on oblique grid points $\hat{\mathbf{r}}_{\hat{i},\hat{j},\hat{k}}$ and other variables (ϕ_i^n and $\phi\mathbf{u}_{\rm p}^{n-1}$) which are supported on rectangular grid points $\mathbf{r}_{i,j,k}$. We determine values of $\mathbf{u}^*$ on rectangular grid points $\mathbf{r}_{i,j,k}$ by linear interpolation as described in detail in Appendix 2. The translational velocity and rotational velocity of each colloidal particle are then calculated as

$$\mathbf{V}_i^n = \mathbf{V}_i^{n-1} + \frac{1}{M_i}\int_{t_{n-1}}^{t_{n-1}+h} \left(\mathbf{F}_i^H + \mathbf{F}_i^P + \mathbf{G}_i^V\right) ds \tag{2.28}$$

and

$$\mathbf{\Omega}_i^n = \mathbf{\Omega}_i^{n-1} + \mathbf{I}_i^{-1}\int_{t_{n-1}}^{t_{n-1}+h} \left(\mathbf{N}_i^H + \mathbf{G}_i^\Omega\right) ds \tag{2.29}$$

v) To ensure the rigidity of the particles and the appropriate non-slip boundary conditions at the fluid/particle interface, the body force $\phi\mathbf{F}_{\rm p}$ is calculated as

$$\phi\mathbf{f}_{\rm p} = \frac{\phi\left(\mathbf{u}_{\rm p}^n - \mathbf{u}^*\right)}{h} - \frac{1}{\rho}\nabla p_{\rm p}. \tag{2.30}$$

The correcting pressure $p_{\rm p}$ is determined to make the resultant total velocity incompressible. This leads to the Poisson equation of $p_{\rm p}$:

$$\mathbf{\Delta} p_{\rm p} = \rho\frac{\nabla\cdot\phi\left(\mathbf{u}_{\rm p}^n - \mathbf{u}^*\right)}{h}. \tag{2.31}$$

We then transform $\phi\mathbf{f}_{\rm p}$ into oblique coordinates $\hat{\phi}\hat{\mathbf{f}}_{\rm p}$ using Eqs. (2.15) and (2.17).

vi) Finally, we obtain the correct fluid velocity field as:

$$\hat{\mathbf{u}}^n = \hat{\mathbf{u}}^* + \hat{\phi}\hat{\mathbf{f}}_{\rm p}h. \tag{2.32}$$

Repetition of steps i) through vi) provides a complete procedure to perform the DNS of colloidal dispersions under shear flow.

We can calculate the stress tensor of the dispersion $\langle\mathbf{s}\rangle$ and the dispersion viscosity $\eta = \langle s_{xy}\rangle/\dot{\gamma}$ in the following manner where $\langle\cdots\rangle$ denotes averaging over space and time. The equation governing the dispersion is formally written as:

$$\frac{D}{Dt}(\rho\mathbf{u}) = \nabla\cdot\boldsymbol{\sigma}^{\rm dis} - K\rho(u_x - \dot{\gamma}y)\mathbf{e}_x \tag{2.33}$$

By comparing Eq. (2.1) with Eq. (2.33), we get the formula

$$\nabla\cdot\boldsymbol{\sigma}^{\rm dis} = \nabla\cdot\boldsymbol{\sigma} + \rho\phi\mathbf{f}_{\rm p}. \tag{2.34}$$

The full stress tensor $\mathbf{s}$ of the flowing dispersion is then defined by introducing a convective momentum-flux tensor explicitly as

$$\mathbf{s} = \boldsymbol{\sigma}^{\mathrm{dis}} - \rho \mathbf{u}\mathbf{u}. \tag{2.35}$$

The definitions of $\boldsymbol{\sigma}^{\mathrm{dis}}$ and $\mathbf{s}$ are identical to the definitions in Iwashita's paper.[4] Now, we can evaluate the average stress tensor of the dispersion $\langle \mathbf{s} \rangle$ directly from Eqs. (2.34), (2.35), and $\delta\boldsymbol{\sigma} = \mathbf{s} - \boldsymbol{\sigma}$ as

$$\begin{aligned}
\langle \mathbf{s} \rangle =& \langle \boldsymbol{\sigma} \rangle + \frac{1}{V} \left\langle \int \mathbf{dr} \delta\boldsymbol{\sigma} \right\rangle_t \\
=& \langle \boldsymbol{\sigma} \rangle + \frac{1}{V} \left\langle \int \mathbf{dr} \left[(\nabla \cdot (\delta\boldsymbol{\sigma}\mathbf{r}))^T - \mathbf{r}\nabla \cdot \delta\boldsymbol{\sigma} \right] \right\rangle_t \\
=& \langle \boldsymbol{\sigma} \rangle - \frac{1}{V} \left\langle \int \mathbf{drr} \nabla \cdot \delta\boldsymbol{\sigma} \right\rangle_t \\
=& \langle \boldsymbol{\sigma} \rangle - \frac{1}{V} \left\langle \int \mathbf{drr} \rho\phi \mathbf{f}_{\mathrm{p}} \right\rangle_t + \frac{1}{V} \left\langle \int \mathbf{drru} \cdot \nabla(\rho\mathbf{u}) \right\rangle_t \\
=& \langle \boldsymbol{\sigma} \rangle - \frac{1}{V} \left\langle \int \mathbf{drr} \rho\phi \mathbf{f}_{\mathrm{p}} \right\rangle_t
\end{aligned} \tag{2.36}$$

with the volume $V = L_x L_y L_z$ where L_i is the system size in i-direction. $\langle \cdots \rangle_t$ denotes time averaging over steady state. In the derivation of the second formula, I used a second rank identity. If we substitute Eq. (2.34) into the third formula, then we obtain the fourth formula. The fifth formula can be obtained by assuming that the system is in a steady state in which $\left\langle \frac{d}{dt} (\rho\mathbf{u}) \right\rangle_t = \left\langle \frac{\partial}{\partial t} (\rho\mathbf{u}) + \mathbf{u} \cdot \nabla(\rho\mathbf{u}) \right\rangle_t = 0$ and $\left\langle \frac{\partial}{\partial t} (\rho\mathbf{u}) \right\rangle_t = 0$.

2.3 Results

Using the method described above, I calculated the high- and low-shear limiting viscosities of colloidal dispersions for various volume fractions of particles Φ. The particles interact via a truncated Mie (m, n) potential with $m = 36$ and $n = 18$.[13]

$$U(r) = \begin{cases} 4\epsilon \left\{ \left(\frac{\sigma}{r} \right)^{36} - \left(\frac{\sigma}{r} \right)^{18} \right\} + \epsilon & (r < 2^{\frac{1}{18}}\sigma), \\ 0 & (r > 2^{\frac{1}{18}}\sigma), \end{cases} \tag{2.37}$$

where r is the distance between the centers of a pair of particles. The parameter ϵ characterizes the strength of the interactions, and σ represents the diameter of the colloidal particles. The lattice spacing δx is taken to be the unit of length. The unit of time is given by $\rho_{\mathrm{f}} \delta x^2 / \eta$ where $\eta = 1$ and $\rho_{\mathrm{f}} = \rho_{\mathrm{p}} = 1$. The system size is $L_x \times L_y \times L_z = 64 \times 64 \times 64$. Other parameters are set as follows: $\sigma = 8$, $\xi = 2$, $\epsilon = 1$, $\eta = 1$, $M_i = \pi\sigma^3/6$, and $h = 0.067$. The temperature is $k_{\mathrm{B}}T/\epsilon = 7$. The range of shear rate is $1.0 \times 10^{-4} < \dot{\gamma} < 0.1$.

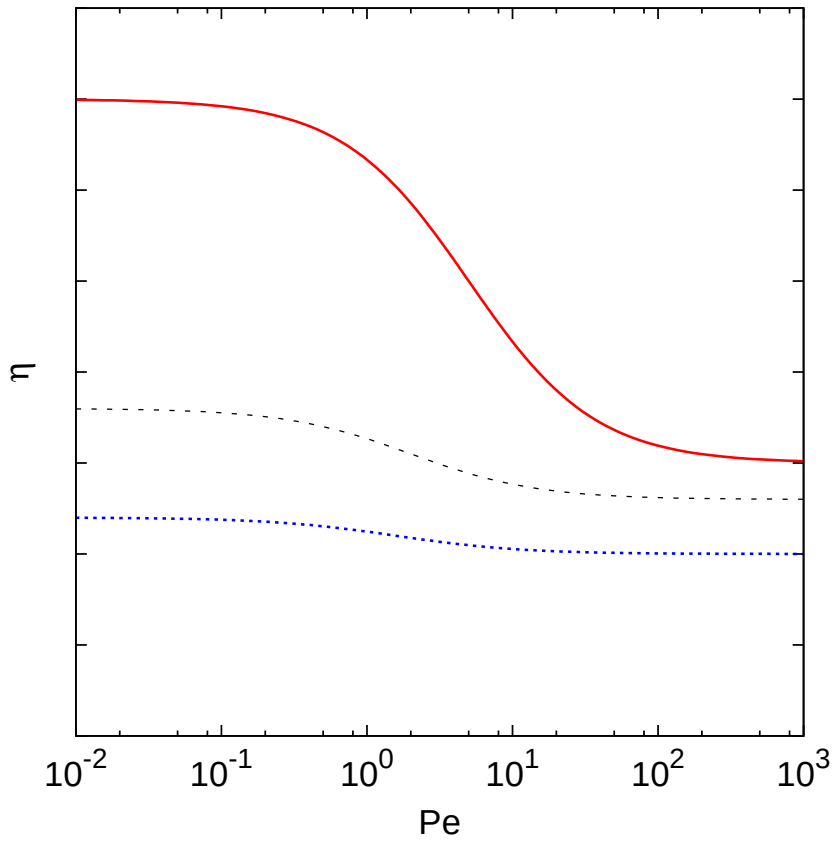

Figure 2.3: The schematic illustration of the behavior of the viscosity as a function of the Peclet number for several volume fractions. In descending order of volume fractions: solid line, dashed line, dotted line

The Fig. 2.3 shows the schematic illustration of the behavior of the viscosity as a function of the Peclet number for several volume fractions. Here, the Peclet number is defined as $Pe = 6\pi\eta\sigma^3\dot{\gamma}/k_{\mathrm{B}}T$. With increasing Pe, the shear-thinning behavior is clearly observed from the higher plateau region to a lower plateau region. From higher and lower plateau values of the viscosity curve, we can obtain the low shear limiting viscosity and the high shear limiting viscosity for each volume fraction.

The inset of Fig. 2.4 shows the dependence of the Newtonian viscosity on the volume fraction Φ when $\Phi \ll 1$. The present simulation data show very good agreement with Einstein's viscosity law. Fig. 2.4 shows the dependence of the low-shear limiting viscosity (closed symbols) and the high-shear limiting viscosity (open symbols) on the volume fraction. My simulation data for both high- and low-shear limiting viscosities show good agreement with the experimental results of van der Werff *et al.*[14] Previously, Brady theoretically predicted the behavior of the low-shear limiting

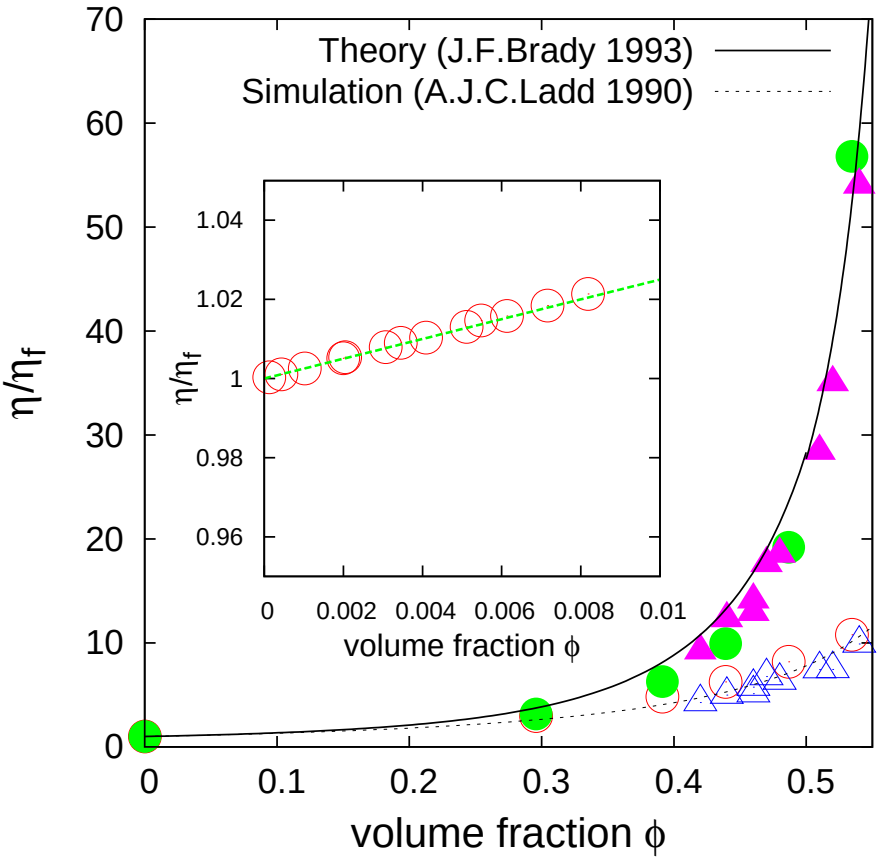

Figure 2.4: The behavior of the viscosity η as a function of the volume fraction Φ. The open symbols represent the high-shear limiting viscosity, and the closed symbols represent the low-shear limiting viscosity. The open and closed circles correspond to my simulation data, whereas the triangles correspond to experimental results.[14] The solid line is Brady's theoretical prediction,[15] and the dotted line is a fitting curve obtained from previous experimental[14] and simulation[16] data. The inset indicates a comparison of my present simulation data with Einstein's viscosity law (dashed-line) in the small volume fraction regime $\Phi < 0.01$ where the viscosity exhibits simple Newtonian behavior.

viscosity.[15] My simulation data show good agreement with Brady's prediction over a wide range of volume fractions $0 < \Phi < 0.55$. Ladd analyzed the behavior of the high-shear limiting viscosity using Stokesian dynamics.[16] My simulation data agree well with Ladd's simulation data and also with the theoretical results of Beenakker.[17]

Finally, I add some comments on the differences between the present method using Lees-Edwards boundary condition and the previously proposed method using zigzag velocity profile.[18] I simulated a single spherical particle in shear flow using the two methods without thermal fluctuation. The volume fraction is 0.001. Figure 2.5 shows the ratio of angular velocity ω of a spherical particle to the applied shear rate $\dot{\gamma}$ as a function of $\dot{\gamma}$. Although the data using the present method tend to be slightly smaller than the data using the zigzag flow, deviations of both data from the

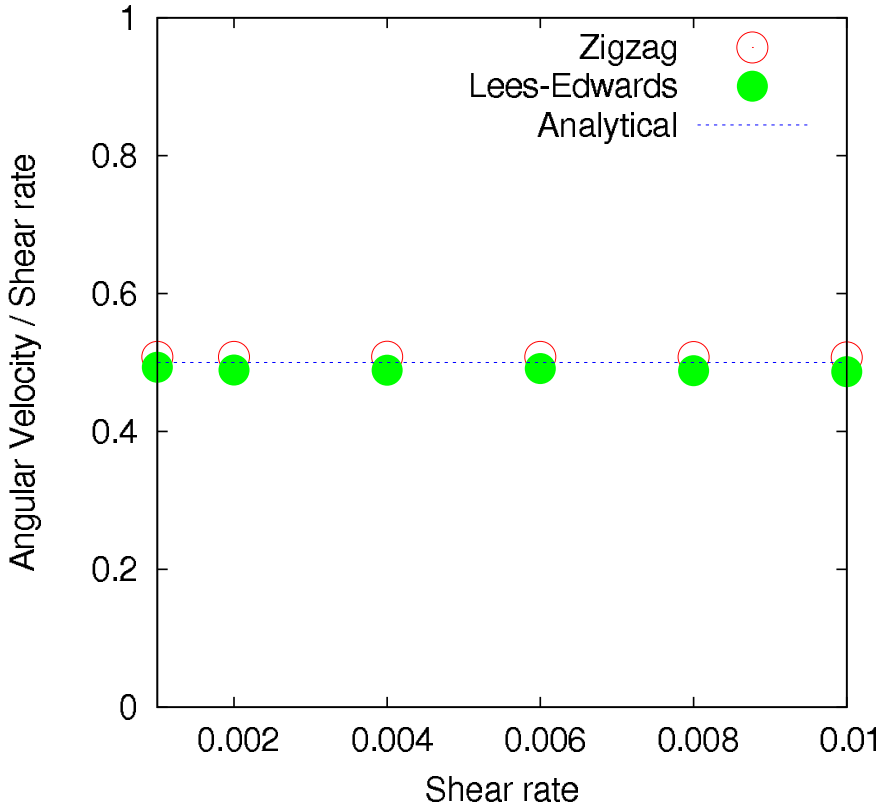

Figure 2.5: The behavior of the ratio of angular velocity ω to the shear rate $\dot{\gamma}$ as a function of $\dot{\gamma}$. Open circles indicate the results of the previous method. Closed circles indicate the results of the present method. The solid line corresponds to the analytical solution.

analytical value $\omega/\dot{\gamma} = 0.5$ remain small within numerical errors of the methods. Figure 2.6 shows the intrinsic viscosity $[\eta]$ of the dilute dispersion as a function of shear rate $\dot{\gamma}$. The simulation data using the present method almost perfectly follow onto the Einstein's prediction $[\eta] = 2.5$, while the data using zigzag flow slightly overestimate $[\eta]$ because of unphysical kinks of the zigzag flow profile. This problem is not very serious when the shape of dispersed particles is spherical and the size of the particle is much smaller than the distance between two kinks. Serious problems, however, occur if this method is applied to non-dilute dispersions of chains or rods, for example. The present method using Lees-Edwards boundary condition is free from this problem.

2.4 Conclusion

I presented a generic methodology for performing DNS of particle dispersions in a shear flow using oblique coordinates and periodic boundary conditions. The validity of the method was confirmed by comparing the present numerical results with experimental viscosity data for particle dispersions over a wide range of the parameters Φ and $\dot{\gamma}$ that include nonlinear shear-thinning regimes. An

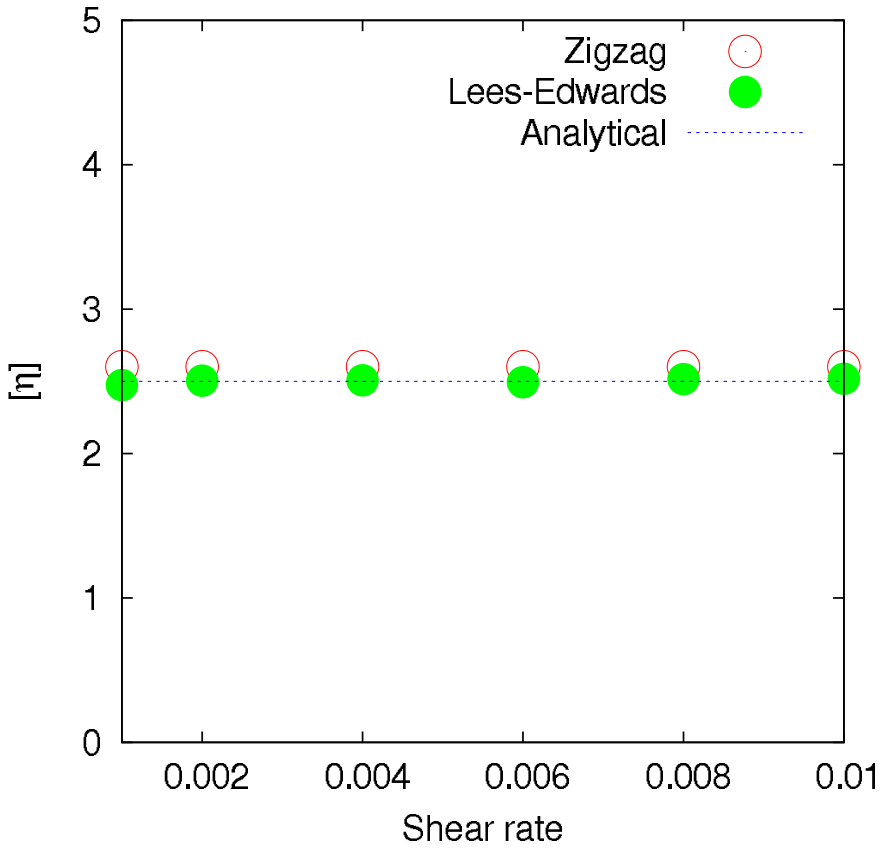

Figure 2.6: The behavior of the intrinsic viscosity as a function of shear rate $\dot{\gamma}$. Open circles indicate the results of the previous method. Closed circles indicate the results of the present method. The solid line corresponds to Einstein's viscosity law.

important advantage of the DNS approach over other approaches such as Stokesian dynamics is its applicability to particle dispersions in complex fluids. In fact, electrophoresis of charged colloids[19] and particle dispersions in nematic liquid crystals[20] have already been calculated using SPM. My methodology can also be applied to simulate particle dispersions in viscoelastic fluids simply by replacing the Newtonian constitutive equation to more complex ones such as Maxwell model.

Appendix 1

In this section, I describe how to solve Eq. (2.21) with the incompressibility condition in an oblique coordinate system using Fourier spectral methods. The Fourier and inverse Fourier transforms are defined as

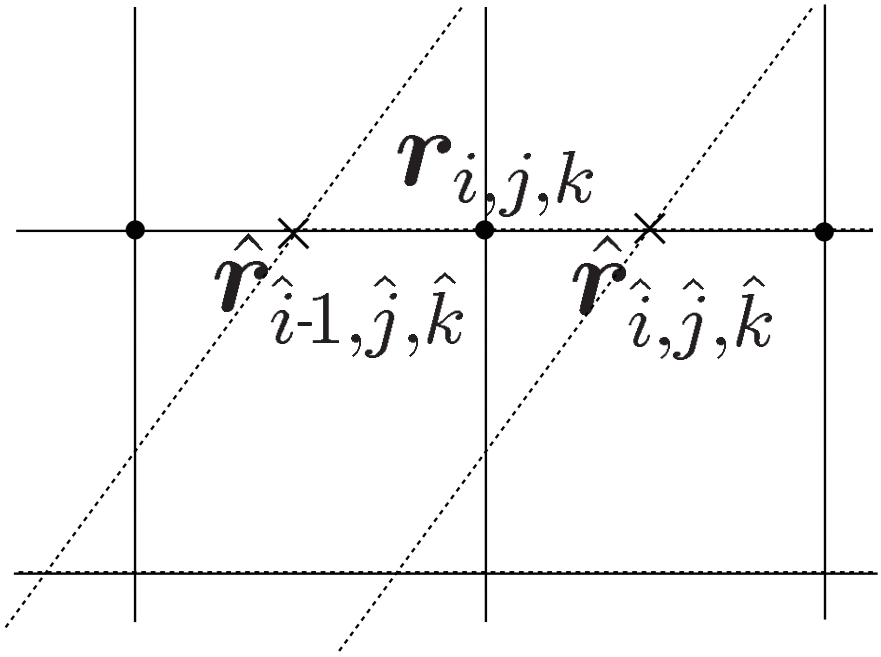

Figure 2.7: A schematic illustration of the lattice discordance between the oblique and rectangular coordinates. $\mathbf{r}_{i,j,k}$ is the location vector in a rectangular coordinate system. $\hat{\mathbf{r}}_{\hat{i}-1,\hat{j},\hat{k}}$ and $\hat{\mathbf{r}}_{\hat{i},\hat{j},\hat{k}}$ are the location vectors in the oblique coordinate system.

$$A(\hat{\mathbf{k}}) = \int A(\hat{\mathbf{r}}) \exp(-i\hat{\mathbf{k}} \cdot \hat{\mathbf{r}}) d\hat{\mathbf{r}} \tag{2.38}$$

$$A(\hat{\mathbf{r}}) = \frac{1}{(2\pi)^3} \int A(\hat{\mathbf{k}}) \exp(i\hat{\mathbf{k}} \cdot \hat{\mathbf{r}}) d\hat{\mathbf{k}}, \tag{2.39}$$

where $\hat{\mathbf{k}}$ is the wavevector of the oblique coordinate system. In $\hat{\mathbf{k}}$ space, we can express the spatial covariant derivative as

$$\frac{\partial A(\hat{\mathbf{r}})}{\partial \hat{x^\alpha}} \rightarrow ik_\alpha A(\hat{\mathbf{k}}). \tag{2.40}$$

where k_α is a covariant component of $\hat{\mathbf{k}}$.

Using these relations, we modify Eq. (2.23) from $\hat{\mathbf{r}}$ space to $\hat{\mathbf{k}}$ space. This equation is solved in $\hat{\mathbf{k}}$ space. First, by substituting Eq. (2.22) into Eq. (2.23), we obtain the explicit equation represented by

$$\begin{aligned}&\hat{\mathbf{u}}^*(\hat{\mathbf{r}}) = \hat{\mathbf{u}}(\hat{\mathbf{r}}) + \\ &\int_{t_{n-1}}^{t_{n-1}+h} \left[-(\hat{\mathbf{u}}(\hat{\mathbf{r}}) \cdot \hat{\nabla})\hat{\mathbf{u}}(\hat{\mathbf{r}}) - \hat{\nabla}\frac{\hat{p}(\hat{\mathbf{r}})}{\rho} + \nu\hat{\boldsymbol{\Delta}}\hat{\mathbf{u}}(\hat{\mathbf{r}}) - \left\{ K(\hat{u}^1(\hat{\mathbf{r}}) + \gamma\hat{u}^2(\hat{\mathbf{r}})) + 2\dot{\gamma}\hat{u}^2(\hat{\mathbf{r}}) \right\} \hat{\mathbf{E}}_1 \right] ds,\end{aligned} \tag{2.41}$$

where $\nu = \eta_\mathrm{f}/\rho$ is the kinetic viscosity. Using a Fourier transform, the form of Eq. (2.41) in $\hat{\mathbf{k}}$

space is written as

$$\hat{\mathbf{u}}^*(\hat{\mathbf{k}}) = \hat{\mathbf{u}}(\hat{\mathbf{k}}) + \int_{t_{n-1}}^{t_{n-1}+h} \left[-\mathbf{F}(\hat{\mathbf{k}}) - \nu\hat{\mathbf{k}}^2\hat{\mathbf{u}}(\hat{\mathbf{k}}) - \left\{ K(\hat{u}^1(\hat{\mathbf{k}}) + \gamma\hat{u}^2(\hat{\mathbf{k}})) + 2\dot{\gamma}\hat{u}^2(\hat{\mathbf{k}}) \right\} \hat{\mathbf{E}}_1 \right]_\perp ds, \tag{2.42}$$

where

$$\mathbf{F}(\hat{\mathbf{k}}) = \int (\hat{\mathbf{u}}(\hat{\mathbf{r}}) \cdot \hat{\nabla})\hat{\mathbf{u}}(\hat{\mathbf{r}}) \exp(-i\hat{\mathbf{k}} \cdot \hat{\mathbf{r}}) d\hat{\mathbf{r}}. \tag{2.43}$$

The bracket $\left[\mathbf{A}(\hat{\mathbf{k}})\right]_\perp \left(\equiv \mathbf{A}(\hat{\mathbf{k}}) \cdot \left(\mathbf{I} - \frac{\hat{\mathbf{k}}\hat{\mathbf{k}}}{\hat{\mathbf{k}}^2} \right) \right)$ denotes taking the orthogonal part to $\hat{\mathbf{k}}$ and this operation corresponds to imposing the incompressibility condition $\hat{\nabla} \cdot \hat{\mathbf{u}}(\hat{\mathbf{r}}) = 0$ (or equivalently $\hat{\mathbf{k}} \cdot \hat{\mathbf{u}}(\hat{\mathbf{k}}) = 0$). Because $\hat{p}(\hat{\mathbf{r}})$ is automatically determined by imposing the condition of incompressibility, we can safely neglect this term.

Using the method describe above, we calculate $\hat{\mathbf{u}}^*(\hat{\mathbf{r}})$ from $\hat{\mathbf{u}}(\hat{\mathbf{r}})$ as shown in Eq. (2.23).

Appendix 2

An arbitrary position vector in the oblique coordinate system is defined as

$$\hat{\mathbf{r}}_{\hat{i},\hat{j},\hat{k}} = (\hat{i}\hat{\mathbf{E}}_1 + \hat{j}\hat{\mathbf{E}}_2 + \hat{k}\hat{\mathbf{E}}_3)\delta x \tag{2.44}$$

with arbitrary integer numbers $\hat{i}, \hat{j}, \hat{k}$, while a position vector in the rectangular coordinate system is defined as

$$\mathbf{r}_{i,j,k} = (i\mathbf{e}_x + j\mathbf{e}_x + k\mathbf{e}_x)\delta x \tag{2.45}$$

with integer numbers i, j, k, where δx represents the lattice spacing. In general, the two position vectors $\hat{\mathbf{r}}_{\hat{i},\hat{j},\hat{k}}$ and $\mathbf{r}_{i,j,k}$ are not compatible with each other. To transform from $\hat{\mathbf{r}}_{\hat{i},\hat{j},\hat{k}}$ to $\mathbf{r}_{i,j,k}$ using Eq. (2.9), i must equal $\hat{i} - \gamma\hat{j}$. However, $\gamma\hat{j}$ is not always an integer since γ is defined between 0 and 1. We thus perform interpolation of the variables to overcome this problem.

Fig. 2.7 shows a lattice discordance between the rectangular and oblique coordinate systems. $\mathbf{r}_{i,j,k}$ is the location vector in rectangular coordinates, and $\hat{\mathbf{r}}_{\hat{i}-1,\hat{j},\hat{k}}$ and $\hat{\mathbf{r}}_{\hat{i},\hat{j},\hat{k}}$ are the location vectors in oblique coordinates. Using liner interpolation, we estimate the velocity field in rectangular coordinates $\mathbf{u}(\mathbf{r}_{i,j,k})$ from the velocity field in oblique coordinates $\mathbf{u}(\hat{\mathbf{r}}_{\hat{i}-1,\hat{j},\hat{k}})$ and $\mathbf{u}(\hat{\mathbf{r}}_{\hat{i},\hat{j},\hat{k}})$. From the liner interpolation, $\mathbf{u}(\mathbf{r}_{i,j,k})$ along the straight line is given by the equation

$$\mathbf{u}(\mathbf{r}_{i,j,k}) = \frac{|\hat{\mathbf{r}}_{\hat{i},\hat{j},\hat{k}} - \mathbf{r}_{i,j,k}|}{|\hat{\mathbf{r}}_{\hat{i},\hat{j},\hat{k}} - \hat{\mathbf{r}}_{\hat{i}-1,\hat{j},\hat{k}}|}\mathbf{u}(\hat{\mathbf{r}}_{\hat{i}-1,\hat{j},\hat{k}}) + \frac{|\hat{\mathbf{r}}_{\hat{i}-1,\hat{j},\hat{k}} - \mathbf{r}_{i,j,k}|}{|\hat{\mathbf{r}}_{\hat{i},\hat{j},\hat{k}} - \hat{\mathbf{r}}_{\hat{i}-1,\hat{j},\hat{k}}|}\mathbf{u}(\hat{\mathbf{r}}_{\hat{i},\hat{j},\hat{k}}). \tag{2.46}$$

When using liner interpolation, artificial diffusion may arise. To check the reliability of the present method, I calculate the angular velocity ω and intrinsic viscosity $[\eta] = \lim_{\Phi \to 0}(\eta - \eta_f)/\Phi$ for a dilute dispersion of spherical particle for which analytical solutions are available. As already shown in Figs. 2.5 and 2.6, the present simulation data agree very well with analytical solutions indicating that the effects of artificial numerical diffusion are not serious.

References

1 Y. Nakayama and R. Yamamoto, Phys. Rev. E **71**, 036707 (2005).

2 Y. Nakayama, K. Kim, and R. Yamamoto, Eur. Phys. J. E **26**, 361 (2008).

3 T. Iwashita, Y. Nakayama, and R. Yamamoto, J. Phys. Soc. Jpn. **77** 074007 (2008).

4 T. Iwashita and R. Yamamoto, Phys. Rev. E **79** 031401 (2009).

5 A. W. Lees and S. F. Edwards, J. Phys. C **5**, 1921 (1972).

6 A. Onuki, J. Phys. Soc. Jpn. **66**, 1836 (1997).

7 S. Toh, K. Ohkitani, and M. Yamada, Physica D **51**, 569 (1991).

8 R. S. Rogallo, NASA Tech. Mem., 81315 (1981).

9 A. Onuki, R. Yamamoto, and T. Taniguchi, J. Phys. II France **7**, 295 (1997).

10 Z. Zhang, H. Zhang, and Y. Yang, J. Chem. Phys. **115**, 7783 (2001).

11 T. Imaeda, A. Furukawa, A. Onuki, Phys. Rev. E **70**, 051503 (2004).

12 S. Nishitsuji, M. Takenaka, T. Taniguchi, Polymer **51**, 1853 (2010).

13 G. Mie, Annalen der Physik **11**, 657 (1903).

14 J. C. van der Werff, C. G. de Kruif, C. Blom, and J. Mellema, Phys. Rev. A **39**, 795 (1989).

15 J. F. Brady, J. Chem. Phys. **99**, 567 (1993).

16 A. J. C. Ladd, J. Chem. Phys. **93**, 3484 (1990).

17 C. W. J. Beenakker, Physica A **128**, 48 (1984).

18 T. Iwashita, R. Yamamoto, Phys. Rev. E **80**, 061402 (2009).

19 K. Kim, Y. Nakayama, R. Yamamoto, Phys. Rev. Lett. **96**, 208302 (2006).

20 R. Yamamoto, Phys. Rev. Lett. **87**, 075502 (2001).

Chapter 3

Tumbling motion of a single chain in shear flow: a crossover from Brownian to non-Brownian behavior

3.1 Introduction

The dynamics of solid particles dispersed in host fluids is an important problem in many different fields of science and engineering. The macroscopic properties of such dispersions (the elastic modulus, viscosity, and thermal and electric conductivities) greatly depend on the dynamics of the particles in the host fluids. In equilibrium states, the dynamics of small dispersed particles are strongly affected by the thermal fluctuations of their host fluids. When flow is imposed, the dynamics are also affected by the flow of the host fluids. Because it is difficult to experimentally analyze these complex particle dynamics, which are coupled both to thermal fluctuations and to fluid flow, numerical simulations are particularly important for understanding the properties of particle dispersions in detail.[1]

For a single Brownian chain fluctuating in the shear flow of a Newtonian fluid, it has been suggested that the tumbling frequency ν is proportional to the shear rate $\dot{\gamma}^{2/3}$.[2–9] This has been experimentally confirmed by Schroeder, Teixeira, Shaqfeh, and Chu[2] for the dynamics of individual DNA molecules in a linear shear flow. Primarily, Smith, Babcock, and Chu[10] measured the power spectral density (PSD) and the probability distribution function (PDF) of the extension length of each DNA molecule for various Weissenberg numbers $Wi = \dot{\gamma}\tau$, where $\dot{\gamma}$ is the shear rate and τ is the relaxation time of the chain orientation. The PSD of polymer extension exhibits no peaks. In subsequent experiments,[2,3] however, the focus has been put on the PSD of the orientation angle φ, where $\varphi = 0$ when the DNA molecule lies perfectly in the flow direction. These experimental results support a simple power law, $\nu\tau \propto Wi^{2/3}$, where ν is the peak frequency of the PSD. The relaxation time τ is considered to be a constant if the temperature is constant. This leads to $\nu \propto \dot{\gamma}^{2/3}$. Similar results have also been obtained in other experiments,[3,4] numerical simulations,[5,6] and theoretical analyses.[7–9] Although the DNA molecules mentioned above can be considered flexible chains, a quite similar power law was obtained using numerical simulations for a Brownian linear rigid rod as well.[2]

For a single non-Brownian (thermally non-fluctuating) flexible chain in shear flow, the tumbling frequency ν is expected to be proportional to the shear rate $\dot{\gamma}$.[11] A single non-Brownian rigid rod with a finite aspect ratio is known to exhibit a cyclic tumbling motion in shear flow, as described by Jeffrey's equation, $\nu \propto \dot{\gamma}$.[12–14]

From the above experimental findings, one would expect to observe a crossover from Brownian ($\nu \propto \dot{\gamma}^{2/3}$) to non-Brownian ($\nu \propto \dot{\gamma}$) behavior with increasing shear rate; however, such a clear crossover has not yet been reported. This crossover has not yet been successfully predicted by previous numerical[5,6] and theoretical[7–9] studies where a dispersed chain is treated as an end-to-end vector, namely, as an infinitely thin line. Therefore, the rotational motion of the chain cannot be sustained across $\varphi = 0$ without thermal fluctuations. When a thermal fluctuation exists, the orientation of the thin line can fluctuate around $\varphi = 0$. This leads to tumbling motions even for a thin line; however, the frequency of the tumbling motion ν is always proportional to $\dot{\gamma}^{2/3}$, regardless of the shear rate.[9]

I thus aim to analyze this crossover by use of a direct numerical simulation (DNS) approach. In this chapter, I simulated the tumbling motion of a chain using a smoothed profile method (SPM) that accurately takes into account thermal fluctuations and hydrodynamic interactions.[15–18] The chain is represented by a bead-spring model, wherein each bead is modeled as a spherical object with a finite radius a and undergoes free rotation. Rigid rods or flexible chains are represented with or without a constraint force on bond bending. Apart from the previous numerical models, the presented bead-spring model naturally takes into account the finite thickness of the experimentally used chains or rods. A theoretical analysis has also been developed to understand the mechanisms underlying the crossover.

3.2 Methods

3.2.A Model

I solve the dynamics of a single chain in a Newtonian solvent using SPM[15–18] explained in 1.3.A. This method enables us to calculate hydrodynamic interactions both efficiently and accurately, without neglecting many-body interactions. The equation governing a solvent with a density ρ_{f} and a shear viscosity η is a modified Navier-Stokes equation,

$$\rho_{\mathrm{f}}\left\{\frac{\partial \mathbf{u}}{\partial t}+(\mathbf{u}\cdot\nabla)\mathbf{u}\right\}=-\nabla p+\eta\boldsymbol{\Delta}\mathbf{u}+\rho_{\mathrm{f}}\phi\mathbf{f}_{\mathrm{p}}+\mathbf{f}_{\mathrm{shear}} \tag{3.1}$$

with the incompressible condition $\nabla\cdot\mathbf{u}=0$, where $\mathbf{u}(\mathbf{r},t)$ and $p(\mathbf{r},t)$ are the velocity and pressure fields of the solvent, respectively. A smoothed profile function $0\leq\phi(\mathbf{r},t)\leq 1$ distinguishes between the fluid and particle domains, yielding $\phi=1$ in the particle domain and $\phi=0$ in the fluid domain. The body force $\phi\mathbf{f}_{\mathrm{p}}$ is introduced to ensure the rigidity of the particles and the appropriate non-slip boundary condition at the fluid/particle interface. The mathematical expressions for ϕ and $\phi\mathbf{f}_{\mathrm{p}}$ are detailed in previous papers.[15,16] The external force $\mathbf{f}_{\mathrm{shear}}$ is introduced to maintain a linear shear,[19] expressed by

$$v_x=\begin{cases}-\dot{\gamma}y & (0<y<L_y/4),\\ -\dot{\gamma}\left(-y+\dfrac{L_y}{2}\right) & (L_y/4<y<3L_y/4),\\ -\dot{\gamma}\left(y-L_y\right) & (3L_y/4<y<L_y),\end{cases} \tag{3.2}$$

where $\dot{\gamma}$ is the shear rate and L_y is the system size in the y-direction.

In this chapter, the chain is represented as either a rigid rod or a flexible chain. I use a bead-spring model consisting of N beads in a single chain. The bead size is sufficient to fit several mesh units. Therefore, it is necessary to consider the torque exerted on the bead. The motion of the ith bead is governed by the following Newton's and Euler's equations of motion with stochastic forces:

$$M_i\frac{d}{dt}\mathbf{V}_i=\mathbf{F}_i^{\mathrm{H}}+\mathbf{F}_i^{\mathrm{P}}+\mathbf{F}_i^{C}+\mathbf{G}_i^{V},\quad \frac{d}{dt}\mathbf{R}_i=\mathbf{V}_i, \tag{3.3}$$

$$\mathbf{I}_i\cdot\frac{d}{dt}\boldsymbol{\Omega}_i=\mathbf{N}_i^{\mathrm{H}}+\mathbf{G}_i^{\Omega}, \tag{3.4}$$

where $\mathbf{R}_i$, $\mathbf{V}_i$ and $\boldsymbol{\Omega}_i$ are the position, translational velocity, and rotational velocity of the beads, respectively. M_i and $\mathbf{I}_i$ are the mass and moment of inertia, and $\mathbf{F}_i^{\mathrm{H}}$ and $\mathbf{N}_i^{\mathrm{H}}$ are the hydrodynamic force and torque exerted by the solvent on the beads, respectively.[15,16] $\mathbf{G}_i^{\mathrm{V}}$ and $\mathbf{G}_i^{\Omega}$ are the random force and torque, respectively, due to thermal fluctuations. The temperature of the system is defined such that the long-time diffusive motion of dispersed particles reproduces correct behavior.[17,18]

$\mathbf{F}_i^{\mathrm{P}}$ represents the potential force due to direct inter-bead interactions, such as Coulombic and Lennard-Jones potentials. I use a bead-spring model as a model of a polymeric chain with a

truncated Lennard-Jones potential and a finitely extensible nonlinear elastic (FENE) potential. The truncated Lennard-Jones interaction is expressed in terms of U_{LJ}:

$$U_{\mathrm{LJ}}(r_{ij}) = \begin{cases} 4\epsilon \left\{ \left(\dfrac{\sigma}{r_{ij}}\right)^{12} - \left(\dfrac{\sigma}{r_{ij}}\right)^{6} \right\} + \epsilon & (r_{ij} < 2^{\frac{1}{6}}\sigma), \\ 0 & (r_{ij} > 2^{\frac{1}{6}}\sigma), \end{cases} \tag{3.5}$$

where $r_{ij} = |\mathbf{R}_i - \mathbf{R}_j|$. The parameter ϵ characterizes the strength of the interactions, and σ represents the diameter of the beads. Consecutive beads on a chain are connected by a FENE potential of the form

$$U_{\mathrm{FENE}}(r) = -\frac{1}{2} k_{\mathrm{c}} R_0^2 \ln \left\{ 1 - \left(\frac{r}{R_0}\right)^2 \right\}, \tag{3.6}$$

where $r = |\mathbf{R}_{i+1} - \mathbf{R}_i|$, $k_c = 30\epsilon/\sigma^2$, and $R_0 = 1.5\sigma$. $\mathbf{F}_i^{\mathrm{C}}$ is the constraint force acting on the ith bead due to the bond-angle constraints that cause the chain to form a straight line, and it is used only for the rigid rod case. This is given by

$$\mathbf{F}_i^{\mathrm{C}} = \frac{\partial}{\partial \mathbf{R}_i} \Big(\sum_{\alpha=3}^{N} \mu_\alpha \cdot \mathbf{\Psi}_\alpha \Big), \tag{3.7}$$

$$\mathbf{\Psi}_\alpha = (\alpha - 2)\mathbf{R}_1 - (\alpha - 1)\mathbf{R}_2 + \mathbf{R}_\alpha, \quad (\alpha = 3, \cdots, N), \tag{3.8}$$

where $\mathbf{\Psi}_\alpha = 0$ is the constraint condition to be satisfied. μ_α is a Lagrange multiplier associated with the intramolecular forces of the constraints chosen such that the constraint condition $\mathbf{\Psi}_\alpha = 0$ is satisfied at a time $t + h$, where h is the time increment of a single simulation step.

3.2.B Simulation

Numerical simulations have been performed in three dimensions with periodic boundary conditions. The lattice spacing Δ is taken to be the unit of length. The unit of time is given by $\rho_{\mathrm{f}}\Delta^2/\eta$, where $\eta = 1$ and $\rho_{\mathrm{f}} = 1$. The system size is $L_x \times L_y \times L_z = 32 \times 16 \times 64$. The other parameters include: $\sigma = 4$, $\xi = 2$, $\epsilon = 1$, $\eta = 1$, $M_i = 4\pi a^3/3$, $N = 5$ and $h = 0.067$.

In this dissertation, the Navier-Stokes equation is discretized with a de-aliased Fourier spectral scheme in space and with a second-order Runge-Kutta scheme in time. To follow bead motions,

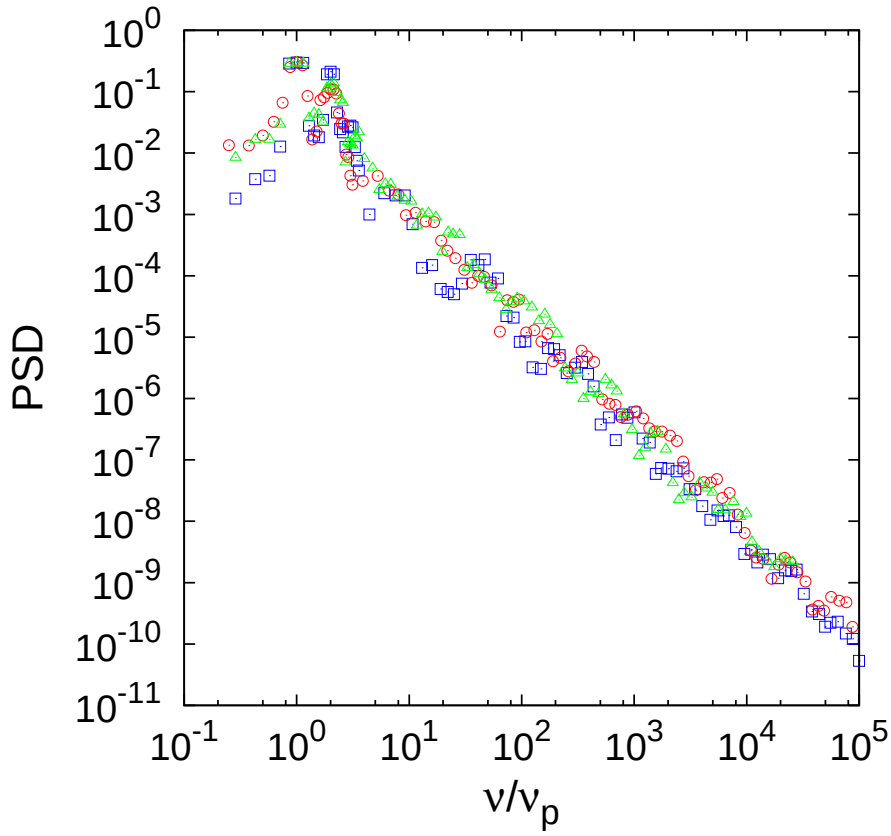

Figure 3.1: The behavior of PSD as a function of ν/ν_p for rigid rods at $k_{\rm B}T/\epsilon = 0.0005$ and $\dot{\gamma} = 0.001$ (□), $k_{\rm B}T/\epsilon = 0.006$ and $\dot{\gamma} = 0.002$ (◯), and $k_{\rm B}T/\epsilon = 0.01$ and $\dot{\gamma} = 0.008$ (△).

the position, velocity and angular velocity of the beads are integrated with the Adams-Bashforth scheme.

At $t = 0$, the chain aligns along the x-axis, which is the shear direction. The run-time of my simulations is about $3520/\dot{\gamma}$. The range of $k_{\rm B}T/\epsilon$ is $5.0 \times 10^{-4} < k_{\rm B}T/\epsilon < 1.0$, and that of $\dot{\gamma}$ is $1.0 \times 10^{-3} < \dot{\gamma} < 4.0 \times 10^{-2}$.

From the symmetry of the system, to analyze the tumbling motion of a chain, we only have to consider the projected tumbling motion on the x-y plane. I introduce the chain orientation angle φ, which is the angle between the x-axis and the projected end-to-end vector on the x-y plane.

Evidence of periodic tumbling motion should appear in the PSD per unit time.[2,3] Therefore, to investigate the spectral properties of the orientation, we calculate the PSD using a fast Fourier transform. The PSD is expressed as

$$PSD(\omega) = |\int \varphi(t) \exp(i\omega t) dt|. \tag{3.9}$$

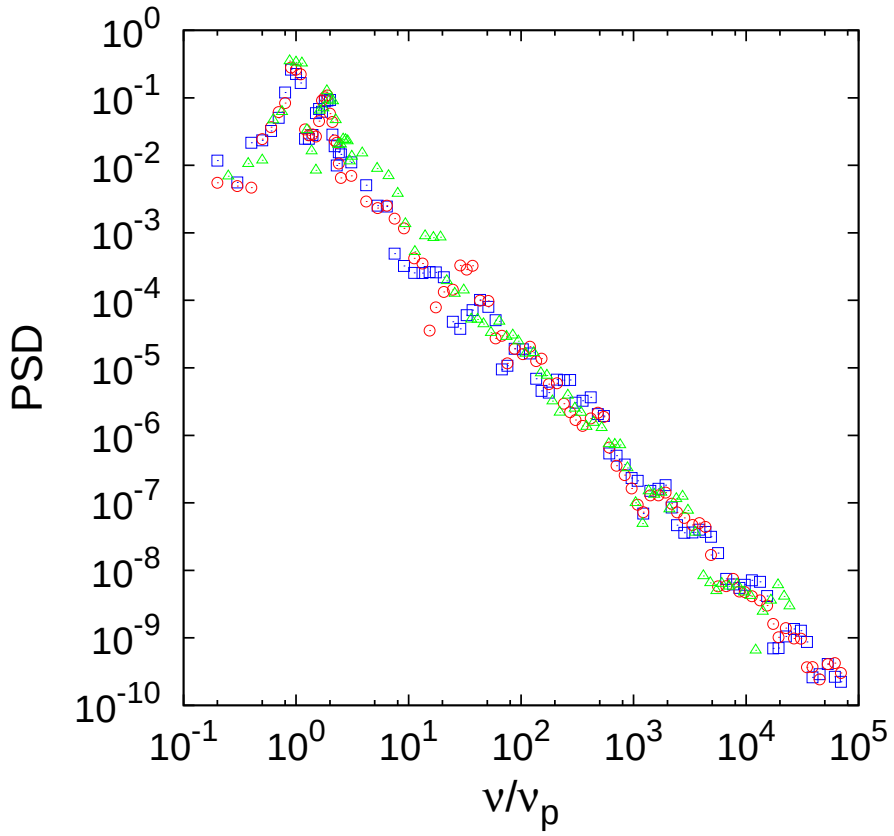

Figure 3.2: The behavior of PSD as a function of ν/ν_p for flexible chains at $k_{\mathrm{B}}T/\epsilon = 0.0005$ and $\dot{\gamma} = 0.001$ (□), $k_{\mathrm{B}}T/\epsilon = 0.006$ and $\dot{\gamma} = 0.002$ (◯), and $k_{\mathrm{B}}T/\epsilon = 0.01$ and $\dot{\gamma} = 0.008$ (△).

3.3 Results

In Figs. 3.1 and 3.2, the PSDs of the chain orientation angle φ show a peak at a specific frequency ν_p, as shown in previous studies.[2,3] Furthermore, the PSD data obtained at different conditions of shear rate and temperature tend to lie on a single master curve if a normalized frequency ν/ν_p is used. This is true for both rigid rods and flexible chains. This result implies that the tumbling motion of chains is fully characterized by ν_p.

In Fig. 3.3, we find that ν_p follows the law $\nu_p \propto \dot{\gamma}$ for $\dot{\gamma} < 0.02$ at $k_{\mathrm{B}}T/\epsilon = 5.0 \times 10^{-4}$, for both the rigid rod and the flexible chain cases. Meanwhile, Fig. 3.4 shows $\nu_p \propto \dot{\gamma}^{0.68}$ for $\dot{\gamma} < 0.02$ at $k_{\mathrm{B}}T/\epsilon = 1.0$ for both.

Figure 3.3 also shows that, for $\dot{\gamma} > 0.02$, ν_p is lower than the frequency expected from the law $\nu_p \propto \dot{\gamma}$. P. Bagchi and S. Balachandar have reported that, at a finite Reynolds number approximately equal to 1, the sphere rotation frequency in a linear shear flow decreases at a much slower rate than $\dot{\gamma}/2$.[20] The Reynolds number, Re, is given by $Re = \rho_f \dot{\gamma} \sigma^2 N/\eta$. In this chapter,

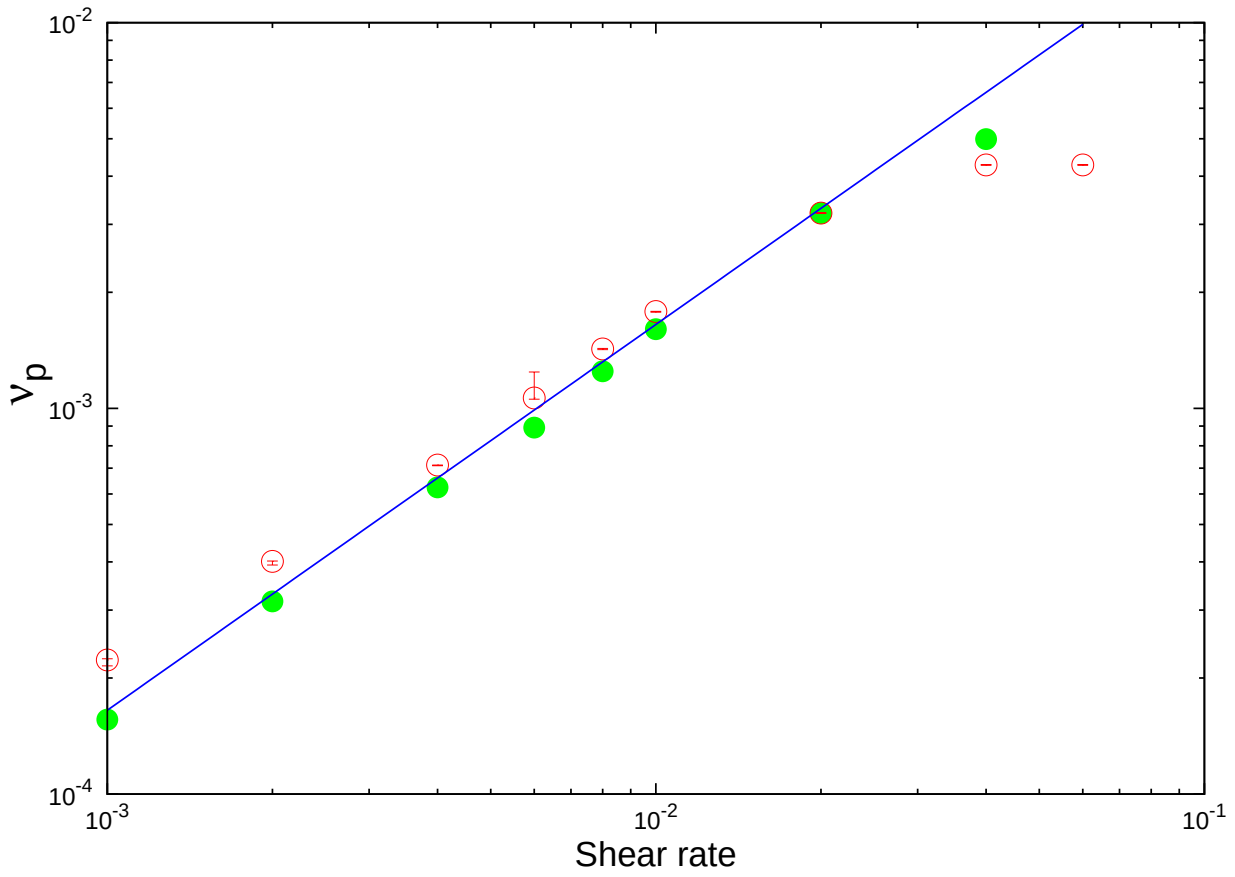

Figure 3.3: The behavior of ν_p as a function of $\dot{\gamma}$ at $k_{\mathrm{B}}T/\epsilon = 0.0005$. Rigid rod (closed circle), flexible chain (open circle). The solid line corresponds to the law $\nu_p \propto \dot{\gamma}$. Error bars are derived from the half band width of PSD.

Re is equal to 1.6 at $\dot{\gamma} = 0.02$. I only consider ν_p in the region of $\dot{\gamma} \leq 0.02$, so the effects of finite Reynolds numbers do not influence the results.

I arrange data sets using the Peclet number to consider the effect of competition between shear and fluctuation. The Peclet number is the dimensionless number that relates the rate of shear flow to the rate of thermal fluctuation. In my dissertation, the Peclet number, Pe, and dimensionless frequency, F, are expressed as

$$Pe = \frac{6\pi\eta\sigma^3\dot{\gamma}}{k_{\mathrm{B}}T}, \tag{3.10}$$

$$F = \frac{6\pi\eta\sigma^3\nu_p}{k_{\mathrm{B}}T}. \tag{3.11}$$

I plotted the behavior of F as a function of Pe for the rigid rod and flexible chain cases in Figs. 3.5 and 3.6. F was found to depend only on Pe because the data sets have the same value

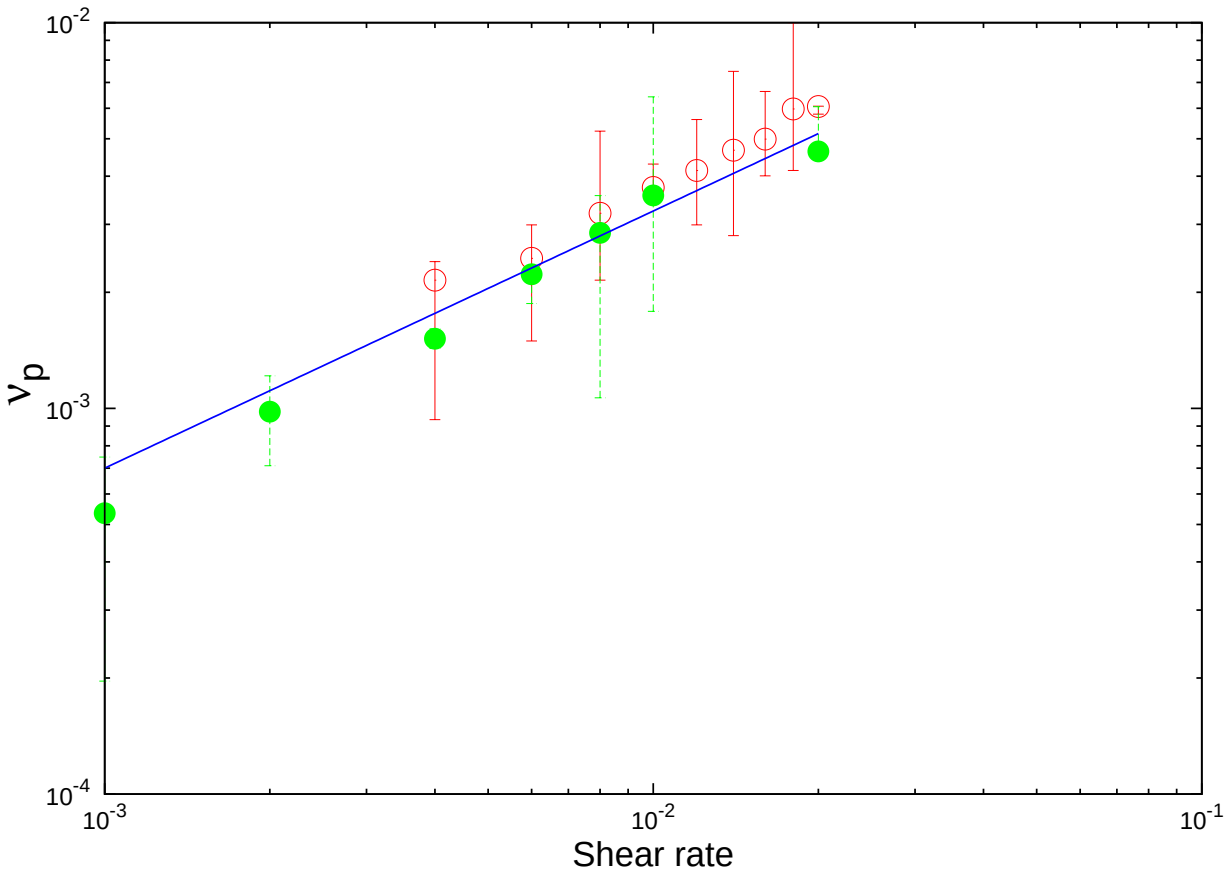

Figure 3.4: The behavior of ν_p as a function of $\dot{\gamma}$ at $k_{\rm B}T/\epsilon = 1.00$. Rigid rod (closed circle), flexible chain (open circle). The solid line corresponds to the law $\nu_p \propto \dot{\gamma}^{2/3}$. Error bars are derived from the half band width of PSD.

of F with the same value of Pe, even when the shear rates and temperatures are different. In the rigid rod case, $F \propto Pe^{0.65}$ for $Pe < 106$ and $F \propto Pe$ for $Pe > 106$. In the flexible chain case, $F \propto Pe^{0.68}$ for $Pe < 156$ and $F \propto Pe$ for $Pe > 156$. The behaviors of F for the rigid rod case and the flexible chain case are roughly equal, although the values of the Peclet numbers are different at the boundary where the exponent of Pe changes.

I define the critical value at which the exponent of Pe drastically changes from almost 2/3 to 1 as the *critical Peclet number*, $Pe_{\rm c}$. $F \propto Pe^{2/3}$ for $Pe < Pe_{\rm c}$; otherwise, $F \propto Pe$. When fluctuations dominate the system, the exponent is nearly equal to 2/3. On the other hand, when shear flow dominates, the exponent is exactly equal to 1.

In order to understand the behavior of F in the limit of $Pe \to \infty$, I examine the behavior of ν_p in the limit of $k_{\rm B}T \to 0$ and Figure 3.7 shows the law $\nu_p \propto \dot{\gamma}$. As shown in Figs. 3.5 and 3.6, the behavior of F in the region of $Pe_{\rm c} < Pe$ is roughly equal to the behavior of ν_p in the limit of $k_{\rm B}T \to 0$. Therefore, I believe that the proportional relation $F \propto Pe$ can be true across the entire

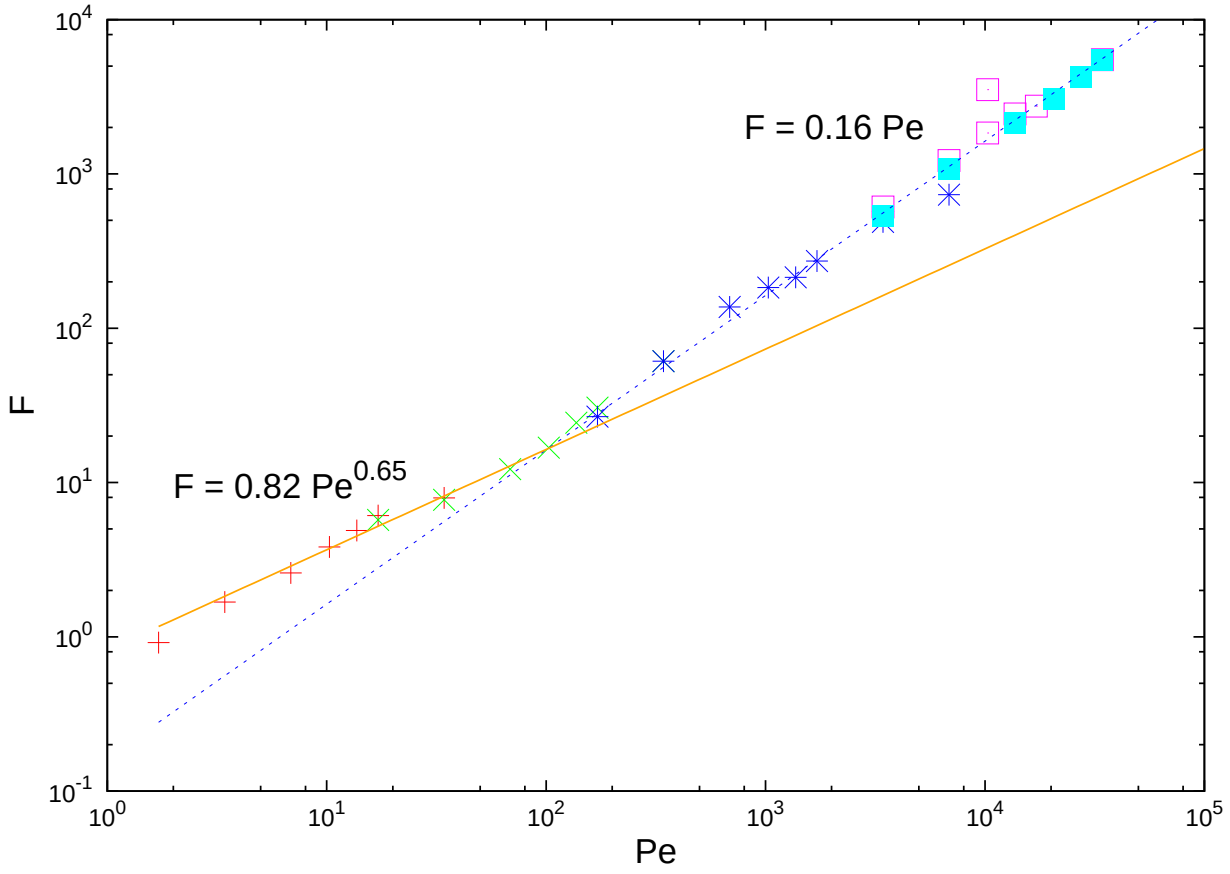

Figure 3.5: The behavior of F as a function of Pe for a rigid rod. The solid and dotted lines were calculated from a least-squares fit of the data points. The solid line corresponds to $Pe^{0.65}$. The dotted line corresponds to Pe.

region of $Pe_c < Pe$.

3.4 Discussion

3.4.A Comparison with other results

In this chapter, I calculate the tumbling motion of a single chain for $0.0005 < k_BT/\epsilon < 1.00$ and $0.001 < \dot{\gamma} < 0.04$. As reported in Jeffrey's paper,[12] which treated non-Brownian particles, ν_p follows the law $\nu_p \propto \dot{\gamma}$ at $k_BT/\epsilon = 5.0 \times 10^{-4}$, as shown in Fig. 3.3. In previous papers[5–8] that treated Brownian particles, ν_p follows the law $\nu_p \propto \dot{\gamma}^{2/3}$ at $k_BT/\epsilon = 1.0$, as shown in Fig. 3.4.

The dimensionless frequency, F, depends only on Pe. This Pe dependence on F can be described by a power law, $F \propto Pe^{\alpha}$. The exponent α drastically changes from 2/3 to 1 at Pe_c; α equals 2/3 for $Pe < Pe_c$, while α equals 1 for $Pe_c < Pe$. In the case of a rigid rod with $N = 5$, $Pe_c \approx 106$, and $Pe_c \approx 156$ in the flexible chain case. When fluctuations dominate the system, F follows the law of $F \propto Pe^{2/3}$. On the other hand, when shear flow dominates, F follows the law of $F \propto Pe$.

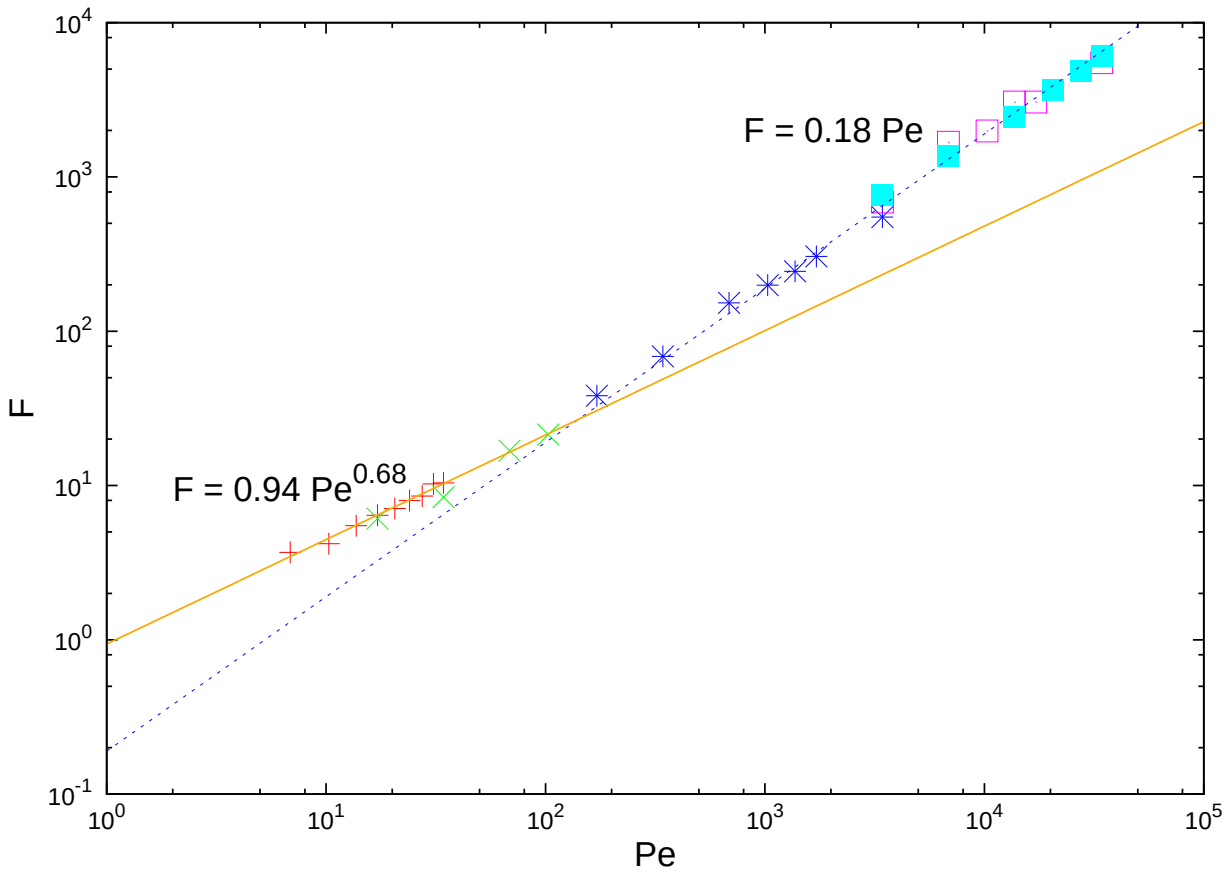

Figure 3.6: The behavior of F as a function of Pe for a flexible chain. The solid and dotted lines were calculated from a least-squares fit of the data points. The solid line corresponds to $Pe^{0.68}$. The dotted line corresponds to Pe.

Gerashchenko and Steinberg[4] claim that there are two dynamical regimes of polymer motion at $Wi \gg 1$, depending on the polymer extension R. When $R \ll R_{max}$, where R_{max} is the maximum polymer extension, the tumbling frequency ν is constant and independent of Wi. On the other hand, when $R \sim R_{max}$, ν is proportional to $Wi^{2/3}$. In Fig. 3.4, we did not observe ν_p to be independent of $\dot{\gamma}$. I consider the chain length to be too short in my work. The chain cannot keep the coil state along the shear direction for long times. The chain is fully stretched at short notice and is always rotated, although Pe is small.

Previously, Szymczak and Cieplak[21] discussed the conformational dynamics of a single long protein in shear flow and found two characteristic tumbling frequencies, ν_1 and ν_2. They showed that the higher frequency ν_1 follows the law of $\nu_1 \propto \dot{\gamma}$; however, the lower frequency ν_2 follows the law of $\nu_2 \propto \dot{\gamma}^{2/3}$. When the protein is tightly packed, it essentially shows a spherical rotation in shear flow. As a result, ν_1 is proportional to $\dot{\gamma}$. The lower frequency, ν_2, corresponds to the

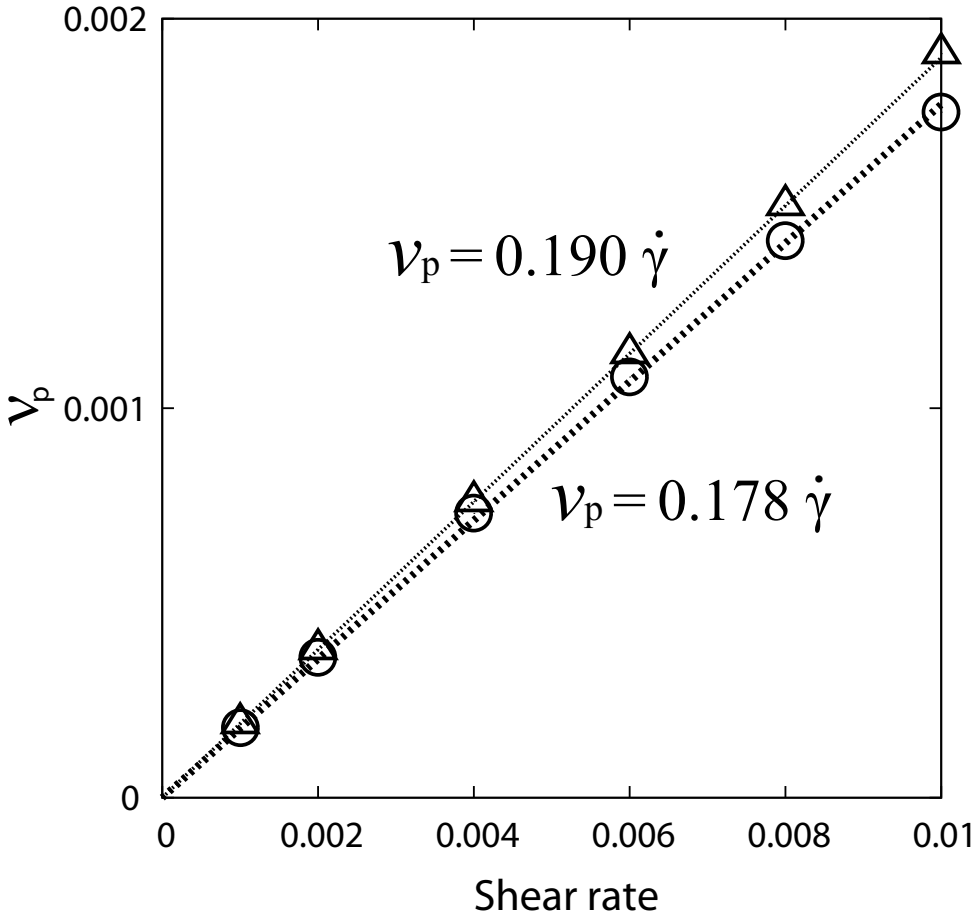

Figure 3.7: The behavior of ν_p as a function of $\dot{\gamma}$ at $k_{\mathrm{B}}T/\epsilon = 0$. Rigid rod (circle), flexible chain (triangle). The data sets for the rigid rods correspond to the law $\nu_p = 0.178\dot{\gamma}$. The data sets for the flexible chains correspond to the law $\nu_p = 0.190\dot{\gamma}$.

stretching-collapse cycle; hence, ν_2 is proportional to $\dot{\gamma}^{2/3}$. Although my results are similar to theirs, the phenomena in my system are essentially different from those in their works because rigid rods cannot fold.

Davoudi and Schumacher[22] analyzed the stretching of polymers in a turbulent flow. It is known that the polymers undergo a coil-stretch transition at $Wi \approx 1/2$ in this system. For $Wi < 1/2$, polymers are in the coiled state, and their size distribution is stationary. In contrast, for $Wi > 1/2$, the polymers are in the stretched state. Their stretching carries on until their lengths reach the finite extensibility limit or until turbulence stops the growth of the polymers. They found the maximum Lyapunov exponent to be $\lambda \sim \dot{\gamma}^{3/2}$. However, Chertkov et al. reported $\lambda \sim \dot{\gamma}^{2/3}$ in their work, where λ^{-1} is expressed as the mean stretching time scale. Davoudi and Schumacher claimed also that their study could not be compared with the analytic results of Chertkov et al. They defined the shear time scale as $T_s = \dot{\gamma}^{-1}$ and the fluctuation time scale as $T_f = D^{-1}$, where

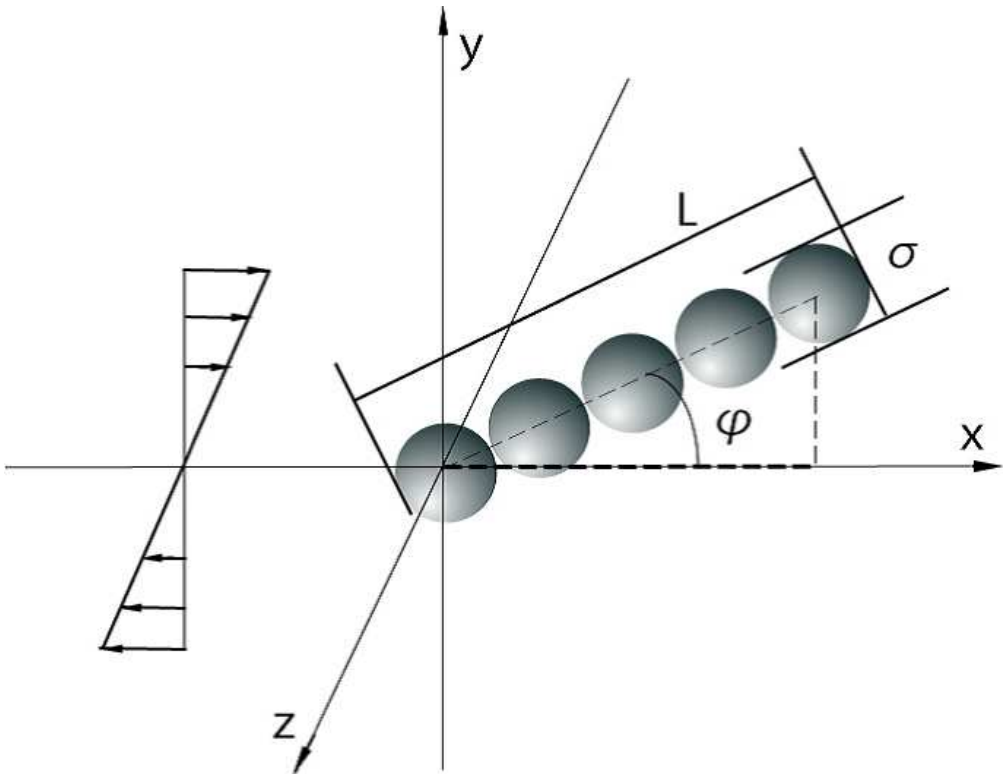

Figure 3.8: The geometry of the present simulations.

D is the strength of Gaussian fluctuation. Chertkov analyzed the polymer dynamics in the region of $T_s \ll T_f$. Davoudi analyzed the polymer dynamics in the region of $\tau_\eta < T_s$, where τ_η is the Kolmogorov time. Notably, Davoudi's work studies a different regime of polymer stretching than the analytic model of Chertkov's work. Chertkov et al. studied in the shear-dominated regime, whereas Davoudi and Schumacher studied in the turbulence-dominated regime.

My work analyzed polymer dynamics in the region of $T_s \ll T_f$. I do not consider the effect of turbulent flow. I only considered the region with particle Reynolds number $Re < 1.6$, so the effects of finite Reynolds numbers do not influence the results. In Davoudi's work, by contrast, the region of particle Reynolds number in the stretched state is estimated to be $Re^{'} > 15$, where $Re^{'} = vL/\nu$, ν is kinetic viscosity, v is the root-mean-square of the turbulent velocity fluctuation, and L is the mean length of polymer. Therefore, my study cannot be compared with Davoudi's work.

3.4.B Theoretical analysis

The geometry of the chain is depicted in Fig. 3.8. In Jeffrey's work,[12] the angle φ of non-Brownian rigid rods with finite aspect ratios is governed by the equation

$$\frac{d}{dt}\varphi = -\dot{\gamma}\frac{r^2-1}{r^2+1}\sin^2\varphi - \dot{\gamma}\frac{1}{r^2+1}, \tag{3.12}$$

where the aspect ratio is $r = L/\sigma$ and L is the length of the chain.

In my work, I consider the equation that governs the angle φ of a Brownian rigid rod with a finite aspect ratio. To consider the diffusion of thermal fluctuation, I introduce white noise $\zeta(t)$ into Eq. (3.12). I can then write down the following equation for a Brownian rigid rod:

$$\frac{d}{dt}\varphi = -\dot{\gamma}\frac{r^2-1}{r^2+1}\sin^2\varphi - \dot{\gamma}\frac{1}{r^2+1} + 2\sqrt{\frac{D_r}{\cos^2\theta}}\zeta, \tag{3.13}$$

$$< \zeta(t)\zeta(t') >= \delta(t-t'), \tag{3.14}$$

where D_r is the rotational diffusion constant. On the basis of the shell model,[23,24] the rotational diffusion constant D_r for a rigid rod is calculated as

$$D_r = \frac{3(\ln r + d(r))k_{\mathrm{B}}T}{\pi\eta L^3}, \tag{3.15}$$

$$d(r) = -0.662 + \frac{0.917}{r} - \frac{0.05}{r^2}. \tag{3.16}$$

In the shell model mentioned above, the contour of the macromolecules of arbitrary shape is represented by a shell composed of many identical small beads. The shell model can be adequately modeled by decreasing the size of the beads.

In the case of $D_r \ll \dot{\gamma}$, the dynamics of the angle φ become decoupled from the angle θ between the end-to-end vector and the $x-y$ plane because the angle θ is approximately zero. We can then write down the following equation:

$$\frac{d}{dt}\varphi = -\dot{\gamma}\frac{r^2-1}{r^2+1}\sin^2\varphi - \dot{\gamma}\frac{1}{r^2+1} + 2\sqrt{D_r}\zeta. \tag{3.17}$$

For short times, the mean square displacement of $\varphi(t)$ in time t is written as

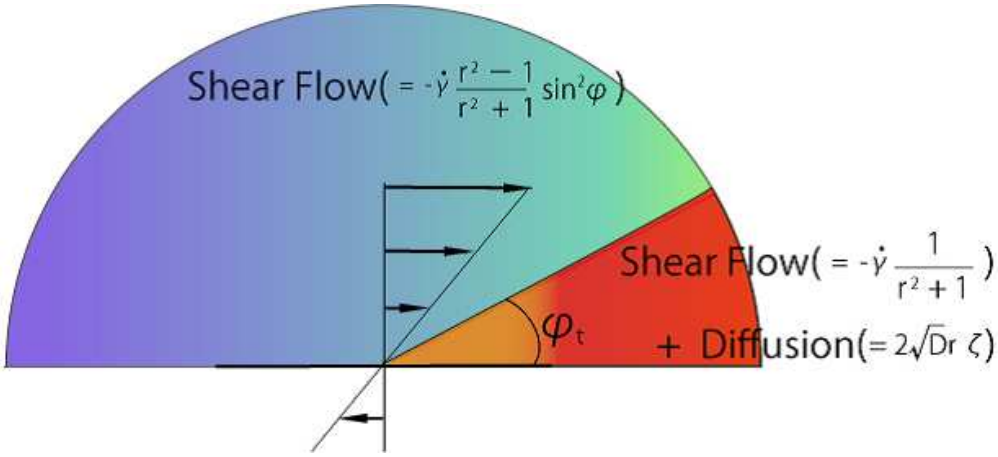

Figure 3.9: Schematic diagram of two areas and the angle φ_t. The angle φ_t is the boundary angle of the area dominated by the first term and the area dominated by the second and third terms on the right-hand side of Eq. (3.17).

$$< |\varphi(t) - \varphi(0)|^2 >= 4D_r t \quad (for \;\; D_r t \ll 1). \tag{3.18}$$

In order to analyze the tumbling motion of a single chain, I only have to consider the dynamics in the stochastic area, where the effect of thermal fluctuation is not negligible. In the case of $D_r \ll \dot{\gamma}$, the time required to pass through the stochastic area is sufficiently larger than the time required to pass through the other area. The tumbling motion can only be understood by considering the stochastic area. The stochastic area is dominated by the second and third terms on the right-hand side of Eq. (3.17). The remaining area is dominated by the first term on the right-hand side of Eq. (3.17). Figure 3.9 shows the two areas and the angle φ_t, which is the boundary angle between the two areas. I call the second and third terms on the right-hand side of Eq. (3.17) the shear and the fluctuation terms, respectively.

1 Infinite aspect ratio case

First, I consider Eq. (3.17) in the limit where $r \to \infty$. This limit is consistent with treating a chain as an end-to-end vector. I can rewrite Eq. (3.17) as $\dot{\varphi} = -\dot{\gamma}\sin^2\varphi + 2\sqrt{D_r}\zeta$, in which the shear term does not exist. This equation is identical to the equation used in previous works.[5–8]

Previous works[4–6] have reported $\varphi_t \sim (D_r/\dot{\gamma})^{1/3}$. In the region of $\varphi_t < \varphi < \pi$, the shear flow rapidly rotates the orientation of the chain from π to φ_t in a time $t_l \approx \dot{\gamma}^{-1}$. In the region of $0 < \varphi < \varphi_t$, the chain orientation almost aligns along the shear direction. Because the effect of

shear becomes sufficiently small in this region, the effect of thermal fluctuations only contributes to rotate the chain orientation from φ_t to 0 in time $t_r = \varphi_t^2/4D_r \propto \dot{\gamma}^{-2/3}$, as calculated with Eq. (3.18). In the case of $t_r > t_l$, t_r dominates the chain tumbling time. I can consider $\nu_p \propto t_r^{-1}$. Therefore, I conclude from Eqs. (3.10) and (3.11) that $F \propto Pe^{2/3}$.

2 Finite aspect ratio case

Next, I consider Eq. (3.17) with a finite aspect ratio, r. I can expect F to be proportional to $Pe^{2/3}$ when the fluctuation term dominates in the region $0 < \varphi < \varphi_t$, as this case agrees with the limit of $r \to \infty$. Additionally, I can expect F to be proportional to Pe when the shear term dominates in the region $0 < \varphi < \varphi_t$ because this case corresponds to the non-Brownian rigid rod. Pe_c is defined as the Peclet number at which the dominating term in the stochastic area changes from the fluctuation term to the shear term with increasing shear rate.

From Eq. (3.17), I can write down the corresponding Fokker-Planck equation as

$$\frac{\partial}{\partial t}P(t,\varphi) + \frac{\partial}{\partial \varphi}J_\varphi = 0, \tag{3.19}$$

$$J_\varphi = -\left\{\dot{\gamma}\frac{r^2-1}{r^2+1}\sin^2\varphi + \dot{\gamma}\frac{1}{r^2+1} + 2D_r\frac{\partial}{\partial\varphi}\right\}P(t,\varphi), \tag{3.20}$$

where $P(t,\varphi)$ is the PDF of the angle φ and J_φ is the probability flow. Each term in the braces of Eq. (3.20) corresponds to a respective term on the right-hand side of Eq. (3.17).

Next, I focus on the stationary PDF $P_{\rm st}(\varphi) \equiv P(t=0,\varphi)$. Because $\partial P_{\rm st}(\varphi)/\partial t = 0$, namely, $\partial J_\varphi/\partial\varphi = 0$ from Eq. (3.19), J_φ is φ-independent and constant: $J_\varphi = -\dot{\gamma}[(r^2-1)\sin^2\varphi_{\rm p}P_{\rm st}(\varphi_{\rm p}) + P_{\rm st}(\varphi_{\rm p})]/(r^2+1)$, where $\varphi_{\rm p}$ is the angle at which $P_{\rm st}(\varphi)$ has a peak. I surmise that the angle φ_t satisfies the equation given by

$$\begin{aligned}\frac{J_\varphi}{2} &= -\dot{\gamma}\frac{(r^2-1)\sin^2\varphi P_{\rm st}(\varphi)}{r^2+1} \\ &= -\dot{\gamma}\frac{P_{\rm st}(\varphi)}{r^2+1} - 2D_r\frac{\partial P_{\rm st}(\varphi)}{\partial\varphi}.\end{aligned} \tag{3.21}$$

By substituting the J_φ expressed by $\varphi_{\rm p}$ into Eq. (3.21), the relation of φ_t to $\varphi_{\rm p}$ is given as

$$-\dot{\gamma}\frac{(r^2-1)\sin^2\varphi_{\rm p}P_{\rm st}(\varphi_{\rm p})+P_{\rm st}(\varphi_{\rm p})}{r^2+1}$$
$$=-2\dot{\gamma}\frac{(r^2-1)\sin^2\varphi_t P_{\rm st}(\varphi_t)}{r^2+1}. \tag{3.22}$$

The angle φ_t is calculated by solving Eq. (3.22). $P_{\rm st}(\varphi_t)$ is expanded in powers $\triangle\varphi = \varphi_t - \varphi_{\rm p}$. When I neglect the second order of $\triangle\varphi$ and higher, I can relate φ_t to $\varphi_{\rm p}$ as

$$\varphi_t = \sqrt{\frac{1}{2}\left(\varphi_{\rm p}^2 + \frac{1}{r^2-1}\right)}. \tag{3.23}$$

It should be noted that $\varphi_t, \varphi_{\rm p} \ll 1$. I can estimate φ_t with the angle $\varphi_{\rm p}$.

Next, I attempt to calculate the analytical form of $\varphi_{\rm p}$. In the case of $D_r/\dot{\gamma} \ll 1$, the formal solution for $P_{\rm st}(\varphi)$ is given by

$$P_{\rm st}(\varphi) = C_1 \int_0^\pi d\psi \exp\left(-\frac{\dot{\gamma}}{4D_r} f(\psi,\varphi)\right), \tag{3.24}$$
$$f(\psi,\varphi) = \psi - (1-\frac{2}{r^2+1})\sin\psi\cos(\psi-2\varphi), \tag{3.25}$$

where C_1 is determined from the normalization condition, $\int_0^\pi P_{\rm st}(\varphi)d\varphi = 1$. In the limit of $r \to \infty$, it is known that $\varphi_{\rm p} = (D_{\rm r}/\dot{\gamma})^{1/3}$.[6] When r is finite, $\varphi_{\rm p}$ is different from $(D_{\rm r}/\dot{\gamma})^{1/3}$ because the shear term influences $P_{\rm st}(\varphi)$.

To estimate the effect of the shear term, I introduce the times $t_2^{'}$ and $t_3^{'}$, where $t_2^{'}$ and $t_3^{'}$ represent the times required to pass through the region $0 < \varphi < (D_{\rm r}/\dot{\gamma})^{1/3}$, depending only on the shear term and the fluctuation term, respectively. $t_2^{'}$ is estimated by dividing $(D_{\rm r}/\dot{\gamma})^{1/3}$ by the shear term as

$$t_2^{'} = \frac{(r^2+1)D_{\rm r}^{\frac{1}{3}}}{\dot{\gamma}^{\frac{4}{3}}}, \tag{3.26}$$

and $t_3^{'}$ is estimated by Eq. (3.18) as

$$t_3^{'} = \frac{1}{4D_{\rm r}^{\frac{1}{3}}\dot{\gamma}^{\frac{2}{3}}}. \tag{3.27}$$

Because the Brownian chain is rotated by both the shear term and the fluctuation terms, I expect that $\varphi_{\rm p}$ is given by

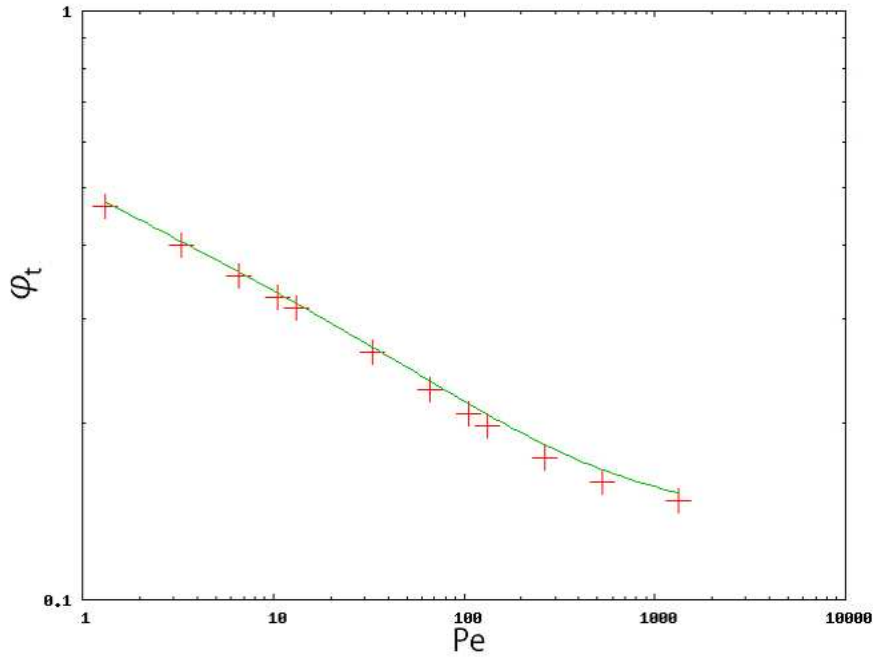

Figure 3.10: The behavior of φ_t as a function of Pe. $\varphi_{t'}$ is φ_t calculated with $\varphi_{\rm p}$, obtained from numerical integration (+). The solid line corresponds to the behavior of $\varphi_{t''}$, where $\varphi_{t''}$ is φ_t, obtained from $\varphi_{\rm p} = [t_2^{'}/(t_2^{'} + t_3^{'})] \times (D_{\rm r}/\dot{\gamma})^{1/3}$.

$$\varphi_{\rm p} = C^{'}(r, Pe) \left(\frac{D_{\rm r}}{\dot{\gamma}} \right)^{\frac{1}{3}}, \tag{3.28}$$

$$\begin{aligned} C^{'}(r, Pe) &\equiv \frac{t_2^{'}}{t_2^{'}+t_3^{'}} \\ &= \left\{ 1 + \frac{1}{4r^2+1} \left(\frac{r^3}{18(\ln r + d(r))} Pe \right)^{\frac{2}{3}} \right\}^{-1}. \end{aligned} \tag{3.29}$$

For large $\dot{\gamma}/D_r$ where the present theoretical analysis is valid, $C^{'}(r, Pe) \sim t_2^{'}/t_3^{'}$ finally approaches zero. I confirmed, however, that $t_2^{'}/t_3^{'}$ still remains finite (~ 1) around $Pe_c \approx 100$, where $\dot{\gamma}/D_r \approx 1000$.

Figure 3.10 shows the behaviors of $\varphi_{t'}$ and $\varphi_{t''}$ as a function of Pe, where $\varphi_{t'}$ is φ_t calculated with Eq. (3.23) and $\varphi_{\rm p}$, which is obtained from the numerical integration of Eq. (3.24), and $\varphi_{t''}$ is φ_t calculated with Eq. (3.23) and $\varphi_{\rm p}$, which is expressed as Eq. (3.28). In this figure, it is shown that Eq. (3.28) is established because the behavior of $\varphi_{t'}$ agrees well with $\varphi_{t''}$ for $Pe \leq 100$. I can obtain φ_t by substituting Eq. (3.28) into Eq. (3.23). Therefore, φ_t is given by

$$\varphi_t = C(r, Pe) \left(\frac{D_{\rm r}}{\dot{\gamma}} \right)^{\frac{1}{3}}, \tag{3.30}$$

$$C(r, Pe) = \sqrt{\frac{1}{2}\left\{C'^2 + 4\left(\frac{r^2+1}{r^2-1}\right)\frac{1-C'}{C'}\right\}}. \tag{3.31}$$

I consider that F is proportional to $Pe^{2/3}$ when the effect of thermal fluctuation is more significant than the effect of shear flow in the region of $0 < \varphi < \varphi_t$ and that F is proportional to Pe in the opposite case. t_2 is the time required to pass through the region $0 < \varphi < \varphi_t$ by the shear term,

$$t_2 = \frac{(r^2+1)CD_{\mathrm{r}}^{\frac{1}{3}}}{\dot{\gamma}^{\frac{4}{3}}}. \tag{3.32}$$

t_3 is the time required to pass through the region $0 < \varphi < \varphi_t$ by the fluctuation term,

$$t_3 = \frac{C^2}{4D_{\mathrm{r}}^{\frac{1}{3}}\dot{\gamma}^{\frac{2}{3}}}. \tag{3.33}$$

It is thought that Pe_{c} is the Peclet number that satisfies $t_2 = t_3$. If we obtain the value of r, we know the value of Pe_{c} because both t_2 and t_3 are functions of Pe and r. My results show that $Pe_{\mathrm{c}} \approx 115$ at $r = 5$. In the numerical results obtained from my work, $Pe_{\mathrm{c}} = 106$. The analytical result agrees well with my numerical result. Moreover, the numerical condition $D_{\mathrm{r}} \ll \dot{\gamma}$ is satisfied because $D_{\mathrm{r}}/\dot{\gamma} \approx 10^{-3} \ll 1$ at $Pe \approx 100$. Therefore, the considerations in this section are reasonable in the region near Pe_{c}.

The considerations in this section agree well with those of previous experimental results.[2–4,10,14] In experimental works that measured the frequencies of DNA rotation,[2–4,10] the DNA molecules contained roughly 400 persistence lengths. The persistence length is thought to correspond to r. Thus, I conclude that $Pe_{\mathrm{c}} \approx 516$. These experiments were carried out in the region of $Pe \ll Pe_{\mathrm{c}}$, and F is proportional to $Pe^{2/3}$. In experimental work that measured the frequencies of freely rotating rigid dumbbells,[14]the aspect ratio r of the rigid dumbbell corresponds to 2 and $Pe_{\mathrm{c}} \approx 60$. The experiments were carried out in the region of $Pe_{\mathrm{c}} \ll Pe$, and F was proportional to Pe. From these results, the considerations in this section are reasonable.

3.5 Conclusion

In my work, I calculated the tumbling motion of a single chain using an SPM that takes into account thermal fluctuations and hydrodynamic interactions for $0.0005 < k_{\mathrm{B}}T/\epsilon < 1.00$ and $0.001 < \dot{\gamma} < 0.02$. I conclude that the dimensionless frequency, F, depends only on Pe. The dependence of F

can be described by a power law $F \propto Pe^{\alpha}$. The exponent α sharply changes from 2/3 to 1 on Pe_{c}. In the case of a rigid rod with $N = 5$, $Pe_{\mathrm{c}} \approx 106$, and in the case of a flexible chain with $N = 5$, $Pe_{\mathrm{c}} \approx 156$. The behavior of F for both cases is similar, while only the values of Pe_{c} are different from each other.

I have presented F to be proportional to $Pe^{2/3}$ when the third term on the right-hand side of Eq. (3.17) dominates in the region $0 < \varphi < \varphi_t$, and F is proportional to Pe when the second term of Eq. (3.17) dominates in the region $0 < \varphi < \varphi_t$. I have estimated the angle φ_t at which the first term of J_φ, expressed as Eq. (3.20), is comparable to the sum of the second and third terms of J_φ, expressed as Eq. (3.20).

A proposed mechanism for this exponent change is that the effect of thermal fluctuation is more significant than the effect of shear flow only for $0 < \varphi < \varphi_t$, whereas in the other case, the effect of thermal fluctuation is negligible. The former contribution leads to $F \propto Pe^{2/3}$, and the latter contribution leads to $F \propto Pe$.

References

1 K. Kamata, T. Araki, and H. Tanaka, Phys. Rev. Lett. **102**, 108303 (2009).

2 C. M. Schroeder, R. E. Teixeira, E. S. G. Shaqfeh, and S. Chu, Phys. Rev. Lett. **95**, 018301 (2005).

3 R. E. Teixeria, H. P. Babcock, E. S. G. Shaqfeh, and S. Chu, Macromolecules **38**, 581 (2005).

4 S. Gerashchenko and V. Steinberg, Phys. Rev. Lett. **96**, 038304 (2006).

5 A. P. A. Celani and K. Turitsyn, Europhys. Lett. **70**, 464 (2005).

6 A. Puliafito and K. Turitsyn, Physica D **211**, 9 (2005).

7 M. Chertkov, I. Kolokolov, V. Lebedev, and K. Turitsyn, J. Fluid Mech. **531**, 251 (2005).

8 K. S. Turitsyn, J. Experimental and Theoretical Phys. **105**, 655 (2007).

9 R. G. Winkler, Phys. Rev. Lett. **97**, 128301 (2006).

10 D. E. Smith, H. P. Babcock, and S. Chu, Science **283**, 1724 (1999).

11 S. Yamamoto and T. Matsuoka, J. Chem. Phys. **98**, 644 (1993).

12 G. B. Jeffery, Proc. R. Soc. A **102**, 161 (1922).

13 F. P. Breterthon, J. Fluid Mech. **14**, 284 (1962).

14 K. Takamura, J. Colloid Interface Sci. **83**, 516 (1981).

15 Y. Nakayama and R. Yamamoto, Phys. Rev. E **71**, 036707 (2005).

16 Y. Nakayama, K. Kim, and R. Yamamoto, Eur. Phys. J. E **26**, 361 (2008).

17 T. Iwashita, Y. Nakayama, and R. Yamamoto, J. Phys. Soc. Jpn. **77**, 074007 (2008).

18 T. Iwashita and R. Yamamoto, Phys. Rev. E **79**, 031401 (2009).

19 J. Schumacher and B.Eckhardt, Europhys. Lett. **52**, 627 (2000).

20 P. Bagchi and S. Balachandar, Phys. Fluids **14**, 2719 (2002).

21 P. Szymczak and M. Cieplak, J. Chem. Phys. **127**, 155106 (2007).

22 J. Davoudi and J. Shumacher, Phys. Fluids **18**, 025103 (2006).

23 M. M. Tirado and J. G. de la Torre, J. Chem. Phys. **73**, 1986 (1980).

24 M. M. Tirado, J. Chem. Phys. **81**, 2047 (1984).

Chapter 4

Reentrant transition in the shear viscosity of dilute rigid rod dispersions

4.1 Introduction

The viscous properties of dilute dispersions of rigid rods change drastically as the rate of applied shear flows $\dot{\gamma}$ increases. Although many previous studies have investigated this phenomenon, the mechanism of this viscosity change is not yet completely clear. The aim of this chapter is to understand the detailed mechanism of the viscosity change by performing direct numerical simulations (DNS) for a dilute dispersion of rigid rods that are subject to thermal fluctuations in a Newtonian host fluid.

The relationship between the measurable bulk rheological properties and the microscale description of dispersions of rod-like particles has been previously investigated in the literature.[1–9] Giesekus obtained the expression for the bulk stress tensor of diluted spheroidal dispersions under shear flow by taking into account the effects of the rotational Brownian motion of the spheroids due to thermal fluctuations.[3] Leal and Hinch reported that the viscosity behavior is characterized by the aspect ratio r of the rod and dimensionless shear rate $\dot{\gamma}/D_{\mathrm{r}}$, where D_{r} is the rotational diffusion constant.[5–8]

In the case of weak shear flow, $\dot{\gamma}/D_{\mathrm{r}} \ll 1$, the dilute rigid rod dispersions exhibit the 1st Newtonian behavior, in which the viscosity η of the dispersion is constant and equal to the 1st Newtonian (zero-shear limiting) value η_0. For an intermediate regime, $1 \ll \dot{\gamma}/D_{\mathrm{r}} \ll r^3 + r^{-3}$, the dispersions exhibit shear-thinning behavior, in which $\eta \propto (\dot{\gamma}/D_{\mathrm{r}})^{-1/3}$. In the case of strong shear flow, $r^3 + r^{-3} \ll \dot{\gamma}/D_{\mathrm{r}}$, the dispersions reenter the 2nd Newtonian regime, in which η becomes constant again and is equal to the 2nd Newtonian (high-shear limiting) value η_∞. Similar results have also been obtained in numerical[10,11] and experimental[12,13] studies. In this chapter, the phrase *viscosity transition* is used to express the changes in viscosity from the 1st Newtonian to the shear-thinning behavior and also from the shear-thinning to the 2nd Newtonian behavior. Similar results have been observed for dilute dispersions of flexible chains, both experimentally[14] and theoretically.[15]

Hinch and Leal[5,6] proposed a theoretical model for the viscosity transitions. They considered that the viscosity η of the dispersion is determined by the ensemble average of the temporal viscosity $\hat{\eta}(\theta, \varphi)$ using the probability distribution function (PDF) $P_{\dot{\gamma}}(\theta, \varphi)$ of the two orientational angles θ and φ of the rod, *i.e.*,

$$\eta(\dot{\gamma}) = \int \hat{\eta}(\theta, \varphi) P_{\dot{\gamma}}(\theta, \varphi) d\theta d\varphi. \tag{4.1}$$

Here the form of $P_{\dot{\gamma}}(\theta, \varphi)$ is shear rate dependent, and the shear rate dependence of the dispersion viscosity $\eta(\dot{\gamma})$ is introduced mainly through this function.

The rigid rod undergoes a random rotational Brownian motion at low shear rates in the 1st Newtonian regime, where the effect of thermal fluctuations is dominant over the effect of shear flow. Therefore,

$$P_{\dot{\gamma}}(\theta, \varphi) = constant \tag{4.2}$$

holds over the entire phase space of θ and φ. The viscosity is thus constant with respect to the shear rate change in this regime, *i.e.*, $\eta(\dot{\gamma}) = \eta_0$.

In contrast, the rigid rod undergoes a deterministic tumbling motion due to strong shear flow in the 2nd Newtonian regime. Here the tumbling motion is perfectly described by Jeffery's equation.[1] Therefore, the PDF approaches the high-shear limiting (non-Brownian) asymptotic form with increasing $\dot{\gamma}$,

$$P_{\dot{\gamma}}(\theta, \varphi) = P_J(\theta, \varphi), \tag{4.3}$$

where $P_J(\theta, \varphi)$ is the theoretical result of Hinch and Leal[6] derived from Jeffery's equation.[1] The viscosity, therefore, tends to be constant again in this regime, *i.e.*, $\eta = \eta_\infty$.

The viscosity exhibits strong shear-thinning behavior in the intermediate regime. The PDF is approximately given by

$$P_{\dot{\gamma}}(\theta, \varphi) \simeq P_J(\theta, \varphi) + (D_\mathrm{r}/\dot{\gamma}) P_1(\theta, \varphi), \tag{4.4}$$

where P_1 represents the leading term of the perturbation expansion of the thermal effects. It is clearly seen that the contribution from the thermal effects decreases with as the dimensionless shear rate $\dot{\gamma}/D_r$ increases in this regime, which gives rise to drastic shear-thinning behavior. The solid line that is shown in three different flow regimes in Fig. 4.1 represents a schematic illustration of the viscosity transition based on the above considerations.

Consistent with the theoretical model of Hinch and Leal,[5,6] the viscosity transition from the 1st Newtonian to shear-thinning regimes has already been successfully reproduced in various numerical

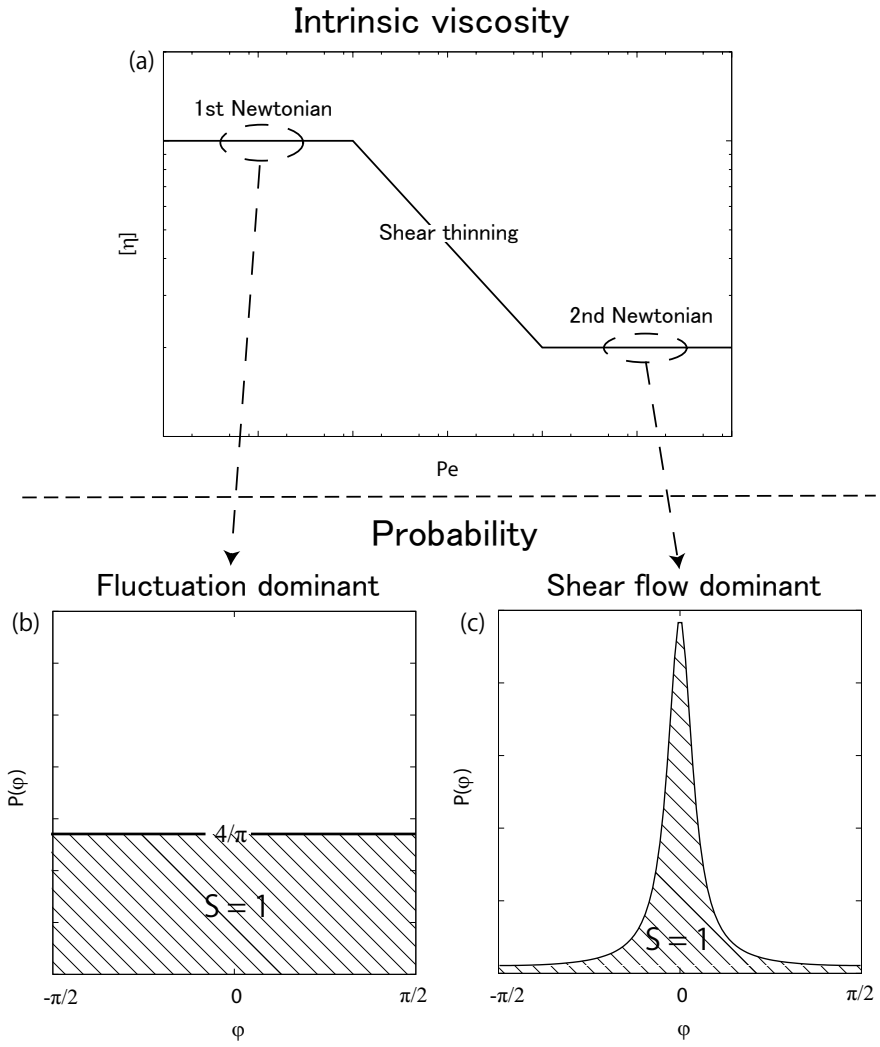

Figure 4.1: A schematic illustration of the viscosity transition. (a) A typical behavior of intrinsic viscosity $[\eta]$ as a function of Pe. Here, $P(\varphi) \equiv \int_{-\frac{\pi}{2}}^{\frac{\pi}{2}} \cos\theta P(\theta,\varphi)d\theta$ is normalized so that $S \equiv \int_{-\frac{\pi}{2}}^{\frac{\pi}{2}} P(\varphi)d\varphi = 1$. (b) $P(\varphi)$ in the weak-shear regime where the rod undergoes random tumbling. (c) $P(\varphi)$ in the strong shear regime where the rod undergoes periodic tumbling.

studies.[11,16] However, the viscosity transition from the shear-thinning to the 2nd Newtonian regime has never been successfully reproduced by numerical simulations. For rigid rod dispersions, I could not find any previous studies that have been performed at high enough shear rates to approach the 2nd Newtonian regime. Several numerical simulations have been conducted for flexible chain dispersions at high shear rates that are expected to be in the 2nd Newtonian regime. However, the viscosity transition from shear-thinning to the 2nd Newtonian behavior has never been correctly reproduced, not even when the hydrodynamic interactions are taken into account using the Rotne-Prager-Yamakawa (RPY) tensor.[16]

In the present study, I used a different class of approach, called the smoothed profile method

(SPM),[17–21] that can accurately take into account the thermal fluctuations and the hydrodynamic coupling between bead particles with a finite radius a and a Newtonian host fluid, based on direct numerical simulations (DNS) of particle dispersions. The viscosity of a rigid rod dispersion has been calculated using SPM to reproduce the viscosity transition from shear-thinning to the 2nd Newtonian regimes and to examine carefully the validity of the theoretical model proposed by Hinch and Leal.[5,6]

4.2 Methods

4.2.A Model

I solve the dynamics of a single rigid rod in a Newtonian solvent using SPM[17–20] explained in **Chapter 2**. The equation governing a solvent with density $\rho_{\rm f}$ and shear viscosity $\eta_{\rm f}$ is a modified Navier-Stokes equation:

$$\rho_{\rm f}\left[\frac{\partial \mathbf{u}}{\partial t} + (\mathbf{u}\cdot\boldsymbol{\nabla})\mathbf{u}\right] = -\boldsymbol{\nabla}p + \eta_{\rm f}\boldsymbol{\nabla}^2\mathbf{u} + \rho_{\rm f}\phi\mathbf{f}_{\rm p} + \mathbf{f}_{\rm shear} \tag{4.5}$$

with the incompressible condition $\boldsymbol{\nabla}\cdot\mathbf{u} = 0$, where $\mathbf{u}(\mathbf{r},t)$ and $p(\mathbf{r},t)$ are the velocity and pressure fields of the solvent, respectively. A smoothed profile function $0 \le \phi(\mathbf{r},t) \le 1$ distinguishes between the fluid and particle domains, yielding $\phi = 1$ in the particle domain and $\phi = 0$ in the fluid domain. These domains are separated by thin interstitial regions, the thicknesses of which are given by ξ. The body force $\phi\mathbf{f}_{\rm p}$ is introduced to ensure the rigidity of the particles and the appropriate non-slip boundary condition at the fluid/particle interface. The mathematical expressions for ϕ and $\phi\mathbf{f}_{\rm p}$ are detailed in previous papers.[17,18] The external force $\mathbf{f}_{\rm shear}$ is introduced to maintain a linear shear with a shear rate of $\dot{\gamma}$. This force is applied with the oblique coordinate transformation based on tensor analysis[21,22] in **Chapter 2**.

In this chapter, I use a bead-spring model consisting of N freely rotating beads in a single rigid rod. The bead diameter is $\sigma = 2a$. The motion of the ith bead is governed by the following Newton-Euler equations of motion with thermal fluctuations:

$$M_i\frac{d}{dt}\mathbf{V}_i = \mathbf{F}_i^{\rm H} + \mathbf{F}_i^{\rm P} + \mathbf{F}_i^{C} + \mathbf{G}_i^{V}, \quad \frac{d}{dt}\mathbf{R}_i = \mathbf{V}_i, \tag{4.6}$$

$$\mathbf{I}_i\cdot\frac{d}{dt}\boldsymbol{\Omega}_i = \mathbf{N}_i^{\rm H} + \mathbf{G}_i^{\Omega}, \tag{4.7}$$

where $\mathbf{R}_i$, $\mathbf{V}_i$, and $\boldsymbol{\Omega}_i$ are the position, translational velocity, and rotational velocity of the beads, respectively. M_i and $\mathbf{I}_i$ are the mass and moment of inertia, and $\mathbf{F}_i^{\rm H}$ and $\mathbf{N}_i^{\rm H}$ are the hydrodynamic

force and torque exerted by the solvent on the beads, respectively.[17,18] $\mathbf{G}_i^{\mathrm{V}}$ and $\mathbf{G}_i^{\Omega}$ are the random force and torque, respectively, due to thermal fluctuations.[19,20] $\mathbf{F}_i^{\mathrm{P}}$ represents the potential force due to direct inter-bead interactions.

I use a bead-spring model as a model of rod-like objects with a truncated Lennard-Jones potential and a finitely extensible nonlinear elastic (FENE) potential. The truncated Lennard-Jones interaction is expressed in terms of U_{LJ}:

$$U_{\mathrm{LJ}}(r_{ij}) = \begin{cases} 4\epsilon\left[\left(\dfrac{\sigma}{r_{ij}}\right)^{12} - \left(\dfrac{\sigma}{r_{ij}}\right)^{6}\right] + \epsilon & (r_{ij} < 2^{\frac{1}{6}}\sigma) \\ 0 & (r_{ij} > 2^{\frac{1}{6}}\sigma), \end{cases} \tag{4.8}$$

where $r_{ij} = |\mathbf{R}_i - \mathbf{R}_j|$. The parameter ϵ characterizes the strength of the interactions, and σ represents the diameter of the beads. Consecutive beads on a chain are connected by a FENE potential of the form

$$U_{\mathrm{FENE}}(r) = -\frac{1}{2}k_{\mathrm{c}}R_0^2 \ln\left[1 - \left(\frac{r}{R_0}\right)^2\right], \tag{4.9}$$

where $r = |\mathbf{R}_{i+1} - \mathbf{R}_i|$, $k_c = 30\epsilon/\sigma^2$, and $R_0 = 1.5\sigma$. $\mathbf{F}_i^{\mathrm{C}}$ is the constraint force acting on the ith bead due to the bond-angle constraints that cause the connected beads to form a straight rod.

$$\mathbf{F}_i^{\mathrm{C}} = \frac{\partial}{\partial \mathbf{R}_i}\Big(\sum_{\alpha=3}^{N} \boldsymbol{\mu}_\alpha \cdot \boldsymbol{\Psi}_\alpha\Big), \tag{4.10}$$

$$\boldsymbol{\Psi}_\alpha = (\alpha - 2)\mathbf{R}_1 - (\alpha - 1)\mathbf{R}_2 + \mathbf{R}_\alpha, \tag{4.11}$$

where $\boldsymbol{\Psi}_\alpha = 0$ is the constraint condition to be satisfied. $\boldsymbol{\mu}_\alpha$ is a Lagrange multiplier associated with the constraints that is chosen such that the condition $\boldsymbol{\Psi}_\alpha = 0$ is satisfied at a time $t + h$, where h is the time increment of a single simulation step.

The numerical simulations are performed in three dimensions with periodic boundary conditions. The lattice spacing Δ is taken to be the unit of length. The unit of time is given by $\rho_{\mathrm{f}}\Delta^2/\eta_{\mathrm{f}}$, where $\eta_{\mathrm{f}} = 1$ and $\rho_{\mathrm{f}} = 1$. The system size is $L_x \times L_y \times L_z = 32 \times 32 \times 32$. The other parameters include the following: $\sigma = 4$, $\xi = 2$, $\epsilon = 1$, $M_i = 4\pi a^3/3$, $N = 5$, and $h = 6.7 \times 10^{-2}$. In the presented simulations under shear flow, the Navier-Stokes equation is discretized with a de-aliased Fourier spectral scheme in space and with an Euler scheme in time.[21] To follow the motions of the beads, the positions, velocities and angular velocities of the beads are integrated with the Adams-Bashforth scheme. The bead particles are assumed to be neutrally buoyant, so no gravity effects are considered. At $t = 0$, the rigid rod aligns along the x-axis, which is the flow direction. The total duration τ_{t} of each simulation is set such that $\dot{\gamma}\tau_{\mathrm{t}} \simeq 3500$. The range of $k_{\mathrm{B}}T$

is $5.0 \times 10^{-4} < k_{\rm B}T/\epsilon < 32$ and that of $\dot{\gamma}$ is $5.0 \times 10^{-3} < \dot{\gamma} < 2.0 \times 10^{-2}$. From the symmetry of the system, I follow the polar angles θ and φ defined in Fig. 4.2 to consider the motion of a rigid rod. The angle defined between the rod and the x-y plane is denoted by θ, and the angle defined between the rod projected on the x-y plane and the x-axis is denoted by φ.

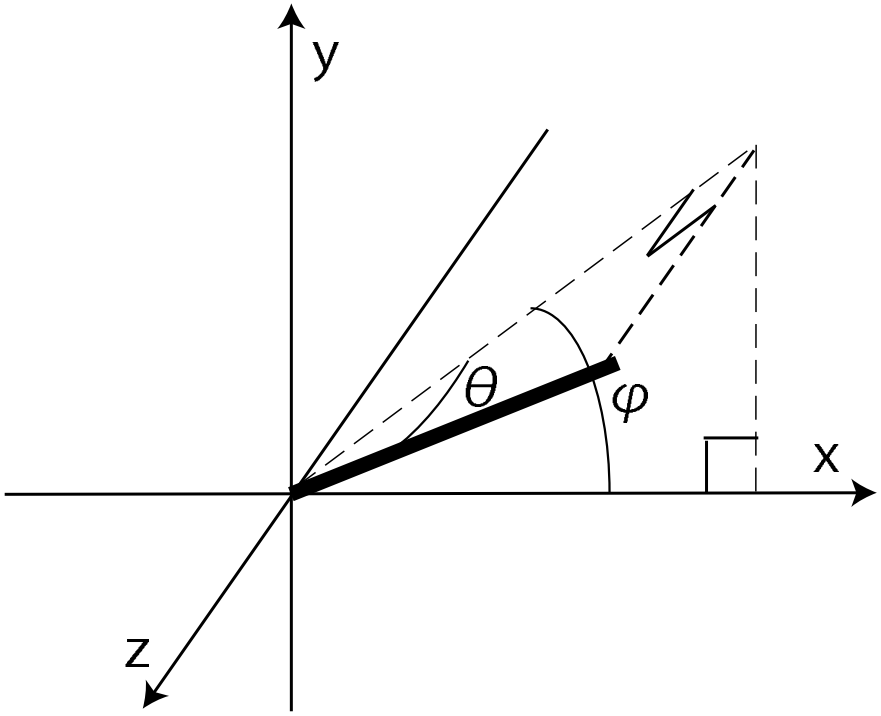

Figure 4.2: The geometry of the rod's orientation in the present simulations.

4.2.B Effective Aspect Ratio

In this chapter, the rigid rod is represented as connected beads. Because the beads composing the rod can rotate freely, the effective aspect ratio r differs from the simple geometrical aspect ratio L/σ, where $L \simeq N\sigma$ is the rod's length. Instead, I evaluate r numerically with the PDF of the rotating rigid rods without thermal fluctuations in the x-y plane, *i.e.*, $\theta = 0$, as represented by

$$P_{\rm J}(\varphi) = \frac{C_0}{\frac{r^2-1}{r^2+1}\sin^2\varphi + \frac{1}{r^2+1}}, \tag{4.12}$$

where C_0 is determined from the normalization condition $\int_{-\frac{\pi}{2}}^{\frac{\pi}{2}} P_{\rm J}(\varphi)d\varphi = 1$. One obtained Eq. (4.12) in the following manner. The projection of the PDF $P_{\rm J}(\varphi)$ of a rotating rigid rod on the x-y plane is governed by a Fokker-Planck equation of the form

$$\frac{\partial P_{\rm J}(\varphi)}{\partial t} = \frac{\partial(\omega P_{\rm J}(\varphi))}{\partial \varphi} + 2D_{\rm r}\frac{\partial P_{\rm J}(\varphi)}{\partial \varphi^2}, \tag{4.13}$$

where $\omega = \dot{\varphi}$ is the angular velocity of the tumbling rod. When the rigid rod rotates in the x-y plane without thermal fluctuations in steady states, the Fokker-Planck equation is modified to

$$\frac{\partial(\omega P_{\rm J}(\varphi))}{\partial\varphi} = 0. \tag{4.14}$$

In this case, ω is represented as

$$\omega = \dot{\gamma}\left(\frac{r^2-1}{r^2+1}\sin^2\varphi + \frac{1}{r^2+1}\right) \tag{4.15}$$

from Jeffery's equation.[1] Eq. (4.12) is obtained because $P_{\rm J}(\varphi)$ is inversely proportional to ω. Figure 4.3 shows that my numerical results of $P'(\varphi) = \int \cos\theta P_{\dot{\gamma}}(\theta,\varphi)d\theta$ of the strong shear regime agree well with $P_{\rm J}(\varphi)$ with $r = 7.1$. I thus use $r = 7.1$ for the present rigid rod, which is composed of freely rotating beads.

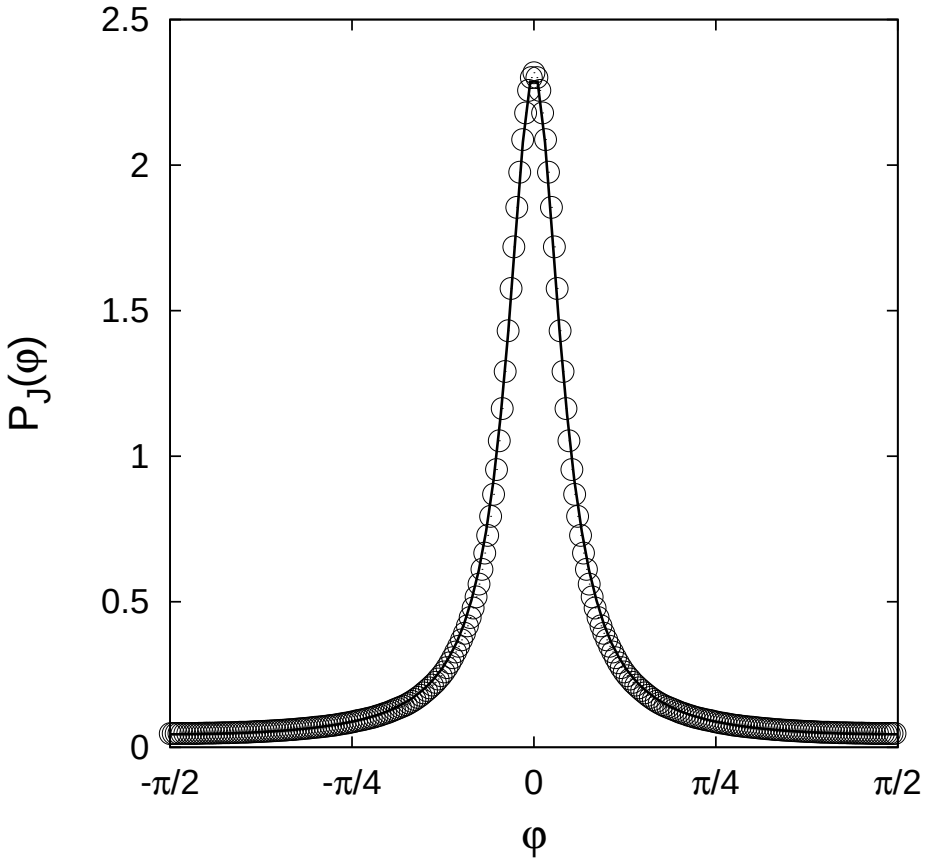

Figure 4.3: The PDF for a rotational rigid rod as a function of φ without thermal fluctuations. Numerical results (circle) and Eq. (4.12) with $r = 7.1$ (solid line).

4.2.C Analytic formula for the viscosity

Hinch and Leal[5,6] studied the rheological properties of a dilute dispersion of rigid non-spherical particles in steady shear flow. They obtained an analytical formula for the dispersion viscosity. I

analyze my numerical results with their formula. The dispersion viscosity η is given by the ensemble average of the temporal viscosity $\hat{\eta}(\theta, \varphi)$ using the PDF of the two angles for the rotating rigid rods $P_{\dot{\gamma}}(\theta, \varphi)$, which satisfies the normalization condition,

$$\int_{-\frac{\pi}{2}}^{\frac{\pi}{2}} \cos\theta d\theta \int_{-\frac{\pi}{2}}^{\frac{\pi}{2}} d\varphi P_{\dot{\gamma}}(\theta, \varphi) = 1. \tag{4.16}$$

The temporal shear viscosity is found to be

$$\begin{aligned} \hat{\eta}(\theta, \varphi) &= \eta_f \left[1 + \Phi \left(A \cos^4\theta \sin^2 2\varphi + 2B \cos^2\theta + \frac{2}{I_3} \right.\right. \\ &\qquad \left.\left. + \frac{D_{\mathrm{r}}}{\dot{\gamma}} F \frac{1}{2} \cos^2\theta \sin 2\varphi \right) \right], \end{aligned} \tag{4.17}$$

where Φ is the volume fraction of suspended particles, D_{r} is the rotational diffusion constant, and A, B, F, I_3 are the shape functions given in previous studies.[4–6] In the case of rigid rod, A, B, F, and I_3 are dependent only on the aspect ratio r. At $r = 7.1$, $A = 8.44$, $B = 0.06$, and $I_3 = 0.99$.

The shear viscosity of the dispersion is obtained by substituting Eq. (4.17) into Eq. (4.1). When we consider the strong shear case $D_{\mathrm{r}} \ll \dot{\gamma}$, we can safely neglect the last term in Eq. (4.17). The dynamics of the angle φ become decoupled from the angle θ because the angle θ is sufficiently small for a large r.[6] Thus, we obtain the following formula,

$$\eta(\dot{\gamma}) = \int \hat{\eta}(\theta, \varphi) P''(\theta) P'(\varphi) d\theta d\varphi \tag{4.18}$$

$$\begin{aligned} &= \eta_{\mathrm{f}} \left[1 + \Phi \left(A \langle \cos^4\theta \rangle_\theta \langle \sin^2 2\varphi \rangle_\varphi + 2B \langle \cos^2\theta \rangle_\theta \right.\right. \\ &\qquad \left.\left. + \frac{2}{I_3} + \Delta E \right), \right], \end{aligned} \tag{4.19}$$

where $\langle f(\theta) \rangle_\theta = \int_{-\frac{\pi}{2}}^{\frac{\pi}{2}} \cos\theta d\theta f(\theta) P''(\theta)$, $\langle g(\varphi) \rangle_\varphi = \int_{-\frac{\pi}{2}}^{\frac{\pi}{2}} d\varphi g(\varphi) P'(\varphi)$, $P''(\theta) \equiv \int_{-\frac{\pi}{2}}^{\frac{\pi}{2}} P_{\dot{\gamma}}(\theta, \varphi) d\varphi$, and ΔE is the error arising from the separation of integrals over θ and φ. We can neglect ΔE safely because ΔE is sufficiently small in comparison to the other terms.

4.3 Results

In Fig. 4.4, I plotted the intrinsic viscosity

$$[\eta] \equiv \frac{\eta - \eta_{\mathrm{f}}}{\eta_{\mathrm{f}} \Phi} \tag{4.20}$$

of the dispersion obtained from the present simulations as a function of the Peclet number Pe. Pe is the dimensionless number that represents the strength of the shear flow normalized by that due

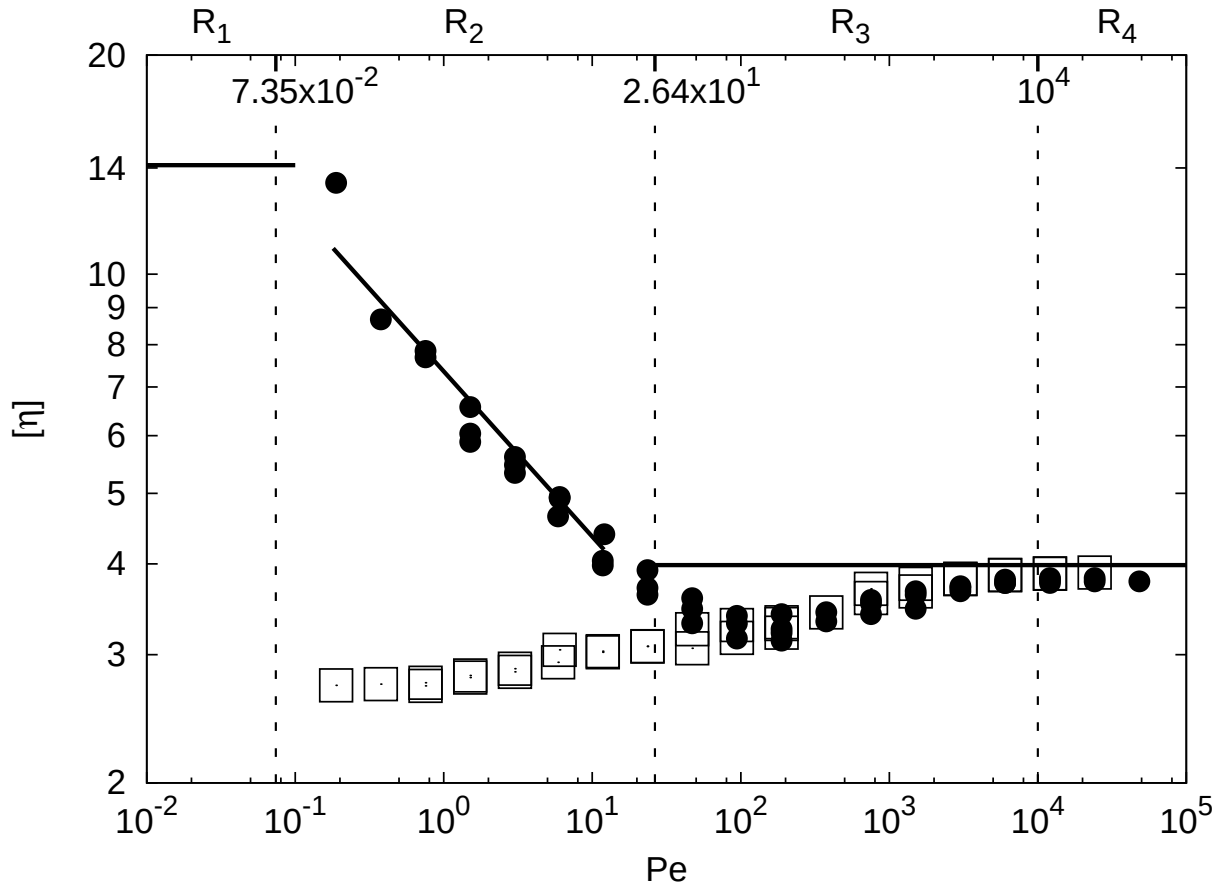

Figure 4.4: The intrinsic viscosity as a function of Pe. $[\eta]$ (circle) and $[\eta_\theta]$ (square). The three solid lines correspond to the theoretical result of Hinch and Leal:[5,6] the 1st Newtonian regime denoted by R_1, the shear-thinning regime denoted by R_2, and the 2nd Newtonian regime denoted by R_3 + R_4. In my simulation, the viscosity shows an undershoot before reaching the 2nd Newtonian regime R_3.

to thermal fluctuations. In my dissertation, Pe is defined as

$$\mathrm{Pe} = \frac{6\pi\eta_\mathrm{f}\sigma^3\dot{\gamma}}{k_\mathrm{B}T}. \tag{4.21}$$

I find that the intrinsic viscosity $[\eta]$ gradually changes from non-Newtonian (shear-thinning) to Newtonian behavior with increasing Peclet number, as shown in Fig. 4.4. The present simulation data for $[\eta]$ show shear-thinning behavior for $\mathrm{Pe} < 10^2$ and 2nd Newtonian behavior for $10^4 < \mathrm{Pe}$. Those results are in good agreement with previous theoretical studies.[5,6,9]

To quantitatively compare my results with those of Hinch and Leal,[5,6] I obtain the relation between Pe in my definition and $\dot{\gamma}/D_\mathrm{r}$, which is used in Hinch and Leal's work[5] instead of Pe. On the basis of the shell model,[23,24] the rotational diffusion constant D_r for a rigid rod is calculated as

$$D_\mathrm{r} = \frac{3(\ln r + d(r))k_\mathrm{B}T}{\pi\eta_\mathrm{f}L^3}, \tag{4.22}$$

$$d(r) = -0.662 + \frac{0.917}{r} - \frac{0.05}{r^2}. \tag{4.23}$$

In the shell model mentioned above, the contour of the macromolecules of arbitrary shape is represented by a shell composed of many identical small beads. The shell model can be adequately modeled by decreasing the size of the beads. From Eq. (4.21) and Eq. (4.22), the relation between $\dot{\gamma}/D_{\rm r}$ and Pe is expressed as

$$\frac{\dot{\gamma}}{D_{\rm r}} = \frac{r^3}{18(\ln r + d(r))}{\rm Pe}. \tag{4.24}$$

The theoretical model of Hinch and Leal is plotted also in Fig. 4.4 with the solid lines in the three different regimes, namely, the weak ($\rm R_1$), intermediate ($\rm R_2$), and strong ($\rm R_3$ + $\rm R_4$) shear regimes.

According to the work of Hinch and Leal,[5,6] for the weak shear regime $\dot{\gamma}/D_{\rm r} \ll 1$, namely, ${\rm Pe} \ll 7.35 \times 10^{-2}$, which is denoted by $\rm R_1$ in Fig. 4.4, $[\eta]$ is constant. On the basis of Ortega's work,[25] the intrinsic viscosity $[\eta]$ of the weak-shear flow regime for a rigid rod with a short aspect ratio is calculated as

$$[\eta] = \frac{4}{15}\frac{r^2}{\ln r + \Upsilon(r)}, \tag{4.25}$$

$$\Upsilon(r) = -0.90 - \frac{1.38}{r} + \frac{8.87}{r^2} - \frac{8.82}{r^3}. \tag{4.26}$$

This expression is identical to Hinch and Leal's result in the limit of $r \to \infty$. The lowest shear rate that I consider in the present simulations is still not in the weak-shear regime because of the extremely long simulation time needed to obtain reliable data.

For the intermediate shear regime $1 \ll \dot{\gamma}/D_{\rm r} \ll r^3 + r^{-3}$, namely, $7.35 \times 10^{-2} \ll {\rm Pe} \ll 26.4$, which is denoted by $\rm R_2$ in Fig. 4.4, the intrinsic viscosity $[\eta]$ shows shear-thinning as derived from Eq. (4.19),

$$[\eta] = C_1{\rm Pe}^{-1/3} + 2B + 2/I_3, \tag{4.27}$$

where C_1 is an arbitrary constant. Figure 4.4 shows good agreement between the data from the present simulation data with that of Hinch and Leal, where C_1 was determined to fit the simulation data. When r is sufficiently large, the contributions from the last two terms in Eq. (4.27) become negligible, and $[\eta] \propto {\rm Pe}^{-1/3}$.

For the strong shear regime $r^3 + r^{-3} \ll \dot{\gamma}/D_{\rm r}$, namely, $26.4 \ll {\rm Pe}$, which is denoted by $\rm R_3$ and $\rm R_4$ in Fig. 4.4, the theory predicts that the intrinsic viscosity $[\eta]$ is constant at $A\langle \sin^2 2\varphi \rangle_J + 2B + 2/I_3 = 3.99 = [\eta_\infty]$ from Eq. (4.19) with my numerical ensemble. Here $\langle \cdots \rangle_J$ denotes the ensemble average,

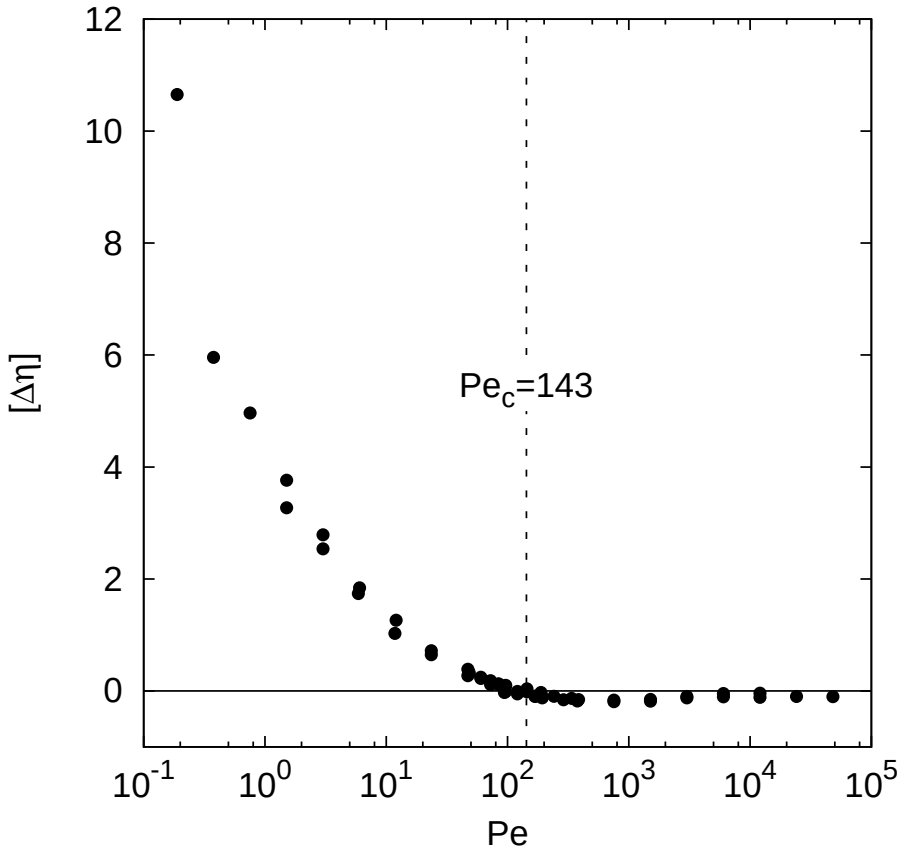

Figure 4.5: The behavior of $[\Delta\eta]$ as a function of Pe. $[\Delta\eta]$ goes to zero around Pe ≈ 150.

which is calculated as

$$\langle f(\varphi)\rangle_J = \int_{-\frac{\pi}{2}}^{\frac{\pi}{2}} d\varphi f(\varphi) P_{\rm J}(\varphi). \tag{4.28}$$

I obtained $[\eta_\infty] = 3.82$ from my numerical data in the high shear regime, which is denoted by $\rm R_4$ in Fig. 4.4. The error from the theoretical value 3.97 is within 4.26%.

For the regime $10^2 < \mathrm{Pe} < 10^3$, which is denoted by $\rm R_3$ in Fig. 4.4, the behavior of $[\eta]$ shows a notable undershoot before reaching the high-shear limiting 2nd Newtonian viscosity. This is attributable to the fluctuations in θ. It gives rise to the deviations of $P''(\theta)$ from its high-shear limiting form $P^*(\theta) \equiv \int_{-\frac{\pi}{2}}^{\frac{\pi}{2}} P_J(\theta,\varphi)d\varphi$ and increases with decreasing Pe. The rods tend to align in the flow direction with increasing Pe. Therefore, $\langle\cos^4\theta\rangle$ and $\langle\cos^2\theta\rangle$ monotonically increase up to their high-shear limiting values with increasing shear rate. This leads to an increase in $[\eta]$ up to $[\eta_\infty]$ through Eq. (4.19). To examine the role of thermal fluctuations in θ in more detail, let us

define

$$[\eta_\theta] = A\langle \sin^2\varphi\rangle_J\langle\cos^4\theta\rangle_\theta + 2B\langle\cos^2\theta\rangle_\theta + \frac{2}{I_3} \tag{4.29}$$

$$= 1.81\langle\cos^4\theta\rangle_\theta + 0.12\langle\cos^2\theta\rangle_\theta + 2.02 \tag{4.30}$$

to estimate the contribution of θ fluctuations on the total intrinsic viscosity of the dispersion. Here, $P(\varphi) = P_{\rm J}(\varphi)$ is assumed in Eq. (4.19), and $\langle\cos^4\theta\rangle_\theta$ and $\langle\cos^2\theta\rangle_\theta$ are evaluated numerically from the present simulations. The results are plotted in Fig. 4.4 with the square symbols. One can see that the data of $[\eta_\theta]$ almost perfectly collapse onto those of $[\eta]$ for $10^2 <$ Pe.

On the other hand, the shear-thinning behavior observed for $10^2 >$ Pe is attributable to the effect of the thermal fluctuations in φ. It gives rise to the deviations of $P'(\varphi)$ from its high-shear limiting form $P_J(\varphi)$ and increases with decreasing Pe. To examine this effect quantitatively, I introduce

$$[\Delta\eta] \equiv [\eta] - [\eta_\theta] \tag{4.31}$$

$$= A\langle\cos^4\theta\rangle_\theta(\langle\sin^2 2\varphi\rangle_\varphi - \langle\sin^2 2\varphi\rangle_J) \tag{4.32}$$

to eliminate the contribution of θ fluctuations from the total intrinsic viscosity of the dispersion. Figure 4.5 shows the behavior of $[\Delta\eta]$ as a function of Pe. $[\Delta\eta]$ decreases with increasing Pe, and finally $[\Delta\eta]$ goes to zero around Pe $\approx$ 150. This value is considerably different from the value Pe = 26.4 predicted by Hinch and Leal[5] for the viscosity transition from the shear-thinning to the 2nd Newtonian but agrees well with my theoretical prediction of $\mathrm{Pe_c} = 143$, at which the dynamical crossover from Brownian to non-Brownian behavior[26] explained in **Chapter 3** takes place in the rotational motion of the rotating rod at $r = 7.1$.

4.4 Discussion

Let us discuss the numerical models with which the viscosity transition to the 2nd Newtonian regime takes place based on Eq. (4.19). For the strong shear regime $1 \ll \dot\gamma/D_{\rm r}$, I can estimate $\langle\cos^2\theta\rangle_\theta \simeq 1$ and $\langle\cos^4\theta\rangle_\theta \simeq 1$ because $P_{\dot\gamma}(\theta,\varphi) \simeq P^*(\theta)P(\varphi)$. Here, $P(\varphi)$ satisfies the Fokker-Planck equation, shown as Eq. (4.13), for which the formal solution is given by

$$P(\varphi) = C_1\int_0^\pi d\psi \exp\left(-\frac{\dot\gamma}{4D_r}f(\psi,\varphi)\right), \tag{4.33}$$

$$f(\psi,\varphi) = \psi - (1 - \frac{2}{r^2+1})\sin\psi\cos(\psi - 2\varphi), \tag{4.34}$$

where C_1 is determined from the normalization condition, $\int_{-\frac{\pi}{2}}^{\frac{\pi}{2}} P(\varphi)d\varphi = 1$. When $\dot{\gamma}/D_{\rm r}$ is sufficiently large, $P(\varphi)$ converges to $P_{\rm J}(\varphi)$ represented by Eq. (4.12), and the viscosity displays 2nd Newtonian behavior.

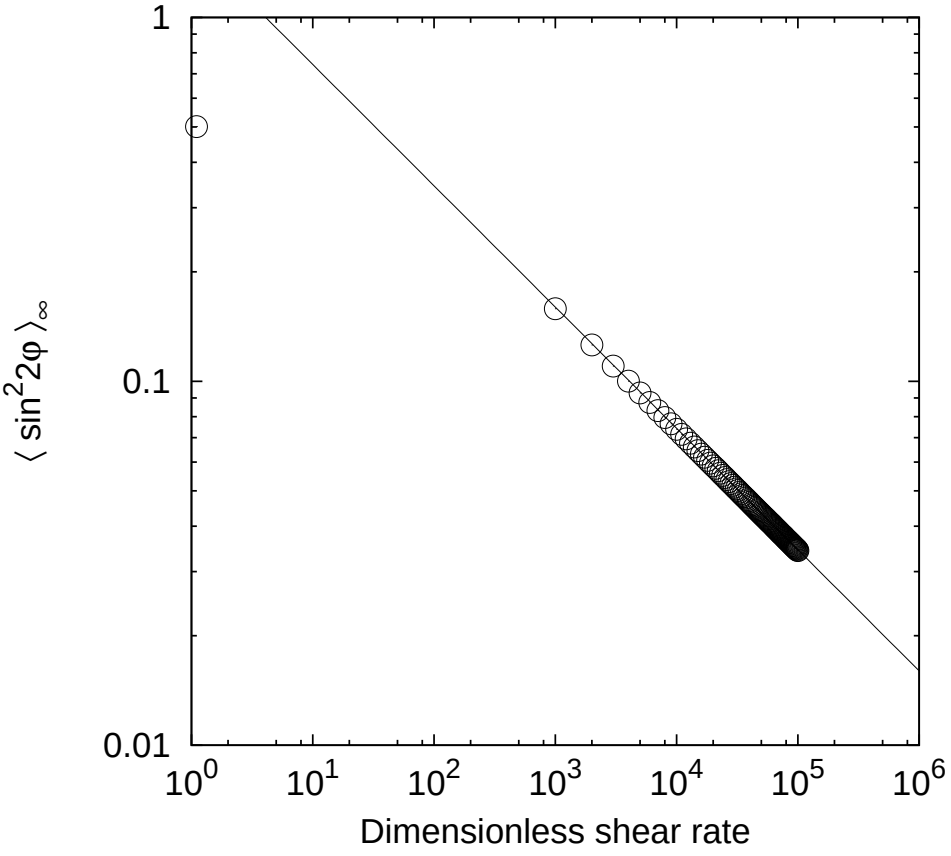

Figure 4.6: The behavior of $\langle \sin^2 2\varphi \rangle_\infty$ as a function of $\dot{\gamma}/D_r$. Numerical results (circle). The solid line corresponds to $(\dot{\gamma}/D_r)^{-1/3}$

The above discussion is not valid in the limit of $r \to \infty$, which corresponds to an infinitely-long or equivalently infinity-thin rod. In this limit, the angular velocity of the tumbling rod becomes zero at $\varphi = 0$ from Eq. (4.15). Thus, the rod cannot continue rotational motion without thermal fluctuations. This is because the hydrodynamic torque acting on the rod becomes zero at $\varphi = 0$ for $r \to \infty$. Therefore, $P(\varphi)$ in Eq. (4.33) is modified to

$$P_\infty(\varphi) = C_2 \int_0^\pi d\psi \exp\left(-\frac{\dot{\gamma}}{4D_r}\left[\psi - \sin\psi\cos(\psi - 2\varphi)\right]\right), \tag{4.35}$$

where C_2 is determined from the normalization condition, $\int_{-\frac{\pi}{2}}^{\frac{\pi}{2}} P_\infty(\varphi)d\varphi = 1$. Using Eq. (4.35), the intrinsic viscosity $[\eta]$ is rewritten as

$$[\eta] = A\langle \sin^2 2\varphi \rangle_\infty + 2B + 2/I_3, \tag{4.36}$$

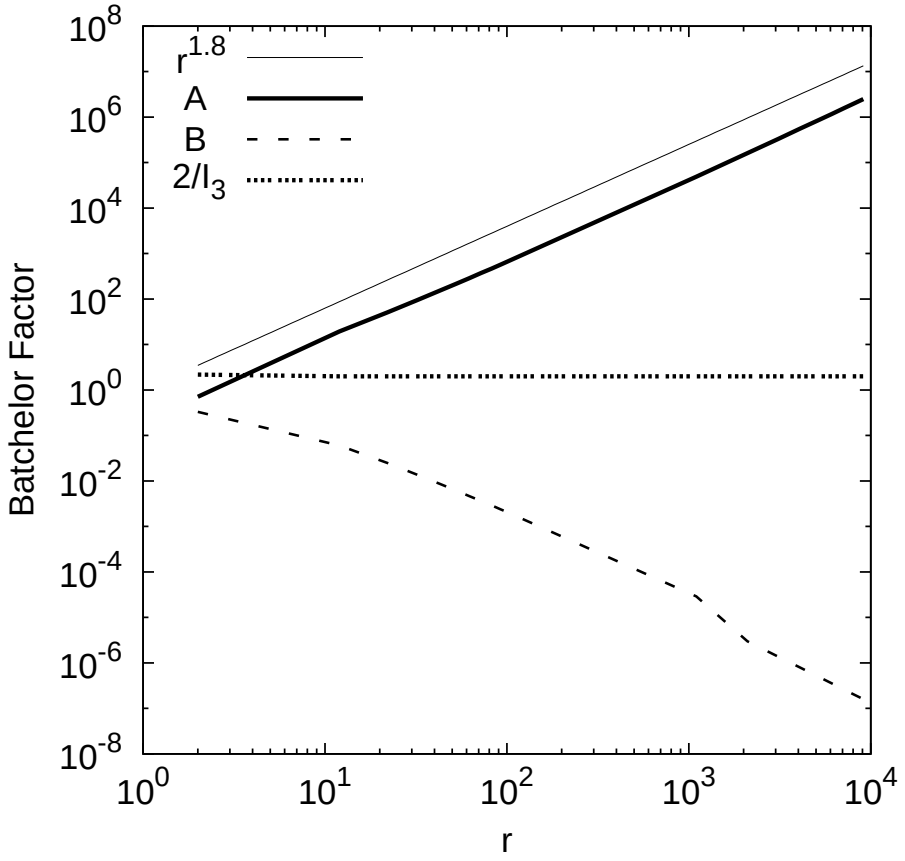

Figure 4.7: The behavior of A, B, and $2/I_3$ as a function of the aspect ratio r. A (bold solid line), B (dashed line), $2/I_3$ (dotted line). The thin solid line represents $r^{1.8}$.

$$\langle f(\varphi)\rangle_\infty = \int_{-\frac{\pi}{2}}^{\frac{\pi}{2}} d\varphi f(\varphi) P_\infty(\varphi). \tag{4.37}$$

It is demonstrated in Fig. 4.6 that the first term in Eq. (4.36) shows $\langle \sin^2 2\varphi\rangle_\infty \propto (\dot{\gamma}/D_\mathrm{r})^{-1/3}$ for the entire range of Pe. Figure 4.7 shows that only A is increasing with increasing r, while B and $2/I_3$ tend to be decreasing or constant upon increasing r. I estimate $A/(2B + 2/I_3) \sim r^{1.8}$ for $r \to \infty$. This indicates that

$$[\eta] \propto \langle \sin^2 2\varphi\rangle_\infty \propto (\dot{\gamma}/D_\mathrm{r})^{-1/3} \tag{4.38}$$

holds for the entire range of Pe without indicating the occurrence of 2nd Newtonian behavior. The same conclusion can be derived by considering a characteristic shear rate $\dot{\gamma}^*$ at which the first term in Eq. (4.36) becomes comparable to the remaining terms. The condition is satisfied at

$$\frac{\dot{\gamma}^*}{D_\mathrm{r}} \sim l^{5.4}. \tag{4.39}$$

This indicates $\dot{\gamma}^* \to \infty$ for $r \to \infty$.

In the case of a previous numerical study,[16] the hydrodynamic force acting on each bead particle was considered via the RPY tensor. Although the translational hydrodynamic force was properly considered, the rotational hydrodynamic torque acting on each bead particle was completely ignored in that study. Therefore, it is suspected that the hydrodynamic torque acting on the rod becomes zero at $\varphi = 0$. Therefore, the rod cannot continue rotational motion at a high shear rate, where the effect of thermal fluctuations disappears. This situation is exactly the same as the case of $r \to \infty$. I expect that the 2nd Newtonian regime could be correctly reproduced with the RPY tensor approach if the hydrodynamic torque is taken into account properly.

4.5 Conclusion

In the present study, I numerically calculated the intrinsic viscosity $[\eta]$ of a dilute dispersion of rigid rods using a DNS method known as SPM. Simulations were conducted under the influence of thermal fluctuations and shear flow in the ranges of $5.0 \times 10^{-4} < k_{\mathrm{B}}T/\epsilon < 32$ and $5.0 \times 10^{-3} < \dot{\gamma} < 2.0 \times 10^{-2}$, respectively. I have successfully reproduced the viscosity transition from the shear-thinning to the 2nd Newtonian regimes, as was correctly predicted by the theoretical model of Hinch and Leal.[5,6]

There are, however, some discrepancies between the theoretical predictions and the results of the present simulations. By defining $[\Delta\eta]$ to eliminate the effects of fluctuations in θ, which is not considered in the theoretical model, I confirmed that the viscosity transition from the shear-thinning to the 2nd Newtonian takes place around $\mathrm{Pe} = 150$. This value is considerably larger than the value of 26.4 predicted by Hinch and Leal[5] but agrees well with my theoretical prediction of $\mathrm{Pe_c} = 143$, at which the dynamical crossover from Brownian to non-Brownian behavior takes place in the rotational motion of the rotating rod.[26]

I have analyzed the mechanism of the viscosity undershoot observed in my simulation before reaching the 2nd Newtonian regime. Shear flow suppresses fluctuations in φ and θ as its rate is increased. The former contributes to decrease $[\eta]$, but the later contributes to increase $[\eta]$. The undershoot takes place because of the two competing effects.

I also conclude that the viscosity transition to the 2nd Newtonian regime can be reproduced correctly only if the hydrodynamic torque is properly taken into account in numerical models of the dispersions.

References

1 G. B. Jeffery, Proc. R. Soc. A **102**, 161 (1922).

2 A. Peterlin and H. A. Stuart, Z. Phys. **112**, 1 (1938).

3 V. H. Giesekus, Rheol. Acta. **2**, 50 (1962).

4 G. K. Batchelor, J. Fluid Mech. **41**, 545 (1970).

5 E. J. Hinch and L. G. Leal, J. Fluid Mech. **52**, 683 (1972).

6 L. G. Leal and E. J. Hinch, J. Fluid Mech. **46**, 685 (1971).

7 E. J. Hinch and L. G. Leal, J. Fluid Mech. **71**, 481 (1975).

8 E. J. Hinch and L. G. Leal, J. Fluid Mech. **76**, 187 (1976).

9 L. G. Leal and E. J. Hinch, Rheol. Acta **12**, 127 (1973).

10 H. A. Scheraga, Z. Phys. **23**, 1526 (1955).

11 J. F. Ryder and J. M. Yeomans, J. Chem. Phys. **125**, 194906 (2006).

12 H. Chen, Y. Ding, and A. Lapkin, Powder Tech. **194**, 132 (2009).

13 G. Chauveteau, J. Rheol. **26**, 111 (1982).

14 I. Noda, Y. Yamada, and M. Nagasawa, J. Phys. Chem. **72**, 2890 (1968).

15 R. L. CHRISTIANSEN and R. B. BIRD, Journal of Non-Newtonian Fluid Mechanics **3**, 161 (1977).

16 D. Petera and M. Muthukumar, J. Chem. Phys. **111**, 7614 (1999).

17 Y. Nakayama and R. Yamamoto, Phys. Rev. E **71**, 036707 (2005).

18 Y. Nakayama, K. Kim, and R. Yamamoto, Eur. Phys. J. E **26**, 361 (2008).

19 T. Iwashita, Y. Nakayama, and R. Yamamoto, J. Phys. Soc. Jpn. **77**, 074007 (2008).

20 T. Iwashita and R. Yamamoto, Phys. Rev. E **79**, 031401 (2009).

21 H. Kobayashi and R. Yamamoto, J. Chem. Phys. **134**, 064110 (2011a).

22 A. Onuki, J. Phys. Soc. Jpn. **66**, 1836 (1997).

23 M. M. Tirado and J. G. de la Torre, J. Chem. Phys. **73**, 1986 (1980).

24 M. M. Tirado, J. Chem. Phys. **81**, 2047 (1984).

25 A. Ortega and J. G. de la Torre, J. Chem. Phys. **119**, 9914 (2003).

26 H. Kobayashi and R. Yamamoto, Phys. Rev. E **81**, 041807 (2010b).

Chapter 5

General conclusion

In order to investigate the dynamical behavior of dilute dispersions of chains in shear flow, several numerical studies are proposed.

In **Chapter 2**, I presented a generic methodology for performing DNS of particle dispersions in a shear flow using oblique coordinates and periodic boundary conditions. The validity of the method was confirmed by comparing the present numerical results with experimental viscosity data for particle dispersions over a wide range of the parameters Φ and $\dot{\gamma}$ that include nonlinear shear-thinning regimes. An important advantage of the DNS approach over other approaches such as Stokesian dynamics is its applicability to particle dispersions in complex fluids. In fact, electrophoresis of charged colloids and particle dispersions in nematic liquid crystals have already been calculated using SPM. My methodology can also be applied to simulate particle dispersions in viscoelastic fluids simply by replacing the Newtonian constitutive equation to more complex ones such as Maxwell model.

In **Chapter 3** , I calculated the tumbling motion of a single chain using an SPM that takes into account thermal fluctuations and hydrodynamic interactions for $0.0005 < k_{\mathrm{B}}T/\epsilon < 1.00$ and $0.001 < \dot{\gamma} < 0.02$. I conclude that the dimensionless frequency, F, depends only on Pe. The dependence of F can be described by a power law $F \propto Pe^{\alpha}$. The exponent α sharply changes from 2/3 to 1 on Pe_{c}. In the case of a rigid rod with $N = 5$, $Pe_{\mathrm{c}} \approx 106$, and in the case of a flexible chain with $N = 5$, $Pe_{\mathrm{c}} \approx 156$. The behavior of F for both cases is similar, while only the values of Pe_{c} are different from each other. I presented F to be proportional to $Pe^{2/3}$ when the third term on the right-hand side of Eq. (3.17) dominates in the region $0 < \varphi < \varphi_t$, and F is proportional to Pe when the second term of Eq. (3.17) dominates in the region $0 < \varphi < \varphi_t$. I estimated the angle φ_t at which the fist term of J_φ, expressed as Eq. (3.20), is comparable to the sum of the second and third terms of J_φ, expressed as Eq. (3.20). A proposed mechanism for this exponent change is that the effect of thermal fluctuation is more significant than the effect of shear flow only for $0 < \varphi < \varphi_t$, whereas in the other case, the effect of thermal fluctuation is negligible. The former contribution leads to $F \propto Pe^{2/3}$, and the latter contribution leads to $F \propto Pe$.

In **Chapter 4**, In the present study, I numerically calculated the intrinsic viscosity $[\eta]$ of a dilute dispersion of rigid rods using a DNS method known as SPM. Simulations were conducted under the influence of thermal fluctuations and shear flow in the ranges of $5.0 \times 10^{-4} < k_{\mathrm{B}}T < 32$ and $5.0 \times 10^{-3} < \dot{\gamma} < 2.0 \times 10^{-2}$, respectively. I have successfully reproduced the viscosity transition from the shear-thinning to the 2nd Newtonian regimes, as was correctly predicted by the theoretical model of Hinch and Leal. There are, however, some discrepancies between the theoretical predictions and the results of the present simulations. By defining $[\Delta\eta]$ to eliminate the effects of fluctuations in θ, which is not considered in the theoretical model, I confirmed that the viscosity transition from the shear-thinning to the 2nd Newtonian takes place around Pe = 150. This value is considerably larger than the value of 26.4 predicted by Hinch and Leal but agrees well with my theoretical prediction of $\mathrm{Pe_c} = 143$, at which the dynamical crossover from Brownian to non-Brownian behavior explained in **Chapter 3** takes place in the rotational motion of the rotating rod. I have analyzed the mechanism of the viscosity undershoot observed in my simulation before reaching the 2nd Newtonian regime. Shear flow suppresses fluctuations in φ and θ as its rate is increased. The former contributes to decrease $[\eta]$, but the later contributes to increase $[\eta]$. The undershoot takes place because of the two competing effects. I also conclude that the viscosity transition to the 2nd Newtonian regime can be reproduced correctly only if the hydrodynamic torque is properly taken into account in numerical models of the dispersions.

Although the viscosity and the dynamics of dilute dispersions of chains in shear flow were clear for these results, many problems remain to be solved for dispersions of chains in shear flow. One of the problems is the contradiction between theoretical and experimental work on condensed dispersions of chains. Theoretical works[1–3] reported that the dynamics of rigid rods in condensed dispersions exhibits chaotic behavior at very high shear rates; namely, the Peclet number is very large. On the other hand, many experiments on macroscopic fibers[4] have reported that the rheological responses are stationary. This contradiction and many other problems with condensed dispersions of chains will be solved in future work.

References

1 G. Marrucci and P. L. Maffetone, J. Rheol. **34**, 1217 (1990).

2 G. Rienäcker and S. Hess, Physica A **267**, 294 (1999).

3 G. Rienäcker, M. Kröger and S. Hess, Phys. Rev. E **66**, 040702(R) (2002).

4 M. A. Zirnsak, D. U. Hur and D. V. Boger, J. Non-Newtonian. Fluid. Mech. **54**, 153 (1994).

Acknowledgements

I am grateful to Professor Ryoichi Yamamoto for his encouragement, support and guidance throughout my PhD course. The authors would like to express their gratitude to Dr. T. Murashima, Dr. Y. Nakayama, Dr. K. Kim, Dr. T. Iwashita and Mr. Tatsumi for useful comments and discussions.

List of Publications

Chapter 2

H. Kobayashi, and R. Yamamoto, " Implementation of Lees-Edwards periodic boundary conditions for direct numerical simulations of particle dispersions under shear flow ", J. Chem. Phys. **134** 064110 1-7, (2011).

Chapter 3

H. Kobayashi, and R. Yamamoto, " Tumbling motion of a single chain in shear flow: a crossover from Brownian to non-Brownian behavior ", Phy. Rev. E **81**, 041807 1-8, (2010).

Chapter 4

H. Kobayashi, and R. Yamamoto, " Reentrant transition in the shear viscosity of dilute rigid rod dispersions ", **submitted**.